ONE–DIMENSIONAL NANOSTRUCTURES AND MICROSTRUCTURES

BY

TEMPLATED HIGH–TEMPERATURE CONVERSIONS

Dissertation

zur Erlangung des akademischen Grades

Doktoringenieur (Dr.-Ing.)

genehmigt durch die

Mathematisch-Naturwissenschaftlich-Technische Fakultät

(Mathematisch-naturwissenschaftlicher Bereich)

der Martin-Luther-University Halle-Wittenberg

von Frau Dipl.-Ing. Lili Zhao

geboren am 14.06.1978 in Harbin, China

Gutachter:

1. Prof. Dr. U. Gösele

2. Prof. Dr. H. Hahn

Halle (Saale), den 9 October 2006

verteidigt am 02.07.2007

TABLE OF CONTENTS

CHAPTER I

Introduction

1.1 *Scope of the thesis*

The goal of this thesis is to develop a generic procedure for the production of high quality functional 1D nanostructures and microstructures by templated high-temperature conversion using ordered porous materials as templates and reactants as well as characterization in forms of structure and their relevant properties. The thesis mainly includes two parts, as discussed in the following:

- Templated high-temperature thermolysis of arylchalcogenolates as single source precursors. As a set of single source precursors, with similar wetting and decomposition behavior, can be used for fabrication of 1D nanostructures and microstructures consisting of a variety of target materials by templated thermolysis. Thus a series of single-source precursors, arylchalcogenolates, was selected for the fabrication of 1D nano-objects using a templated high-temperature conversion method. (a) Thermolysis of arylchalcogenolates inside the pores of porous templates, under conditions where the templates are inert, was explored. In these cases the porous materials only served as "molds" and modified the morphology of the nano- and microstructures. A series of II/VI and IV/VI semiconductor nano- and microstructures were obtained. As a selected example, the preparation of CdSe single-crystalline nanowires and polycrystalline microtubes will be described. (b) High temperature chemical transformations exploiting the oxidizing and reducing properties of the ordered porous templates further extend the range of accessible target materials that the 1D nanostructures and microstructures may consist of. Thermolysis of arylchalcogenolates wetted templates under conditions where the templates act as reactants in a controlled manner were studied. The use of template as a reactant again includes two parts. (i) Redox reaction with the template pore walls. Example is Sn, SnSe and SnO_2 microtubes, nanotubes and nanowires by conversion of $Sn(SePh)_4$. (ii) A direct chemical reaction with the template pore walls. Examples is ZnTe, Te, $ZnAl_2O_4$-Te nanowires and $ZnAl_2O_4$ nanotubes by conversion of $Zn(TePh)_2 \cdot$TMEDA.

- Modification of macroporous silicon by functional inorganic oxide microtubes. In order to exploit the versatility of the templated high-temperature conversion approach, we extended the range of template from wetting of ordered porous alumina to macroporous silicon. Two different were investigated (a) Modification of macroporous silicon with $LiNbO_3$ and $Er:LiNbO_3$ microtubes. These microtubes were prepared by an approach of modified templated conversion, high-temperature melt wetting, which involved a direct melt infiltration of inorganic target materials into templates. This method enabled a controlled doping level of the tube walls inside the pores. The tubes within the templates in turn modify the properties of the porous host. (b) Modification of macroporous silicon by crystalline SiO_2 microtubes. Crystalline SiO_2 microtubes were obtained by lithium-induced crystallization of amorphous silica microtubes. Lithium served as catalyst during the crystallization process. Thus we prepared crystalline SiO_2 microtubes using macroporous silicon templates even without any infiltration step.

1.2   1D nanostructures and microstructures

On the nanoscale, not only the physical properties, the chemical properties of materials are different from their bulk conterparts. In the past decades, nanostructured materials, especially 1D nanostructures and microstructures, in particular nanoscale wires and tubes, have received a great deal of attention from the scientific and industrial communities due to their unique properties and potential applications.

1D nanostructures represent structure with the lowest dimension that can efficiently transport electrical carriers, and are thus ideally suited to the critical and ubiquitous task of moving charges in integrated nanoscale systems. Moreover, 1D nanostructures can also exhibit device functions, and thus be exploited as both writing and device elements in architectures for functional nanosystems. In the regard, inorganic nanowires, especially semiconductor nanowires, have shown particular promise. Semiconductor nanowires represent one of the best-defined and controlled classes of nanoscale building blocks, which correspondingly have enabled a wide-range of devices and integration strategies to be pursued in a rational manner. For instance, semiconductor nanowires were assembled into nanometer scale field-effect transistors (FETs) [1], p-n diodes [2] [3], light emitting diodes (LEDs) [2], bipolar junction transistors [3], complementary inverters [3], complex logic gates and even computational circuits that have been used to carry out basic digital calculations [4]. In addition

to nanowires, nanotubes represent another class of interesting and important one-dimensional nanostructures. Due to their geometry, tubular nanomaterials can have a low mass density, a high porosity, and an extremely large surface to weight ratio. Thus, tubular structures were received wide attention because of their great potentials in addressing some basic issues about dimensionally and space-confined transport phenomena as well as their superior performance in application areas such as catalysis, fuel cells, chemical sensors, nano-electronic devices, electronics, optoelectronics, drug release, and biochemical functionalized membranes.

1D microstructures, especially microtubes, provide with unique tubular features on the micrometer scale, might probably be even more relevant to real applications than nanostructures. For practical applications, complex multilayered hybrid structures composed of metal, dielectric, and/or magnetic-material layers were prepared. This could substantially widen the possible applications of such tubes and related objects in micromechanics and in micro- and nanoelectronics. For example, two-dimensional electron systems (2-DES) in InGaAs microtubes were realized [5]. Moreover, in piezoelectric microtubes fabricated by the template-assisted method macroporous silicon was used as a template. The tubes with diameters in the micron range and a high aspect ratios will enable extreme miniaturization of scanners. As the fabrication methods are similar as in thin-film technology, wafer-scale integration of the piezoelectric scanner arrays with silicon microelectronics should be possible [6].

In the last decades, numerous methods for preparing 1D nano- and micro-scale materials have been developed. The most successful approaches to the preparation of nanowires include: Vapor-liquid-solid growth [7] [8], template-assisted preparation [9], solution-liquid-solid growth [10], and laser ablation [7]. The most important methods for the growing of inorganic nanotubes and microtubes can be divided broadly into sulfurization [11], decomposition of a precursors [12], template-assisted growth [13], rolling-up because of misfit-induced stress [14], and direct synthesis from the vapor phase [15]. Their main weakness is, however, the poor control of final morphology and arrangement of the produced nanostructures and microstructures although some specific properties (for example, the enhanced electronic conductivities) are exhibited only with enhanced ordered.

1.3 Highly ordered arrays of 1D nanostructures and microstructures

Assembling 1D structures on a large scale into highly ordered arrays, especially keeping them in good orientation and arrangement as well as building them onto various substrates will probably lead to practical uses in many fields. The aligning of 1D structures will gives an opportunity to discover a series of new properties arosing from such superstructures [16] [17]. For instance, Willner et al. [17] investigated the generation of photocurrents in structurally controlled DNA-cross-linked CdS nanoparticle arrays. Yang et al. [18] demonstrated room temperature lasers based on ZnO nanowire arrays, which could have applications in optical computing, information storage, and microanalysis. Health et al. [19] produced ultrahigh-density arrays of aligned metal and semiconductor nanowires and circuits. Whitney et al. [9] reported that arrays of template synthesized ferromagnetic Ni and Co nanowires that display a preferred magnetization direction perpendicular to the film plane with enhanced coercivities as high as 680 oersteds and remnant magnetization up to 90%.

There are mainly three approaches to fabricate ordered arrays of 1D nano- and microstructures. One method is the so-called vapor-liquid-solid (VLS) growth [7] [8]. A critical feature of this method is that catalyst is used to define one-dimensional growth and frequently the catalyst is observed at the nanowire tip. The second method is oxide-assisted semiconductor nanowire growth [20], thermal evaporation, or chemical vapor deposition [21] [22]. In this approach, each nanowire consists of an amorphous oxide shell, and a high density of defects has been observed in the crystalline core. The third is a template-assisted synthesis, which was pioneered by Martin [23] and extended by several others [24] [25]. In this method, the porous materials serve as "molds" to guide the growth of wires and tubes that are synthesized in the pores. Due to the cylindrical pore geometry and monodisperse diameters, corresponding cylindrical and oriented nano- and microstructural materials with a narrow diameter distribution can be obtained. One the other hand, the growth is controllable almost exclusively in the direction parallel to the the pore axis. Based on this approach, arrays of metallic [26], oxidic [27], and semiconductor compounds 1D nanostructures [28] [29] were successfully prepared. Synthesis in a template is taken as one of the most universal and efficient methods for the fabrication of highly ordered arrays of nano- and microstructures.

The method based on using porous materials as templates has been quite successful in terms of controlling the material morphology and arrangement. However, it is

difficult to obtain single-crystalline materials. Wires or tubes obtained by template wetting are usually composed of nano-scale grains, and they are polycrystalline in structure. Polycrystalline materials show relatively poor mechanical properties. The grain boundary scattering of carries could also greatly affect their electrical transport properties. Thus could limit their potential use in studies or applications related to electronic transport.

The template pore walls of porous alumina consist of an amorphous gel containing water and electrolyte ions. These represent basically active groups having oxidizing or reducing properties at elevated temperatures, and may oxidate or reduce the materials within the pores. Moreover, at certain suitable conditions, the pore walls are not only limited to redox reactions, they may directly react with the nanomaterial in the pores. All these unexplored issues should be investigated in order to well control the structure and property of the obtained functional nano- and micromaterials.

1.4   Potential applications

As mentioned above, one-dimensional nano- and microstructures are very promising materials for future electronics, they are structures with the lowest dimensional that can be used for efficient transport of electrons. They are thus expected to be critical to the function and integration in today's nano-scale electronic [3] and opto-electronic devices [30]. Especially highly ordered arrays of 1D nano microstructures and microstructures fabricated by template-assisted approach (introduced in section 1.3) have some specific properties which may lead practical applications in many fields. The ordered arrays have applications in chemical and biosensors, photocatalysis and solar energy conversion devices as well as optoelectronic applications. Examples of nanowire arrays are as following:

- Aligned semiconductor nanowire arrays by template-assisted growth, such as II-VI compound semiconductors (ZnO, CdS, CdSe, CdTe, etc.) and III-V semiconductors (GaN and InP), due to their highly crystallinine and well-oriented properties, are good candidates for excitonic laser action and thus could be used for the nanowire lasers [28].

- These nanowire arrays could also be used as luminescent emitters for planar displays [31]. Due to the high density and highly regular arrangement of the nanowires arrays, the size of the emitter could be greatly decreased and the number of emitters area could be increased. This would increase the resolution and improve the stability of the display.

- The nanowire arrays could be used as a new class of semiconductor electrodes for photovoltaics [29]. CdSe nanorods have been used to fabricate efficient hybrid solar cells together with polymers [32].

- The nanowire arrays could be used as a photocatalyst for the light-induced redox processes. Lakshmi et al. [27] investigated the decomposition of salicylic acid over time on an array of immobilized TiO_2 fibers with exposure to sunlight. They observed a marked increase in decomposition rate of salicylic acid for the template-synthesized TiO_2 fibres.

In addition to nanowires, high quality functional 1D nano- and microtubes in porous membranes, represent another class of interesting and important nanostructures to study because of their potentially superior performance in applications such as gas storage, energy conversion, fluid transportation, catalysis, electronics, optoelectronics, drug release, and sensing. Outstanding examples of arrays generated by the template-assisted route are nanotubes of TiO_2 [33] which can be used as photocatalysts due to their high photoefficiency, semiconductor nanotubes of In_2O_3 and Ga_2O_3 [34] for the applications of gas sensors and optoelectronic nanodevices, and $BaTiO_3$ and $PbTiO_3$ [35] nanotubes for their piezoelectric or ferroelectric behavior. Besides nanotubes, ordered arrays of microtubes prepared in macroporous silicon templates also attracted much attention. For instance, piezoelectric microtubes are ideal candidates for electromechanical system such as mesoscopic actuators similar to current piezoelectric scanners, mass storage devices as well as tunable photonic crystals [6] [36].

In addition to the specific properties of highly ordered arrays, aligned of 1D nanostructured objects in porous membranes gives an opportunity to investigate properties that can not easy be measured by using other methods. For instance, Au nanodisk electrodes prepared by using the template method offer the opportunity to study the kinetics of charge-transfer processes that are too fast to measure with conventional macroscopic electrodes [37]. The ultratrace levels of electroactive species can be detected with ensembles of nanoscopic electrodes [38] and electrochemistry can be performed in highly resistive media [39]. Membranes filled with Co, Ni, or Fe are magnetic nanocomposites that have a strong perpendicular magnetic anisotropy suitable for perpendicular recording [40].

12

1.5 Organization of the thesis

This dissertation is organized in the following manner. The introduction is followed by an overview on the synthesis of 1D nanostructures and microstructures (chapter 2). Chapter 3 is a detailed description of the fabrication of porous templates, including porous alumina and macroporous silicon. Chapter 4 is an experimental chapter, describes all the methods used for measuring properties and for structural characterization of 1D nanosystems. In chapter 5, the concept of templated high-temperature thermolysis of single-source precursors using ordered porous alumina as a template and reactant is introduced. It will be explained that porous templates can either serve only as a inert "mold" to direct the dimension of the nano-objects and micro-objects or besides defining the morphology, can also induce a conversion of the materials in the pores. This allows the preparation of different target materials from one and the same precursor by changing the reaction conditions in the nanopores.

In order to further exploit the versatility of the templated high-temperature conversion approach, in the following part of the thesis (chapter 6) the investigation on the modification of macroporous silicon was extended to functional inorganic oxide microtubes base on this method. The modification began with $LiNbO_3$ and $Er:LiNbO_3$ microtubes fabricated by high-temperature melt wetting and finished in crystalline SiO_2 microtubes, the crystallization of which is induced by lithium ions. Finally, chapter 7 gives a summary based on the results obtained.

CHAPTER II

1D Nanostructures and Microstructures: State of the Art Preparation Methods

This chapter will give an overview of existing approaches and previous work on the synthesis of 1D nanostructures and microstructures. Based on the difference of reaction media, the synthesis methods can be divided into two categories: solution-based and template-assisted (template-directed) approaches.

2.1 Solution-based approaches

Solution-based synthesis methods in principal contain four major methods: concentration depletion method, solution-liquid-solid method, solvothermal chemical synthesis and self-assembly.

- Concentration depletion: This nucleation induced concentration depletion was first observed in various colloidal systems by Matijevicin 1994 [41]. A zone of concentration depletion is formed in the center of the growing surface because these sites usually have higher free energies than other regions on the surface in the solution[42]. By forming a concentration depletion zone at the surface of a growing seed, many materials have inherently anisotropic feature in their crystal lattices, can be directed to grow into nano- and microtubes. Trigonal-phase selenium (t-Se) and tellurium (t-Te) are two such examples [43].

- Solution-liquid-solid (SLS): The use of SLS method for the growth of InP, InAs, and GaAs nanowhiskers was introduced by Buhro's group at Washington University [10]. This mechanism shows processes analogous to that of vapor-liquid-solid (VLS) growth but can operate at low temperatures and using solution-phase-reactions. The materials obtained are either fibers or near-single-crystal whiskers having diameters of 10 to 50 nm and lengths of up to several micrometers. For instance, methanolysis of t-Bu$_2$In[-P(SiMe$_3$)$_2$]$_2$ in aromatic solvents gives highly crystalline InP fibers at temperature as low as 111-203°C [44]. Silicon nanowires were obtained by a supercritical fluid solution-phase approach.

In addition to elemental semiconductors (Si and Ge) and III-V semiconductor (GaAs, GaP, InP, InAs), it was reported that well-established II-VI (ZnS, ZnSe, CdS, CdSe) semiconductor nanocrystal method can be modified for the synthesis of semiconductor nanorods [45].

- Solvothermal chemical synthesis: In solvothermal chemical synthesis processes, a solvent is mixed with certain metal precursors and possibly a crystal growth regulating or templating agent such as amines. This solution mixture is then placed in an autoclave kept at relatively high temperature and pressure to carry out the crystal growth and assembly process. This methodology seems to be quite versatile and has been demonstrated to be able to produce many different crystalline semiconductor nanorods and nanowires as exemplified by extensive work performed by Qian's group [46] [47].

- Self-assembly: Self-assembly is a method that organizes materials (molecules, nanocrystals, etc.) through noncovalent interactions such as hydrogen bonding, Van der Waals forces, electrostatic forces, etc. That is, this structure can form by itself without external intervention. By choosing suitable chemical conditions, various nanostructured materials can be obtained by a simple self-assembling process. CdSe nanocrystals were fabricated in large quantities with variable aspect ratios and excellent monodispersity by Alivisatos et al. [48]. El-Sayed induced self-assembly of these particles into one-, two- and three-dimensional arrays [49].

Solution-based processes have been extensively examined as one possible route for the preparation of 1D nanostructured materials. Solution-based methods commonly yield single-crystalline nanoobjects with uniform length and diameter strictly controlled processing conditions. However, self-assembly occurring at a specific area or position are very critical problems during applications. Self-assembly of silver nanocrystals forming a ring shape with micron scale diameter shows the possibility of controlling self-assembly [50].

2.2   Porous materials as templates

As discussed in chapter 1, section 1.3, an important issue in the synthesis and application of 1D nano- and microstructures is how to assemble them into an effective and controllable way. One of the easiest ways to control the shape and size of a target material is to synthesize it inside a mold or template. The size and shape

of the resulting object is determined by that of the template. This is the so-called template-assisted or template-directed approach.

There are a variety of interesting and useful characteristics associated with using porous materials as templates for the fabrication of nanostructured materials. Probably the most useful feature of this method is the extremely general aspect with regard to the type of materials that can be prepared. Nearly any chemical used to prepare bulk materials can be adapted to generate 1D nanomaterials within the cavities of the template. Secondly, both tubular and fibrillar nanosystems with very small diameters can be prepared. In the case of using mesoporous silica materials (SBA-15 or MCM), the nanowires obtained have diameter as small as 3 nm. These tubular or fibrillar nano- and microstructures can be assembled into a variety of architectures. The porous matrix can be selectively removed by an appropriate aqueous acid or base, resulting either arrays of tubes/wires or powder. This is very convenient for the characterization of properties. For example, for sensing and nanoelectrode applications, the nanowires can partially remain in the template and function as an array. For single-nanowire applications, dissolving the template produces individual nanowires can be isolated. The nanomaterials can be fabricated in a porous membrane with a controllable morphology. Because the membrane used contains cylindrical pores of uniform diameters and length, analogous monodispersed nano- and microstructures can be obtained in principle. Moreover, in the case of using hard membranes (ordered porous alumina and macroporous silicon) as templates, the templates are rigid and can be easily handled and positioned. In most cases, temperatures below about 550°C the templates do not affect the properties of materials embedded in the templates.

Templates of 1D hosts include mesoporous silica materials (SBA-15 [51] and MCM-42 [52]), carbon nanotubes [53], zeolites [54], polycarbonate membranes, porous alumina membranes [55] [56] and macroporous silicon [57]. The nanoscale channels or pores can be filled by a solution, electrochemistry, a sol-gel, precursor and other methods. 1D tubular and fibrillar structures of metals, semiconductors, polymers and carbon have been generated by this templating method. The porous materials commonly used as templates for the generation of nano- and microstructures, will be discussed in the following sections.

2.2.1 Mesoporous silica materials

With high surface areas and uniform pore sizes, mesoporous silica materials [52] [51] have been widely used as templates for loading catalysts, polymers, metal and

semiconductor nanoparticles that have potential catalytic, environmental, and opto-electrical applications. For instance, Ag nanowires, with diameters of 5 - 6 nm and large aspect ratios can reach to 100 - 1000, within mesoporous silica SBA - 15 was fabricated. However, mesoporous silica materials can only form powder with random orientation but no extended membranes.

2.2.2 Polycarbonate membranes

Polycarbonate membranes with a wide range of pore diameters (down to 10 nm) are available commercially. Although there is uniformity in the pore diameter, the pore length is limited to only 6-11 μm. The problems of this approach are that first of all, the porosity of these membranes is quite low. Second, the pores and hence the wires, can be tilted more than 20° from the direction normal to the template plane. The distribution in the wire orientations can be avoided in laboratory-made templates by appropriately collimating the particle beam. However, the locations of the pores are randomly distributed in general. Moreover, polycarbonate templates also place a limit on the maximum operating temperature of the wire arrays. In the case of organic templates, this can be quite low (140°C for polycarbonate, from Nuclepore date sheet).

2.2.3 Ordered porous templates

Ordered porous templates, especially porous alumina [55] [56] and macroporous silicon [57] are excellent membranes for preparation of 1D nanostructures and microstructures and various of highly ordered arrays of functional nanomaterials have been obtained. The pores in these membranes are highly monodisperse and can be arranged in a regular lattice. The available pores density is as high as 10^{12} pores/cm^2. Accessible Pore diameter in theses membranes rang from a few tens of nanometers to micrometers, details will be introduced in chapter 3.

2.3   Infiltration of porous templates

Various template-associated techniques that are suitable for preparation of nanostructured materials will be reviewed in this section. Methods used to synthesize 1D nanoscaled materials in the pores of the template membranes include chemical vapor deposition (CVD) [58], electrochemical [59] and electroless deposition [60], chemical polymerization and template wetting approaches (polymerization, conversion of precursors and sol-gel) [61].

2.3.1 Chemical vapor deposition (CVD)

CVD has long been applied in the commercial production of solid thin films. The technique entails surface solidification of desired reactants resulting from their gas-phase chemical transformations. CVD processes can be used to deposit a wide range of conducting, semiconducting, and insulating materials [62]. The method has successfully been developed for the template synthesis of carbon nanotubules [63] [64] [65]. The advantages of CVD methods are the ability to controllably create films of widely varying stoichiometry and to uniformly deposit thin films of materials, even onto nonuniform shapes.

2.3.2 Electrochemical deposition

Electrochemical deposition of a material within the pores is accomplished by coating one face of the membrane with a metal film and using this metal film as a cathode for electroplating [66] [9]. This method has been used to prepare a variety of metal nanowires including platinum [67], gold [68], silver [23], cobalt [38], and nickel [9] etc. The volume of the pore is continuously filled up beginning from the pore bottom. Thus, the length of a nanowires can be controlled by varying the amount of material deposited. Hollow metal tube can also be obtained by this method [69] [70]. Conductive polymers, such as polypyrrole, polyaniline, or poly(3-methylthiophene), can also be synthesized within the pores by electrochemical deposition [71] [72]. The electrochemical deposition offers a unique advantage, that is the ability to fabricate composition modulation along the wire's length, making nanowires with segments of different materials. For example, sub-micrometer metallic barcodes were fabricated by growing one nanowire segment, changing depositon solution, growing another nanowire segment, and repeating, thus alternating Au and Ag segment along the length of a nanowire [73]. Muli-layer nickel-copper nanowires with varying segment thickness were also obtained using this method [74]. However, electrochemical deposition has some limitations, such as the range of attainable materials, aspect ratios (which is defined as pore-length/pore-diameter ratio), and a bottom electrode is always required, which complicates the preparation procedure. Moreover, often an uneven layer covering the surface of the alumina membrane is present after electrochemical deposition, which can not easily be removed. In addition, in the process of preparation of nanowire segments, the two metals will be slightly alloyed due to the codeposition of a small amount of the other component.

2.3.3 Electroless deposition

Electroless deposition involves the use of a chemical agent to plate a material from the surrounding phase onto a template surface [23] [75]. This method differs from the electrochemical deposition in that the surface to be coated does not need to be conductive. The material deposition in the pores typically starts at the pore wall. Therefore, after short decomposition times, a hollow tubule is obtained within each pore, whereas long deposition times result in solid nanowires. Unlike the electrochemical deposition where the length of the metal nanowire can be controlled at will, electroless deposition yields structures that cover the complete thickness of the template membrane. The inside diameter of the tubules can be controlled by varying the deposition time. Of course, the outside diameter is determined by the dimensions of the pores in the matrix. The limitation for the electroless deposition is that the pore walls must be modified, and often inhomogeneous walls are obtained.

2.3.4 Template wetting

Template wetting is the most general and versatile template-assisted approach. Nearly all the materials that can be dissolved or melt can generate 1D nano- and micromaterials within the cavities of the template. A general procedure for template wetting is as follows: when a kind of precursor solution/solid powder is brought in contact with porous materials (ordered porous alumina or macroporous silicon) at ambient conditions, the precursor (sol-gel, polymer etc) solution spreads on the template surface, and the pores are thus filled with the liquid. The formed structures can be converted to the target compound by a subsequent thermolysis. Numerous nanomaterials have been successfully fabricated by this approach, for example, polymers [76] [25], metals [77], semiconductors [78], and ferroelectric oxides [6].

The template-assisted method is very successful in terms of controlling the morphology and arrangement of nano- and microobjects. The diameter, length, and aspect ratio of the obtained structures are fully controlled by the templates used. However, the main weakness is, the poor control of crystallinity of the produced nanostructures and microstructures although some specific properties, like mechanical and electrical properties, are strongly effected by the crystallinity of the structure. This could limit their potential applications related to electronic transport. A general requirement for any successful preparative methodology is to be able to achieve nanometer scale control in morphology while maintaining a good overall crystallinity. Therefore our aim is to develop a generic process based on the template wetting

method to improve the quality of nano- and microstructured materials. This allows extending the range of highly ordered arrays of functional 1D nano-scaled materials with low defect density and high aspect ratio and integrate them into nanodevices as functional building blocks used in future nanoscience and nanotechnology.

2.4   Summary of the chapter

In this chapter, the existing approaches and previous work on the synthesis of 1D nanostructures and microstructures was reviewed. Each approach was highlighted by at least one example. The advantages and drawbacks of the different approaches were briefly discussed. Overall, it is concluded that the method of template wetting associated with ordered porous templates is the most versatile approach for the fabrication of 1D nanostructures and microstructures.

CHAPTER III

Fabrication of Ordered Porous Templates

As described in chapter 1, the goal of this thesis is to develop a generic procedure for the production of high quality functional 1D nanostructures and microstructures by templated high-temperature conversion using ordered porous materials as templates and reactants. In additional,the resulting structures should be characterized with respect to various relevant properties. In this chapter, the fabrication and characterization of the templates used in templated high-temperature conversion will be discussed. The templates selected for the proposed approach are ordered porous alumina and macroporous silicon, the reasons are:

- High surface energy at the inner pore walls: their pore walls have a high surface energy [79], as required to conduct the wetting (Si is covered by a native oxide layer under ambient conditions). Strong adhesive forces drive the precursor into the pores when it is brought into contact with the surface of such porous templates.

- Controlled morphology: these porous materials possess highly ordered arrays of pores with monodisperse pore diameters and a high aspect ratio. The currently accessible pore diameters (Dp) of porous alumina range from 15 nm to 400 nm, those of macroporous silicon from 370 nm up to a few microns as indicated in Figure 3.1. The length of pores can be varied from a few hundreds of nm up to a few hundreds of microns. Both template systems contain highly ordered arrays of straight pores with sharp diameter distribution and uniform depth.

- Easy fabrication: with existing technologies, these templates can be fabricated in sufficiently large quantities for relevant properties.

In the following sections, the fabrication processes of ordered porous alumina and macroporous silicon will be described.
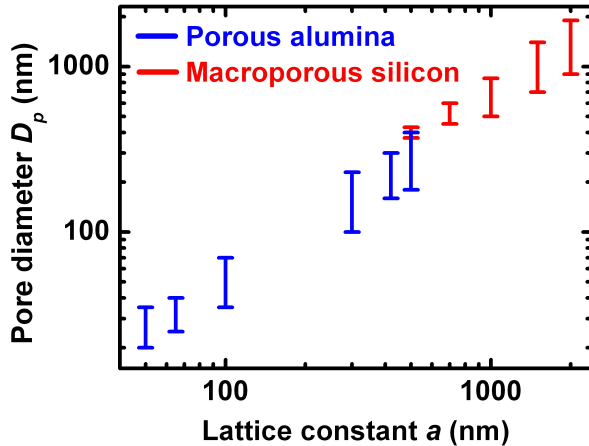
Figure 3.1: Overview of the pore diameters (D_p) and lattice constant (D_{int}) of the currently available highly ordered templates of porous alumina (red bars) and macroporous silicon (blue bars)

3.1 Ordered porous alumina

3.1.1 Order in alumina membranes

According to the order of pores arranged in alumina membranes, porous alumina can be classified into three categories: disordered porous alumina, ordered porous alumina with polycrystalline degree of order as well as long-range ordered porous alumina.

3.1.1.1 Disordered porous alumina

Disordered porous aluminum oxide has been used for the eloxation of aluminum for over 100 years. In this process, the aluminum is potentiostatically anodized in diprotic acids (mostly sulfuric acid, oxalic acid, phosphoric acid, or chromic acid), the details of the anodization process will be discussed in section 3.1.3. An interesting feature of electrochemical oxidation of alumina is that tubular pores forms along the current lines. The pores are random in the shape and packing, and there is some heterogeneity in size. Thus the average distance is determined by the applied voltage. This is a result of the pores nucleating from random pits and valleys on the aluminum surface. A detailed discussion of the pore formation process can be found in the literature [80] [81]. The pore diameters typically lie between 15 nm and 400 nm, with a dispersity (calculated by dividing the standard deviation by the mean pore diameter) of at most 20%. The SEM image in Figure 3.2 is a typical top view of a disordered porous alumina membrane, with a pore diameter of 60 nm and a average distance of 165 nm. The Fourier transform (Fig. [80], inset) indicates that the degree of order of the pore array is amorphous, i.e., the Fourier transition contain an amorphous halo. The Dp-value is not constant along individual pores and the pore array may exhibit
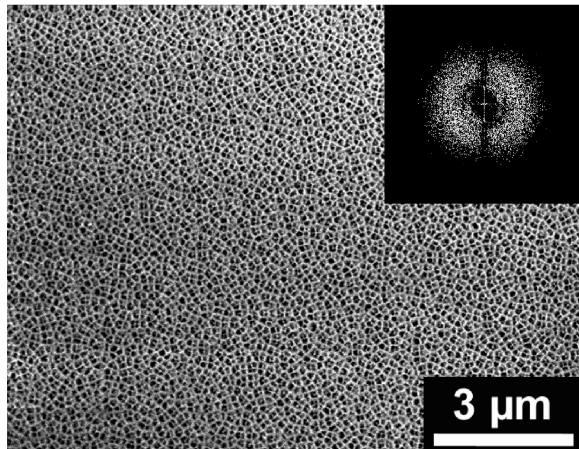
a sponge-like morphology.

Figure 3.2: SEM image of a commercially available porous alumina membrane with randomly arranged pores and a pore diameter of 60 nm. Inset: Fourier transition

3.1.1.2 Self ordered porous alumina

One hundred years after the first patent for disordered porous aluminum oxide [82], Masuda and Fukuda were able to produce self-organized pore structures [55]. A systematic investigation suggests the self-organization is induced during pore growth by lateral forces resulting from the expansion in volume on the conversion of aluminum to aluminum oxide [83]. Self-organized pore growth leads to a nearly perfect, densely packed two-dimensional hexagonal pore structure for a narrow set of processing parameters [83] [84]. Self-ordering phenomena in porous alumina are only observed under specific anodization conditions. To accomplish self-ordered pore growth, the electrolyte and the process parameters such as temperature and voltage have to be selected in such a way that the 10% porosity (fraction of the whole membrane surface taken up by pore openings) rule is obeyed [85]. In a two-step process [55], self-organized pore structures with a polycrystalline degree of order can be produced. The details will be discussed in the following anodization section 3.1.3. The distances between the centers of the pores a (the lattice constants) can be controlled by the applied voltage and the add acid. The domains typically extend 10 to 20 lattice constants and the dispersity of the pore sizes distribution is 8%. The initial porosity of 10% can be increased by wet chemical processes after anodization. For example, the pore diameter for porous aluminum oxide with a = 500 nm after anodization can be increased from D_p = 180 nm to 400 nm in a controlled manner by means of isotropic etching (Fig 3.3). The Fourier transform (Fig. 3.3, inset) indicates a polycrystalline degree of order. Ring patterns up to the fourth order appears in the Fourier image.
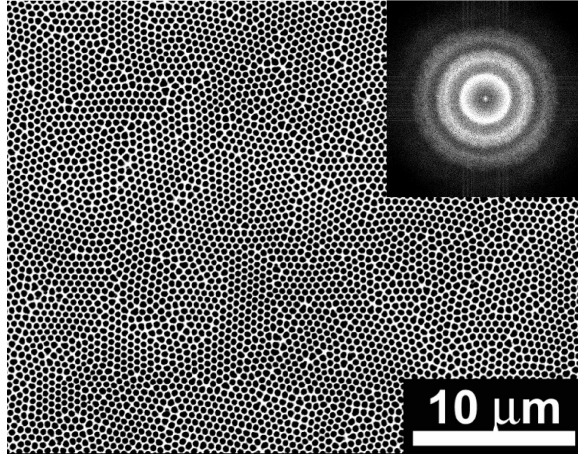
Figure 3.3: SEM image of a self-ordered porous alumina fabricated by a two-step anodization with a pore diameter of 400 nm after an additional pore widening process. Inset: Fourier transition

3.1.1.3 Long-range ordered porous alumina

Self-organization combined with lithographic methods makes it possible to produce extensive monodomains of pores with lateral dimensions ranging into the square centimeter range. Due to its nanoroughness, direct electron beam lithography on aluminum gives unsatisfactory results, whereas hard nanoimprint lithography processes may overcome this problem [86] [87]. Pore formation is initiated in the preformed indentations gives rise to highly ordered, monodisperse pore arrays. The lithograpically introduced pattern was to match the lattice constant of the self-organized pore growth. Attainable pore diameter dispersities are below 2%. A good review of the theory of his process can be found in the dissertation of J. Choi [88].

3.1.2 Pre-treatment of aluminium substrates

High-purity aluminum in the form of chips (99.99%) was the starting material for alumina templates. Aluminum oxidizes naturally in the atmosphere to form a very thin layer of alumina, Al_2O_3, which adheres strongly to the metal's surface, protecting it from further reaction. The first step in this fabrication process is to clean the aluminum sheets that are being used. This process starts with sonification of the chips in pure acetone in ultrasonic for bath for 5 min. Then the aluminum is rinsed in deionized (DI) water and isopropanol. Subsequently, the chips are immersed into a solution containing 50 ml H_5O + 20 ml HCl + 10 ml HNO_3 + 1 ml HF + DI water = 100 ml at 60°C for 5 s. The HF is used to strip off the native oxide on the sheets. Finally, the aluminum chips are annealed at 500°C for 3 h in a nitrogen atmosphere.

Because the alumina film is converted directly from the aluminum metal, a rough metal surface will produce a rough alumina film. To improve the order of the pore

array formed upon subsequent anodization, a polishing step is required. The polishing is usually performed electrochemically in an acid electrolyte (25% $HClO_4$ + 75% C_2H_5OH). A mechanical polishing may be needed if the surface of aluminum is scratched or pitted. Concentrated acid electrolyte solutions favor immediate dissolution of the alumina. After electro-polishing, the aluminum sheets are rinsed under flowing DI water.

3.1.3 Anodization

Anodization is known as a process of electrochemical oxidation. As introduced in the former section 3.1.1, porous alumina can be obtained by anodizing aluminum in an aqueous electrolyte of polyprotic acids (sulfuric acid, phosphoric acid, or oxalic acid) at constant voltage. Anodization of aluminum to obtain porous oxides is a well-established technique and has been reported extensively in the literatures [55] [89]. The pore formation mechanism is schematically displayed in Figure 3.4.
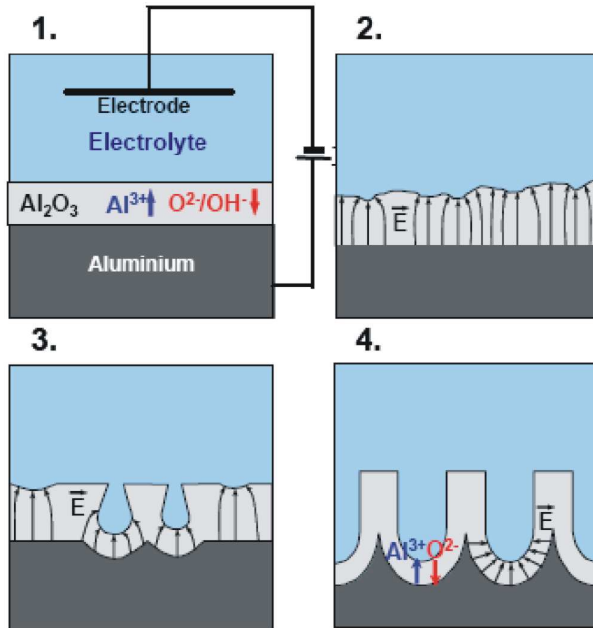
Figure 3.4: Schematic diagram of the pore formation at the beginning of the Al anodization. Regime (1) formation of barrier oxide on the entire area; regime (2) local field distributions caused by surface fluctuations; regime (3) creation of pores by field enhanced or/and temperature-enhanced dissolution; regime (4) stable pore growth [88]

The pore formation mechanism consists of four regimes. At the beginning of the anodization, a thin non-porous layer of alumina is formed on top of the aluminum. This is the so called barrier film, consisting of non-conductive oxide (= 10^{10} x 10^{12} Ω cm [90]), which covers the entire surface of the aluminum (regime 1 in Fig. 3.4). As the anodization continues, the electric field gets locally focused because of the presence of fluctuations of the surface (regime 2 in Fig. 3.4). This leads to field-enhanced or/and

27

temperature-enhanced dissolution in the formed oxide and thus an array of pores develop on the alumina layer (regime 3 in Fig. 3.4). Some pores stop growing due to competition among the pores. Finally, the system reaches an equilibrated state. In this stage, pores grow in a stable manner (regime 4 in Fig. 3.4). The depth of the pores increases as the anodization is continued. The pore diameter depends on the type of acid used and the applied voltage. The concentration of the electrolyte is also important. To keep the reaction rate low, the electrolyte is chilled to between 0°C and 4°C. The most important parameter in determining the final pores size of the alumina film is the applied voltage. Smaller pore sizes require low applied voltages and therefore require more highly conductive electrolytes. When proper electrolyte choice and temperature control constrain the current density between 1 and 6 mA/cm^2, the pore area is observed to be $\sim$1.4 nm^2/V of the applied voltage. The relationship between anodization voltage U and interpore distance D_{int} was found:

$$D_{int} = Dp + 2\alpha U$$

where Dp is the diameter of the pores, α is a proportionality constant of approximately between 2.5 and 2.8 nm/V.

As discussed in section 3.1.1, in the anodization process the pores are somewhat random in their shape and packing in the initial stages of pore growth. Whereas as pore growth continues, the pores self-organize into a hexagonal array and the pores become highly monodisperse. Thus, to obtain a self-organized pore structure, a two-step anodization process [55] is necessary. The first step is growth of alumina film for sufficient time to allow self-organization and homogenization of pore size arranged in a hexagonal lattice. The interface between the alumina and the aluminium adopts hemispherical shape of the pore bottoms. That film is then removed with acid, leaving a regularly arranged array of indentations in the underlying aluminum. These indentations are seeds for the generation of an ordered pore array during a second anodization step. The aluminum is re-anodized at the same voltage and in the same electrolyte as the original anodization. The pores nucleate in the pits and thus are already highly ordered and monodisperse, and continue to grow as patterned.

3.2   Macroporous silicon templates

Since the first successful preparation of macroporous silicon in the early 1990s, very regular ordered pore structures in silicon have been obtained by a photoelectrochemical etching procedure of lithographically pre-patterned Si wafers [57]. In this process,

the silicon oxides or fluorides formed in the oxidation of silicon dissolve in an electrolyte containing hydrofluoric acid [91]. The processes involved are relatively complex and are extensively discussed in the literature [57] [91] [65]. The growth conditions for both n-silicon [91] and p-silicon [92] have been extensively investigated in recent years.
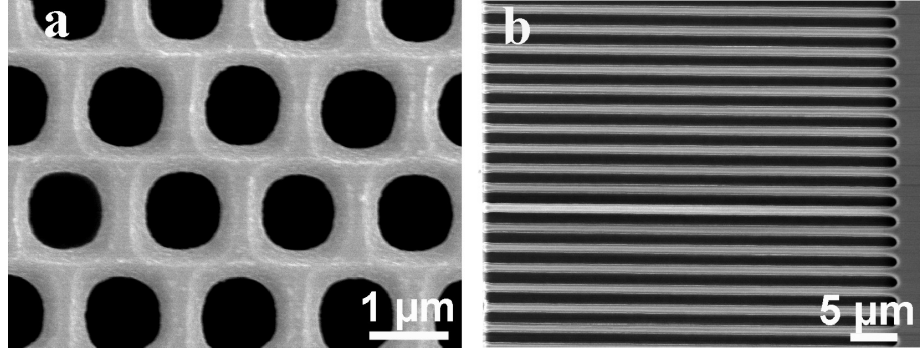

Figure 3.5: SEM images of perfectly ordered n-type macroporous silicon with pore diameter of 1 μm and pore length of 100 μm (a) Top view and (b) Cross-section view.

Nowadays, transferring the lithographic pattern into the silicon by means of photo-electrochemical etching yields a monodomain of pores with sharp size distribution and extensive pore monodomains with lateral dimensions reaching the square centimeter range [57] [65]. The distance between pores can be set anywhere from a=500 nm to a=20 μm by variation of the process conditions, but not independent of the pore diameters. The arrangement of these pores can be controlled by the lithographic mask. They can be a hexagonal or quadratic lattice. The pore diameter, ranging from 370 nm to 4 μm as fabricated at MPI-Halle, is controlled by the illumination intensity. The pores are nearly perfectly vertically aligned. The pore depths are only limited by the thickness of the wafers used as substrates and can reach several hundreds of microns [57] [84], thus providing excellent aspect ratios over 500 [93]. The dispersity of the pore diameter distribution is less than 1%. Figure 3.5 shows SEM images (top-view and cross-section view) of a macroporous silicon sample having a photo-lithographically-defined hexagonal pore arrangement. It has an interpore distance of 1.5 μm and a depth of 100 μm and exhibits hexagonal monodomains of pores at the wafer scale.

3.3   Summary of the chapter

In this chapter, the fabrication process of two different porous templates, ordered porous alumina and macroporous silicon, were introduced.

CHAPTER IV

Structure Characterization

In this chapter, the properties and structural characterization techniques, including electron microscopy, energy-dispersive X-ray analysis, electron energy loss spectroscopy, X-ray diffraction and photoluminescence spectroscopy will be introduced. These methods and techniques will be used in the next chapters for the fabrication and characterization of 1D nano- and micro-objects.

4.1 Release of tubes and wires from the porous templates

In order to study the morphology and properties of 1D nano- and microstructures, it is necessary to get released tubes or wires as powders or free-standing tubes or wires with one end embedded in the matrix. In case of macroporous silicon templates, the silicon can be dissolved in a strong base such as aqueous potassium hydroxide (KOH). In the case of porous alumina templates, the selective etching can be realized via a controlled process by using solutions of either a base such as KOH, or an acid such as H_3PO_4. The details are discussed in the following section:

- In case of macroporous silicon as template matrix, it can be etched with 30-wt% KOH. To prepare free-standing tubes or wires arrays with one end in the macroporous silicon matrix, a drop of KOH solution was put onto the template surface at ambient condition for at least 1 hour. The length of the released tube and rod segments can be controlled by the etching time. Thus, arrays of aligned partially released microstructures, which are still partially embedded within the macroporous Si, can be obtained. To remove residual KOH, the whole wafer was put in a beaker and washed several times with diluted hydrochloric acid, deionized water, and ethanol successively. To obtain released tubes as a powder, we removed the residual material on the top of the template prior to etching. Then the template was immersed into cuvettes filled with aqueous KOH at 90°C for 40 to 50 minutes. The resulting suspension within the cuvettes was centrifuged after the complete decomposition of the matrix material. Then,

the lye was removed with a syringe. The powder samples were washed by adding deionized water. After centrifuging, the liquids were separated from the precipitation. Finally, we prepared as suspensions for further characterizations of the 1D nanostructure and microstructures.

- In case of porous alumina as template matrix, 30 wt-% KOH solution was also used for etching away the alumina membrane. The process of preparation free-standing arrays within the alumina template is similar to that of macroporous silicon, but a relatively shorter etching time, of the order of 30 to 40 min, was applied. To obtain released tubes or wires as a powder from the alumina template, the underlying aluminium was first removed by dipping the whole template into $CuCl_2$ + HCl solution. After carefully washing the remaining alumina membrane, it was etched with 30 wt % KOH solution for 40 min within the cuvettes at 70°C. Then, the KOH solution could be replaced by de-ionized water carefully after several cycles of centrifuging and removing the lye until the pH value of the solution reached 7. A shaking of the cuvettes made the aggregation of the tubes disappearing so that a homogeneous suspension formed, containing wires of the target materials.

4.2   Scanning electron microscopy (SEM)

In a field-emission SEM microscope, electrons accelerated through a voltage difference between the cathode and the anode that may be as low as 0.1 keV or as high as 30 keV. An electron probe has a diameter of 1-10 nm carrying an electron-probe current of 0.5 nA to 1 pA is formed at the specimen surface. Various electron-specimen interactions generate a great deal of information in the form of emitted quanta, all of which can be used in the different imaging and operating modes of a SEM. In this thesis, SEM investigations were carried out using a field-emission scanning electron microscope (JEOL JSM 6300F or JSM 6340F) operated at accelerating voltages ranging from 5 to 8 kV.

SEM investigations are not demanding on specified specimen preparations. The specimen can be observed at different stages. In our experiments, SEM investigations were performed from the initial templates over the the free-standing tube or wire arrays within the templates matrix to the completely released wires/tubes deposited on a highly conductive substrate (Si wafers).

4.3 Transmission electron microscopy (TEM)

TEM is a leading technique for nanostructure characterization. A variety of signals generated by the electron beam passing through the specimen can be used to extract useful information about its structure, chemical composition and bonding at the nanometer scale and even at the atomic level. The electron optics of electron microscopes can be used to produce images of electron density emerging from the back side of the sample. For example, variations in the intensity of electron diffraction across a thin TEM sample, called "diffraction contrast", are used in imaging defects, interfaces, and second phase particles. Beyond the diffraction contrast there is high resolution transmission electron microscopy (HRTEM). In HRTEM, the phase of the diffracted electron wave is preserved and interferes constructively or destructively with the phase of the transmitted wave. This technique of "phase contrast imaging" is used to form images of the profiled lattice structures. TEM is such a powerful tool for the characterization of materials that some microstructural and nanostructural features are defined largely based on their TEM images. The following sections will give a brief introduction of the conventional TEM and the high-resolution TEM.

4.3.1 Electron diffraction

In a TEM the illumination source emits electrons, which get accelerated into the microscope column. A set of condenser lenses form a parallel electron beam, which illuminates the electron transparent specimen. TEM is predominantly used for bright field imaging and obtaining diffraction patterns. The electron diffraction pattern (ED) provides important information on the atomic or molecular crystal lattice subunits of the specimen. The spacings between lattice plane reflections on an ED pattern gives information on the crystal structure of the samples investigated. The spacing between lattice planes can be calculated from the diffraction pattern using the equation: $rd = L\lambda$, where d is the spacing between crystallographic planes, λ is the wavelength of electron, L is the camera length and r is the distance from the center spot to the related diffraction spot on the negative. The calculated d value can be compared to the values obtained from a X-ray diffraction pattern. Thus the lattice plane direction and spacing corresponding to each diffraction spot can be determined. From the spots in the ED pattern, the nanocrystal size, morphology, and structure analysis in this thesis were obtained using a JEM 1010 transmission electron microscope operated at 100 kV.

4.3.2 High-resolution TEM

HRTEM is indispensable for examination of specimens with complicated structure (containing several crystallographically different domains, amorphous inclusions, etc). HRTEM is usually performed in the imaging mode with on-axis illumination. To obtain a HRTEM image, a choice of an appropriate objective aperture and its exact centering is essential. The contrast in HRTEM images arises from a phase contrast mechanism, which is due to interference of the electron waves scattered through small angles and not intercepted by the objective. HRTEM micrographs in this thesis were obtained using a JEM 4010 transmission electron microscope operated at 400 kV and CM20 transmission electron microscope operated at 200 kV. The microscope is capable of operating both in conventional TEM and high-resolution TEM mode. Moreover, the small dimension of the electron probe of the CM20 ensures the possibility of performing energy dispersive X-ray spectroscopy (section 4.3.3) and electron energy loss spectroscopy analysis (section 4.3.4) of a sample at high spatial resolution simultaneously with the imaging.

4.3.3 Energy-Dispersive X-ray Analysis (EDX)

When fast electrons from the electron source interact with the specimen, they will be scattered, and the scattering can be elastic or inelastic. The scattering may involve many atoms of the specimen. In case of inelastic scattering the resulting inner shell ionization carry characteristic information of the chemical species in the form of emitted x-rays. Energy dispersive X-ray spectrometers are designed to detect the X-rays emitted upon inner shell ionization caused by interactions of the specimen with the incident electrons. The use of windows (usually consisting of a very thin beryllium foil) shield in the EDX detector from atmospheric pressure prevents since the analysis of light elements can not penetrate the window foil. Also, since the probability of emitting an X-ray instead of an Auger electron increases with the element atomic number, EDX is particularly useful for detecting heavy elements [94]. The geometry of the objective pole in most of the TEMs prevents bringing the detector close to the specimen, which results in a poor count rate and makes quantitative X-ray analysis difficult. Tilting the specimen towards the detector helps improving the collection and enhances the count rate. The spatial resolution of EDX in TEM is mainly determined by the probe size, but using a probe size smaller than 0.5 nm produces too low a counts rate. Increasing the acquisition time can make specimen drift significant. Therefore, EDX is very hard to use to quantify chemical composition of the sub-nanometer

features in the specimen.

The microscope CM20 (Philips) is capable of analyzing not only individual points in the specimen, but can produce X-ray maps in which the intensity of the signal is directly related to the particular X-ray intensity. This capability is very useful when investigating specimen of unknown composition and spatial distribution of chemical elements for the first time. In case of heavy elements, especially the ones that have unsuitable EELS edges, EDX might provide the only possibility of chemical identification.

4.3.4 Electron energy loss spectroscopy (EELS)

EELS is used for the analysis of the energy distribution of electrons that have interacted inelastically with the specimen [94] [95]. The EELS spectrum presents the relation between the intensity and the energy-loss of the electrons, emitted from the field-emission source, after passing through the specimen. Normally, the EELS spectra need to be processed before any quantitative analysis can be done. After the raw data are collected, the energy scale is first calibrated, and then the background of the spectrum is removed according to the power-law background model. In order to get rid of the influence of plural scattering, a Fourier-ratio method needs to be used. Typically, an EELS spectrum includes the zero-loss peak (which has no energy loss), the plasma peak (which is scattering from the outer-shell electrons, typically from 5-50eV) and characteristic peaks with sharp edges (which is scattering from inner-shell electrons, the edge position is approximately the binding energy of atomic shell), the edge position depends on the atomic number. So the position indicates which kind of element is present in the sample. And sometimes, the edge also has fine structure, which represents the energy-band structure. So EELS can provide information about the atomic species in the specimen, such as their electronic structure, bonding, nearest neighbor distances, and the specimen dielectric response. EELS in TEM is considered to be an increasingly important analytical tool for the detection of light elements at high spatial resolution [95] [96]. EELS element edges are more distinctive than those of EDX. Moreover, the edge fine structure of EELS is related to the bonding structure. Whereas EDX can be used in connection with a SEM or a TEM, EELS can only be used in connection with a TEM. This is because the transmitted electrons are probed.

4.3.5 TEM specimen preparation

Unlike SEM, the specimen preparation for TEM investigations is more complex. Some the details are listed below:

- For a conventioned TEM investigation, aqueous suspensions of released nano-objects were directly placed on TEM grids with a perforated carbon film.

- To prepare the cross-sectional specimens, an aliquot of the tubes/wires suspension was transferred into conical moulds. After the water had been evaporated, the tubes/wires were embedded in epoxy resin (Durcupan ACM). The resin was cured at 65°C for 48 h. Slices with a thickness of 70 nm or less, as ascertained from their interference colors, were prepared using an ultramicrotome equipped with a diamond knife. The slices were transferred onto copper grids with perforated carbon films.

- Since the nanostructures studied were grown in nanoscale holes, for a confined geometry (cross section or plan view, tubes/wires within the templates) observation, the only technique capable of investigation the growth interface is cross-sectional TEM (X-TEM). The X-TEM sample preparation may start from the initial sectioning and finishing with the ion milling. Initial sectioning of appropriately sized pieces of material can be done using a diamond saw or a diamond knife. The next step is to clean two approximately equally sized square pieces of material, first in acetone (to remove wax residue) and then in isopropyl alcohol (to degrease the surface). After this, glue should be applied to the pieces, turned 90° relative to each other if possible (to obtain two different zone axis directions in the specimen) and glued face to face to protect the interface and clamps to ensure the glue line to be as thin as possible. Then the sample is glued onto the polisher with the polishing plan forming a certain angle to the glued cross-section surface during polishing. Therefore, a wedge forms during polishing. As the polishing proceeds, the thinner end of the wedge is thin enough to be transparent to electrons, while the thicker end is strong enough for sample handling the sample. Ion milling is the final and the most critical method of the conventional TEM specimen preparation.

4.4   X-ray diffraction (XRD)

X-ray diffraction is used to determine the crystal modification of any kind of crystalline material. The wavelength of x-rays is between 0.01 nm and 10 nm, the same

order as that of the atomic spacing in the crystal ($\sim$ 0.3 nm). Therefore X-rays are ideally suited for probing the structural arrangement of atoms and molecules in wide range of materials. XRD measurements are carried out on the samples containing either nanoobjects aligned within the pores of membranes or powders of wires/tubes liberated from the pores and deposited onto (100)-oriented silicon wafers. In the case of nanoobjects within the membranes, before the XRD measurement was taken, the surface of the as-grown sample was cleaned by a scalpel or polished with a slurry of alumina particles in case of a crystalline thin film formed on the sample surface. Then the sample was placed in the diffractometer in such a way that the template surface with the pore openings was arranged perpendicular with respect to the plane defined by the incident and scattered x-ray beams (Fig. 4.1). In the reflection geometry the pore axes lie in the plane of incident and scattered X-ray beams. In the $\theta/2\theta$ geometry, only crystals will contribute to the detected scattering intensity which are oriented in such a way that the corresponding lattice planes are parallel to the template surface (perpendicular to the pore axis). The XRD measurements in the thesis were performed with a Philips X'pert MRD diffractometer with a cradle and secondary monochromator for CuKα radiation with a wavelength of 1.5406. The $\theta/2\theta$ scans are carried out in reflection mode with a 2θ increment of 0.05° and an integration time of 20 s.
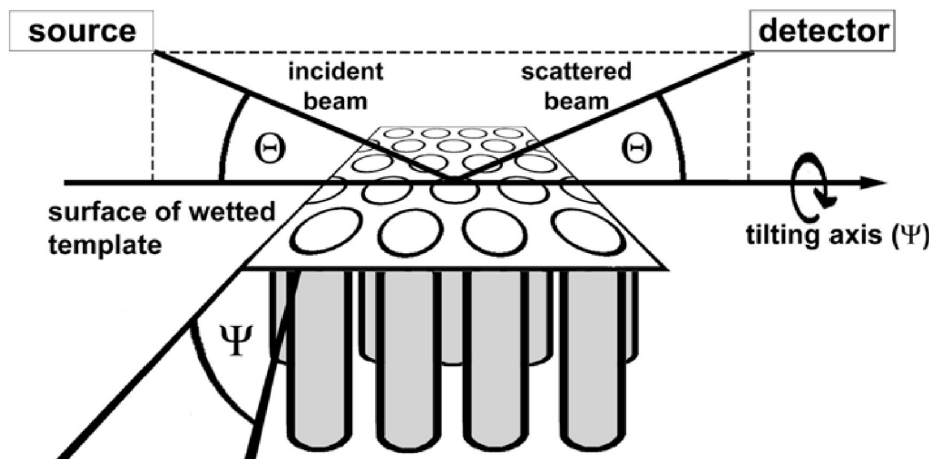

Figure 4.1: Schematic depiction of the setup used for the X-ray diffraction experiments. For the $\theta/2\theta$ scans, the samples were placed in the equipment in such a way that the surface of the wetted template was oriented perpendicular to the plane of incident and scattered X-ray beams. To perform the ψ scans, the setup was adjusted to selected 2θ angles. Then, the samples were tilted by an angle ψ around an axis defined by the intersection of the template surface and the plane of the incident and the scattered X-ray beam. The scattering intensity was measured as a function of the tilting angle.

To investigate texture of the samples, orientation distributions of specific sets of lattice planes were measured by means of ψ scans. The settings of θ (incident beam) and 2θ (detector) were fixed to specific values corresponding to the maximum intensity of the corresponding reflection. The sample was tilted about the axis defined by the intersection of the plane of the incident and the scattered x-ray beams with the template surface (Fig. 4.1), ψ equals zero if the two planes are oriented perpendicularly. The scattering intensity is measured as a function of tilting angle ψ. This method allows to analyze orientational distribution of sets of lattice planes of crystallographic directions with respect to the pore axes.

4.5   Photoluminescence spectroscopy

Photoluminescence (PL) spectroscopy is a contactless, nondestructive method of probing the optical properties of materials. Light is directed onto a sample, where it is absorbed and imparts excess energy into the material in a process called photo-excitation. One way this excess energy can be dissipated by the sample is through the emission of light, or luminescence. In the case of photo-excitation, this luminescence is called photoluminescence. The intensity and spectral content of this photoluminescence is a direct measurement of various important material properties. Photo-excitation causes electrons within the material to move into permitted excited states. When these electrons return to their ground states, the excess energy is released and may include the emission of light (a radiative process) or may not (a nonradiative process). The energy of the emitted light (photoluminescence) relates to the difference in energy levels between the two electron states involved in the transition between the excited state and the equilibrium state. The intensity of the emitted light is related to the relative contribution of the radiative process. PL can be used for band gap determination, which is particularly useful when working with new compound semiconductors. Radiative transitions in semiconductors also involve localized defect levels. The photoluminescence energy associated with these levels can be used to identify specific defects, and the amount of photoluminescence can be used to determine their concentration. Thus, material quality can be measured by quantifying the amount of radiative recombination. Moreover, analysis of PL helps to understand the underlying physics of the recombination mechanism.

PL spectroscopy was carried out on either free-standing tubes or wires with one end embedded in the porous matrix, or on completely liberated tubes or wires deposited on a silicon wafer. The PL spectra was measured at room temperature using a

He-Cd Laser ($\lambda = 325$ nm, power of 15 mW) as an excitation source. The integration time was 0.2 s and the slit size 300 μm. A standard single-grating monochromator was used to disperse the luminescence light onto a detector. The visible range was detected by a liquid nitrogen cooled CCD camera. and the infrared range was collected by a Ge detector (Edinburgh Instruments). The laser beam was modulated on-off at 27 Hz by a chopper, and the signals were amplified by standard lock-in techniques. All the spectra were calibrated for the spectral response of the set-up used.

4.6   Summary of the chapter

A primary objective of this chapter was to provide a brief description of the techniques, including TEM, HRTEM, EDS, EELS, XRD and PL. These methods and techniques will be used for structure characterization and properties investigation of 1D nano- and micro-structures in the next chapters.
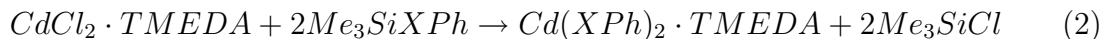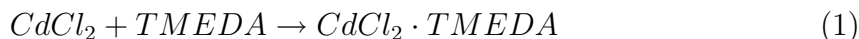
CHAPTER V

One-dimensional nanostructures and microstructures by templated thermolysis of organochalcogenolates

One-dimensional nanostructures and microstructures have received much attention due to their distinct properties and potential applications in nanoscale electronics and optoelectronics [97] [98]. The use of porous templates containing aligned nano-pores [23] [25] is a versatile method to fabricate arrays of aligned nanowires, predominantly by electro-deposition and electro-less deposition [60]. However, it remains still a challenge to extend the range of functional target materials that can be formed into nanowires with low defect density and high aspect ratios. Arylchalcogenolates of group 12 and 14 metals are a versatile class of single-source precursors with similar molecular architecture and thermal properties, which have been employed to generate II/VI, IV/VI, and III/V compound semiconductors. As discussed in the following, templated high temperature thermolysis of organochalcogenolates inside the pores of templates is a simple and universal method for the preparation of 1D nano-objects. We will show in this chapter that arylchalcogenolates and ordered porous templates (self-ordered porous alumina templates [55] [99] and macroporous silicon [57]) represent a construction kit for the synthesis of 1D nanostructures and microstructures of different types of target materials with varying morphologies.

5.1 Organochalcogenolates as single-source precursors

The synthesis of the precursors focused on a straightforward and efficient preparation of organochalcogenolates of group 12 and group 14 metals such as cadmium, zinc or tin. Homoleptic organochalcogenolates of group 14 elements can easily be obtained as monomeric molecules, whereas organochalcogenolates of zinc and cadmium of the general composition $M(XR)_2$ show a high tendency to form insoluble

coordination polymers not suitable for the infiltration of templates. Thus, ligand-stabilized soluble monomeric complexes such as Zn(XPh)$_2$·TMEDA (X = Se, Te) [100] [101] need to be used. Though the zinc species could be prepared according to literature procedures [100] [101], Schlecht et al. have developed a synthesis of the analogous cadmium compounds [102]. As the solubilities of cadmium halides are much lower than those of zinc halides, complexation with TMEDA (tetramethylethylene-diamine) had to be performed before the substitution of the halide by a silylated phenylchalcogenolate. This synthetic procedure allowed the preparation of the complete series of Cd(XPh)$_2$·TMEDA with X = S, Se, Te using the same experimental protocol (equation 1 and 2) [102]. The crystal structures of Cd(SPh)$_2$·TMEDA and Cd(SePh)$_2$·TMEDA were determined.

$$CdCl_2 + TMEDA \rightarrow CdCl_2 \cdot TMEDA \tag{1}$$

$$CdCl_2 \cdot TMEDA + 2Me_3SiXPh \rightarrow Cd(XPh)_2 \cdot TMEDA + 2Me_3SiCl \tag{2}$$

The decomposition characteristics and the melting points of Cd(XPh)$_2$·TMEDA with X = S, Se, Te were determined by calorimetric measurements. All complexes show decomposition temperatures more than 100°C higher than the melting points, thus providing an extended temperature range for the liquid phase and excellent prerequisites for melt infiltration of templates. Table 1 shows the organochalcogenolates precursors used in this work. We used Cd(SePh)$_2$·TMEDA for the preparation of cadmium selenide (CdSe) nanostructures and microstructures, Sn(SePh)$_4$ [103] as a precursor for SnSe and Zn(TePh)$_2$·TMEDA for the synthesis of zinc telluride (ZnTe) nanostructures. The thermolyses of the organochalcogenolate precursors are similar. For example, the thermolysis of Zn(XPh)$_2$·TMEDA starts with the dissociation of the TMEDA donor ligand (equation 3)[101] [100] [104] [102] [105]. Then the precursor decomposes into target nanoparticles (equation 4).
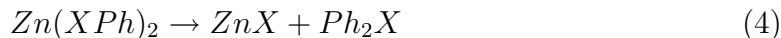
$$Zn(XPh)_2 \cdot TMEDA \rightarrow Zn(XPh)_2 + TMEDA \tag{3}$$

$$Zn(XPh)_2 \rightarrow ZnX + Ph_2X \tag{4}$$

Table 1: Melting points and decomposition temperatures of organochalcogenolates precursors.

precursor	Melting point	decomposition temperature	product
Sn(SePh)$_4$	84°C	250°C	SnSe
Cd(SePh)$_2$·TMEDA	148°C	230°C	CdSe
Zn(TePh)$_2$·TMEDA	123°C	250°C	ZnTe

5.2 CdSe nanostructures: from primary grains to single-crystalline oriented nanowires and polycrystalline microtubes

Nanostructured semiconductor materials are of great interest because of their novel physical, chemical, optical and optoelectronic properties [97] as well as their applications in fabricating nanoscale electronic, photonic, electromechanical and biomedical devices [106] [30]. CdSe is the most extensively studied compound semiconductor in the nanometer range due to the versatile size-tunable properties of its nanostructures. In particular, CdSe nanowires [107] [108] and nanotubes [109] were applied in the fabrication of optoelectronic devices because the power conversion efficiency of nanowires has been demonstrated to be higher than that of quantum dots [108]. Moreover, nanowires with a preferred orientation may produce unique light scattering and polarization effects, which are of considerable interest in the development of microemitters of polarized light and micron-scale polarization sensitive photosensors [110] [111]. It has been reported that invidual CdSe nanorods possess excellent optical properties and up to 100% polarized photoluminescence (PL) [110]. Therefore, a technology that allows for the controllable fabrication of nanowires both arranged in the right place and with the appropriate orientation must be addressed. Shape-controlled synthesis of CdSe nanorods [108] [111] and template assisted synthesis of CdSe nanowires [112] [113] and nanotubes [114] [110] have been demonstrated through electrochemical and chemical approaches. However, most of these nanowires and nanotubes are composed of nanoscale grains, and they are of polycrystalline structure. The grain boundary scattering could greatly affect the optoelectronic performance. Thus, the synthesis of highly crystalline and preferentially oriented nanowires is still

a challenge. In addition, the size and shape of inorganic nanocrystals widely affect their electrical and optical properties [115]. The systematic manipulation of the shapes of inorganic nanocrystals is therefore an important goal in materials chemistry. Prompted by the these, we will in this section demonstrate the synthesis of shape-controlled CdSe nanostructures from nanoparticles over nanorods to single-crystalline nanowires using a templated high temperature conversion approach under condition of wihcih the templates are inert. The crystallization and ripening of these CdSe nanosystems will be systematically studied.

5.2.1 Preparation of CdSe nanowires

CdSe nanowires were fabricated by wetting of ordered porous alumina templates with $Cd(SePh)_2 \cdot TMEDA$, synthesized according to the literature [102]. Four porous alumina templates with a pore diameter of 25 nm and a pore depth of 100 μm were covered with a layer of precursor powder, heated to 160°C at a rate of 2°C/min and kept at 160°C for 2 hours. At this temperature, the precursor melt infiltrated the pores. The wetted template was heated to 500°C at a rate of 2°C/min and held at this temperature for at least 2 hours. This lead to a complete decomposition of the precursor into CdSe nanoparticles. Finally, the template was cooled to room temperature at a rate of 5°C/min. All annealing procedures were performed in corundum crucibles under argon atmosphere. The wetting-crystallization-cooling cycle can be repeated several times to customize the morphology. Took one template out of the oven and repeat the wetting-crystallization-cooling cycle on the rest of three samples. The annealing and cooling processes were the same in each of wetting-crystallization-cooling cycle except the annealing time kept at 500°C (Fig. 5.1). The rest may be deduced by analogy, four wetting-crystallization-cooling cycles were produced on the fourth sample and the accumulated annealing time at 500°C of more than 3 days (Fig. 5.1d). The templates were selectively removed by etching with a 30 wt-% solution of potassium hydroxide at 70°C. The resulting suspension was washed with deionized water until neutrality.

5.2.2 Morphology of CdSe nanowires

Using TEM images of samples taken at different numbers of wetting-crystallization-cooling cycles and at different annealing times, one can follow the shape evolution of the nanostructures. For a given annealing temperature, variations of the annealing time systematically alter the shape of the nanostructures (Fig. 5.1a-d). The
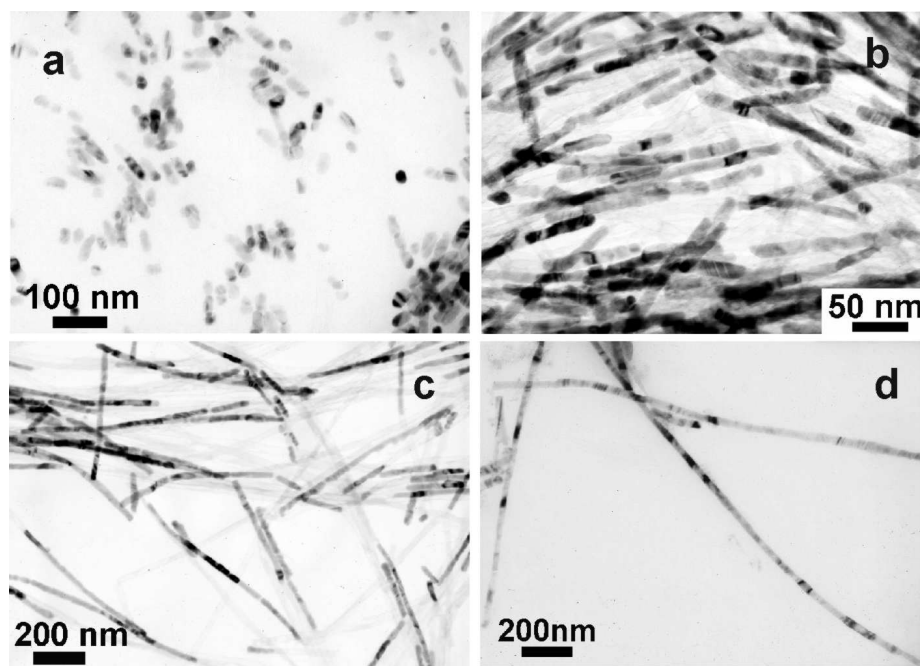
Figure 5.1: TEM images of CdSe samples: (a) Nanoparticles obtained after one wetting-crystallization-cooling cycle and annealing at 500°C for 5h. (b) Nanorods obtained by two cycles and annealing at 500°C for 6 h. (c) Nanorods with higher aspect ratio prepared by three cycles and annealing at 500°C for 24 h. (d) Nanowires obtained after four cycles and annealing at 500°C for 48 h.

CdSe nanoparticles shown in Figure 5.1a were obtained by one wetting-crystallization-cooling cycle and annealing at 500°C for 5 hours. Using two wetting-crystallization-cooling cycles and annealing at 500°C for another 6 hours, nanorods were strongly favored (Fig. 5.1b). Nanorods with a higher aspect ratio formed after three wetting-crystallization-cooling cycles and annealing at 500°C for 24 hours, the accumulated annealing time at 500°C of more than 35 hours (Fig. 5.1c). Finally, nanowires with an aspect ratio up to 75 (Fig. 5.1d) were produced by four wetting-crystallization-cooling cycles and subsequent the annealing at 500°C for another 48 hours, the complete accumulated annealing time at 500°C of more than 83 hours. All nanostructures have a diameter of 25 nm which is inline with the D_p-value of the templates used. It is worth to notice that the annealing time plays a crucial role in controlling the shape of the nanostructures.

5.2.3 Structural characterization of CdSe nanowires

The investigation of the isolated semiconductor nanostructures by HRTEM showed single-crystalline wires without a common growth direction. A preference for an
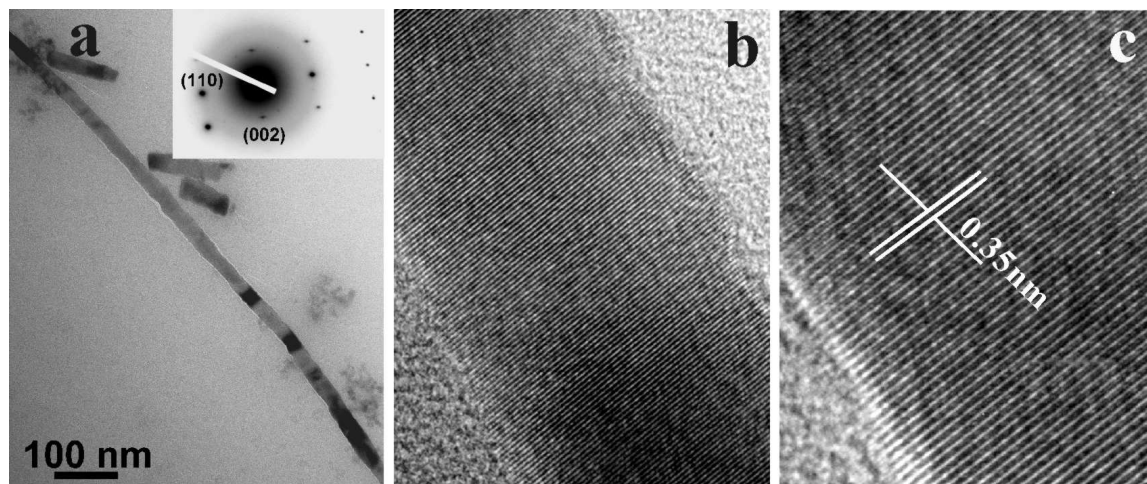
Figure 5.2: (a) TEM image of one individual CdSe nanowire with a diameter of 25 nm, inset: SAED pattern with indexed Bragg reflections for CdSe (b) HRTEM image of the nanowire, (C) Detail showing lattice planes with a spacing of d = 3.5$\mathring{A}$, growth direction is (002).

alignment of the c-axis with the long axis of the wires was observed though, but some other growth directions were also found for a minority of nanowires. For the CdSe nanowires with [001] as the long axis, an inter-planar spacing (dhkl) of 3.50$\mathring{A}$, corresponding to the (002) lattice planes of the hexagonal wurtzite phase of CdSe was observed (Fig. 5.2). Indexing of a typical SAED (selected area electron diffraction) pattern (Fig. 5.2a, inset) of the single-crystalline CdSe wires could be done for this phase as well. The XRD powder patterns of the nanoparticles (Fig. 5.3a) and nanowires (Fig. 5.3b) aligned within the porous alumina membranes confirmed the presence of the wurtzite phase for the complete product. The relative intensity of the (002) reflection of CdSe nanowires (Fig. 5.3b) is higher than that of CdSe in $\theta/2\theta$ scans of aligned nanoparticles and polycrystalline powder, confirming that the c-axis of the hexagonal nanocrystals is preferentially aligned along the long axis of the pores rather than being randomly oriented.

The chemical composition of the CdSe nanowires was characterized using EDX connected with TEM (Philips CM20-FEG). Figure 5.4 reveals that the nanowires are composed of Cd and Se, and quantitative analysis results indicate that the atomic ratio of Cd to Se is very close to the 1:1 stoichiometry. In our experiment, ultra thin amorphous carbon layer covering the CdSe nanowires was found. These carbon films possibly form onto the pore walls of porous alumina if a material containing carbon is pyrolized [116]. In our experiment, this problem has been overcome by a very easy way, that is, by introduction of hexaphenylcyclotrisiloxane ($Ph_6Si_3O_3$) into the
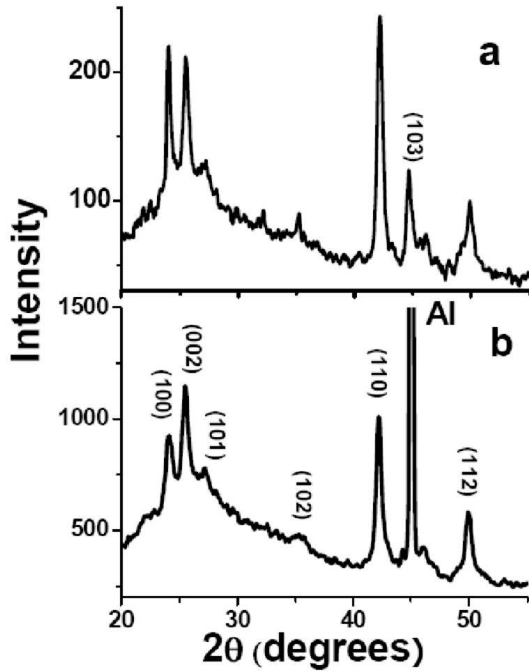
Figure 5.3: X-ray diffraction pattern of (a) CdSe nanoparticles and (b) CdSe nanowires aligned in the porous template ($\theta/2\theta$ mode, indexes for wurtzite CdSe).

precursor system. Thus Si may be released from the pyrolysis of $Ph_6Si_3O_3$ during the annealing process and reacts with amorphous carbon to form a Si/C/O composite shells. These shells are brittle and can be easy removed using sonication, yielding pure nanostructures of CdSe.

5.2.4 Growth mechanism of CdSe nanowires

We propose that the formation mechanism of the CdSe nanostructures can be devided into two stages. In the first stage, many small primary grains form on the pore walls from the molecular precursor. These grains grow to nanoparticles with a certain size distribution. Then, the smaller particles are consumed by the further growth of the bigger ones as the Gibbs-Thomson effect provides a thermodynamic driving force for large particles to grow at the expense of smaller ones [117] [118]. This stage is a typical Ostwald ripening process [119] eventually leading to particles with a diameter close to the pore width. In the second stage of particle growth anisotropic structures such as rods and wires are formed. In contrast to solution systems where the nanocrystals have free mobility in the liqiud phase that allows them to get close and attach to each other ('oriented attachment') [120] [108] [121], the CdSe nanocrystals in our system are confined in one-dimensional pore channels that hinder the nanocrystals from free movement and rotation. Thus, we believe that the growth mechanism of nanowires
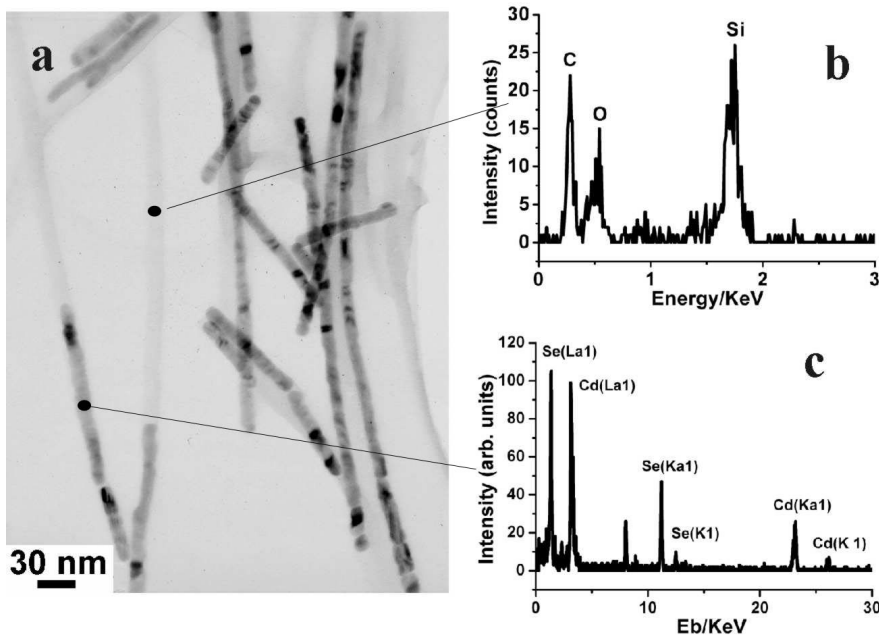
Figure 5.4: Chemical coposition analysis of CdSe nanowires by EDX spectroscopy. (a) TEM images of the investigated nanowire segment. (b) EDX point spectrum measured at the location indicated in (a). (c) EDX point spectrum measured at the location indicated in (a).

occuring in our system is substantially different from the one in solution. A tentative explanation may come from the idea that the transformation of nanoparticles to nanowires is associated with consecutive wetting steps, bringing new precursor material into the pores and with the thermolysis of the precursor melt in the presence of a melt-nanoparticle interface (Fig. 5.5). It can be expected, that the formation of CdSe from the precursor melt will be facilitated at the interface that has the role of a seed for the formation of newly formed CdSe in the second wetting cycle (and in the following ones). It is known from earlier work [102] that the initial state of the degradation of the precursor is the formation of small amorphous grains at 351°C. These crystallize at slightly higher temperatures. When the crystallization is induced by the interface with an neighboring nanoparticle, the crystallization is likely to be epitaxial, giving the newly grown part of the nanostructure the same orientation as the nanoparticle formed in the first thermolysis (Fig. 5.5). This epitaxial growth can occur at every wetting step performed with the templates. Thus, anisotropic elongated nanostructures such as rods or wires can be made stepwise as single-crystals starting from the products of the first thermolysis. The preference for the c-axis as the long axis of the resulting wires can be explained by the fact that the growth of

48

a crystalline phase by attachment of non-aggregated building units is normally favored at the faces with the highest energy [122]. For wurtzite semiconductors such as CdSe this is the (001) pair of facets [123]. When the precursor melt covers different nanoparticles with different orientation in a given template pore, growth will preferably occur at the ones with (001) surfaces, making this orientation the dominant one for the anisotropic products. The same principle holds true for a potential diffusive growth of the nanostructures during the long annealing step at 500°C. This will also favor further crystal growth at (001) surfaces over other orientations.
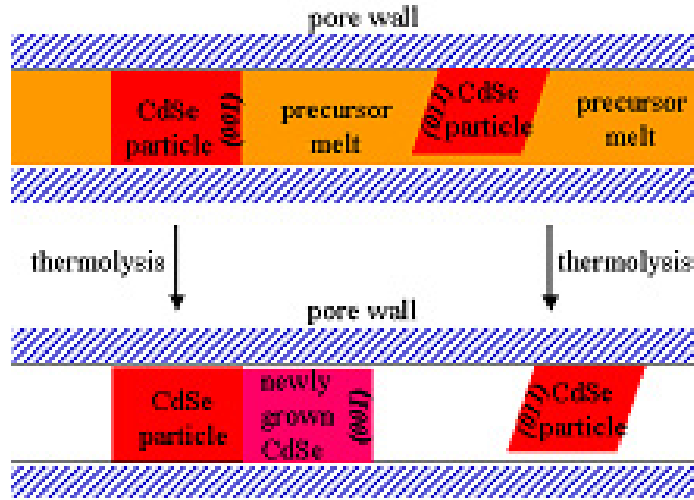

Figure 5.5: Growth mechanism model. Top: precursor-filled template pore in the second wetting cycle. Bottom: elongation of the nanostructures by a preferred growth at the (001) facets of the particles.

5.2.5 Optical properties

For optical characterization, PL measurements were performed at room temperature using a HeCd laser (λ=325 nm, 15 mW) as an excitation source. The PL of CdSe nanoparticles (Fig. 5.6a) and nanowires (Fig. 5.6b) liberated from the alumina template was observed. Both the nanoparticles and nanowires with a diameter of 25 nm exhibit the characteristic photoluminescence of bulk CdSe. The PL spectrum of the nanostructured CdSe centered at 703 nm, coincides with that of bulk CdSe, which has a bandgap of 1.74 eV [124]. The full width at half maximum (FWHM) of the CdSe nanoparticle is around 80 nm (Fig. 5.6a), whereas FWHM of the CdSe nanowires is relatively narrow, about 57 nm, which agrees well with the former results that the nanowires have a higher crystallinity and purity than nanoparticles.
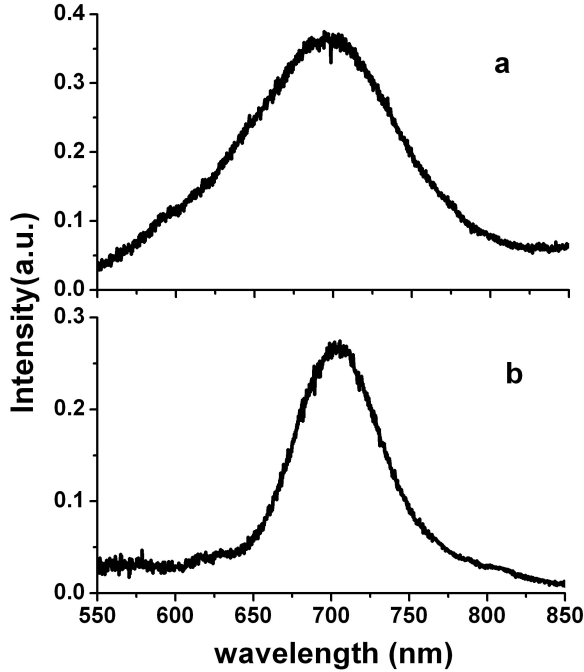
Figure 5.6: Room temperature PL spectrum of (a) CdSe nanoparticles and (b) Nanowires released on a silicon wafer (λ_{max}= 703 nm [124]).

5.2.6 CdSe microtubes

In case of pores having diameters larger than 180 nm, wetting of porous membranes lead to tubular structures, even after long annealing periods (several days). As an examples CdSe tubes prepared by wetting of macroporous silicon are shown in figure 5.7. The tubes were obtained by annealing the wetted macroporous template at 550°C two successive wetting-crystallization-cooling cycles. The SEM image in Figure 5.7a represents the openings of CdSe tubes embedded in the template. Their wall thickness is approximately 90 nm. Completely released CdSe microtubes are depicted in Figure 5.7b. The tubes are grainy and but uniform in diameter.
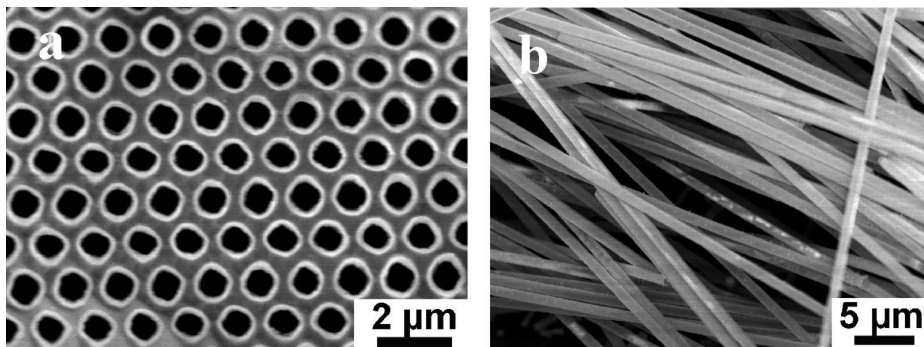

Figure 5.7: SEM image of CdSe microtubes (a) Located in macroporous silicon with a pore diameter of 1 μm. (b) Completely liberated on a silicon wafer.

The details of the CdSe microtube wall formation can be clearly seen in the TEM image in Figure 5.8a. The tube wall is formed by crystalline nanoparticles, which have a size of the order of 50 to 80 nm. Figure 5.8b is the corresponding SAED pattern. The strong reflection rings in the image can be assigned to wurtzite CdSe, which is the same phase as that of the single-crystalline nanowires obtained by wetting ordered porous alumina.
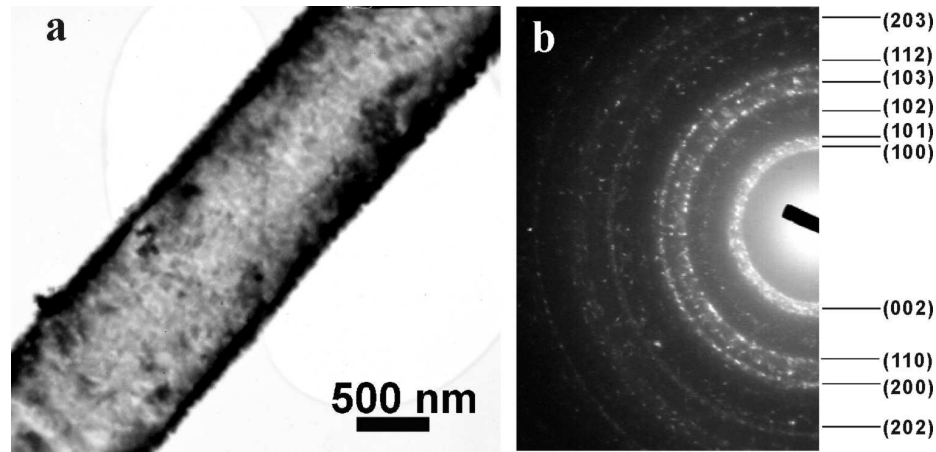

Figure 5.8: (a) TEM image of a CdSe microtube segment. (b) Corresponding SAED of (a), strong lattices are indexed.

In this section, CdSe nanowires and microtubes prepared by templated high-temperatures thermolysis of a typical arylchalcogenolates precursor, $Cd(SePh)_2 \cdot$ TMEDA, was discussed. CdSe nanowires with tunable aspect ratio were obtained by wetting of ordered porous alumina. For an annealing temperature of 500°C and varying annealing times, CdSe nanostructures from nanoparticles over nanorods to high aspect ratio nanowires were accessible. A systematic study on crystallization and ripening of these nanosystems revealed that at first prolate particles of the target material form inside the pores. They grow to short rods and eventually to long rods having aspect ratios of several 100 to one under prolonged thermal treatment. The obtained nanowires display excellent uniformity in diameter. Different from other examples of CdSe nanowires obtained by template wetting, the nanowires have their c-axis largely oriented along the axis of the pores, not oriented randomly. CdSe microtubes with grainy walls were prepared by wetting of macroporous silicon.

5.3 Templates as reactants I: Sn, SnSe and SnO$_2$ microtubes, nanotubes and nanowires by conversion of Sn(SePh)$_4$

In this section, we will report on a new synthetic approach where the templates are not only inert shape-defining moulds but are chemically reactive in the oxidation or reduction of tin (II) selenide nanostructures.

5.3.1 Redox properties of templates

The pore walls of porous alumina membranes are amorphous and also contain tetrahedrally coordinated aluminum atoms, defects and electrolyte anions [125]. The properties of the pore walls depend to a great extent on the electrolyte. The more acidic medium of sulfuric acid together with a higher defect concentration in thin pore walls. This may to enhance the reactivity of the templates with small pore diameters (Table 2). Owing to the large surface area of the pore walls and a relevant number of defects, electrolyte anions and distortions forming in the structure of the pore walls, macroporous silicon templates pores have effective reducing properties during annealing [126]. High temperature chemical transformations exploiting the oxidizing power of alumina and reducing power of the Si templates further extend the range of accessible target materials the 1D nanostructures and microstructures may consist of. For the preparation of nanowires and nanotubes of SnSe, Sn and SnO$_2$ we used different types of templates listed in Table 2. The intermediate oxidation state of Sn(II) in SnSe offers the opportunity of either a reduction or an oxidation of the SnSe nanostructures by appropriate pore walls with reducing or oxidizing properties. Such a selective redox chemistry within the pores requires a sufficient oxidizing power of the pore walls of the used alumina templates and a good reducing ability of the pores of macroporous silicon, as these two template materials are the readily accessible ones with complementary redox properties.

To model the reduction chemistry of Sn(SePh)$_4$ and SnSe with macroporous silicon and with the pore walls of porous alumina, the two tin compounds were reacted with commercial silicon powder under different conditions (Table (3)) and the molecular precursor Sn(SePh)$_4$ was heated in boiling wet diethylene glycol solvent, a system with hydroxyl groups and a small water content just like the amorphous wall structure of the pores in ordered alumina membranes [125] [127]. Under these conditions Sn(SePh)$_4$ did not thermolyze into SnSe but was converted into nanoparticles of SnO$_2$ with a diameter of about 10 nm, as could be shown by X-ray powder diffraction. In a

Table 2: Redox properties of different template types at elevated temperatures.

template type	pore diameter	redox properties
alumina (grown in sulfuric acid)	25 nm, 35 nm	oxidation
alumina(grown in phosphoric acid)	180 nm, 400 nm	mostly inert
silicon	1 μm	reduction

series of experiments with silicon powder the formation of elemental tin was observed at reaction temperatures higher than 600°C (Table (3)).

Table 3: Reactions of Sn(SePh)$_4$ and SnSe with silicon (reaction time: 15h).

tin compound	silicon source	reaction temperature	product
Sn(SePh)$_4$	Si template	650°C	Sn
Sn(SePh)$_4$	Si powder	500°C or 600°C	SnSe
Sn(SePh)$_4$	Si powder	650°C	Sn
SnSe(nanopart.)	Si powder	650°C	Sn
SnSe(microcryst.)	Si powder	650°C	SnSe, very little Sn

For a given template system, the reduction or oxidation can easily be initiated by increasing the temperature to $\sim$ 650°C. Starting from tin(II) selenide nanotubes with tin in a medium oxidation state, single-crystalline nanotubes of elemental tin were produced in a high temperature reaction with the macroporous silicon template as a reducing environment. In an analogous manner single-crystalline nanowires of tin (IV) oxide SnO$_2$ were obtained using the high temperature oxidizing properties of the pore walls of alumina templates etched with sulfuric acid.
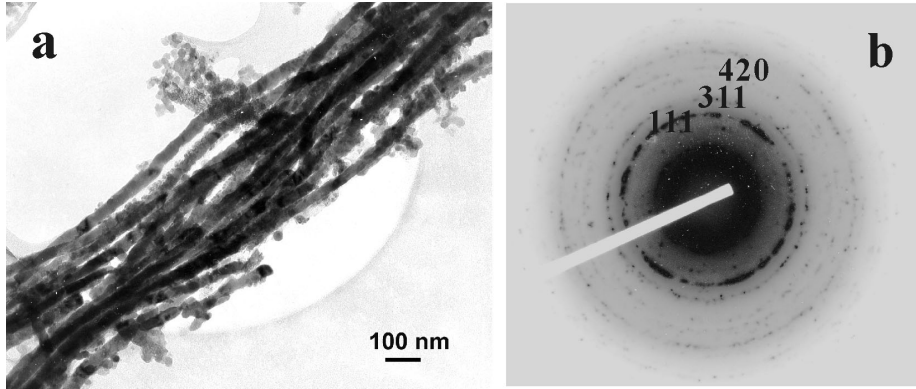
Figure 5.9: (a) TEM image of a bundle of released SnSe nanowires with a diameter of 25 nm; (b) Electron diffraction pattern of a bundle of SnSe nanowires.

5.3.2 SnSe nanowires

SnSe is a narrow band gap semiconductor with an optical band gap of ~ 1 eV. Nanoscale thin films of the tin (II) chalcogenides SnS and SnSe are promising materials for photoelectric conversion[128] [129]. Polycrystalline films of SnSe can be used in energy conversion devices [130] [129]and memory switching [131]. All products resulting from a thermolysis of $Sn(SePh)_4$ [105] at 350°C showed a granular, polycrystalline morphology. In the wetting procedure applied here, the single-source precursor $Sn(SePh)_4$ is infiltrated into the pores. In a low temperature thermolysis of about 350°C SnSe forms as the initial thermolytic product and no chemical reaction involving the template and the precursor or the template and the produced SnSe takes place. Nanowires consisting of orthorhombic SnSe (space group Pbnm) with a diameter of 25 nm, corresponding to the diameter of the template pores, were obtained by annealing the wetted samples at 350°C for 36 h. A TEM image of a bundle of released polycrystalline SnSe nanowires is shown in Figure 5.9a and the corresponding electron diffraction pattern is shown in Figure 5.9b. An X-ray diffraction pattern of the SnSe nanowires which indicates the formation of single-phase SnSe is represented in Figure 5.10.

5.3.3 SnSe nanotubes and microtubes

Unlike solid wires formed in narrow pores with diameters of 25 nm, nanotubes and microtubes of SnSe with polycrystalline walls were obtained when pore diameters of 180, 400 or 1000 nm templates were used. The SEM images in Figure 5.11a and b show an overview and a magnified image of an array of aligned SnSe nanotubes released from the template. In Figure 5.11b it can be seen that the nanotubes exhibit
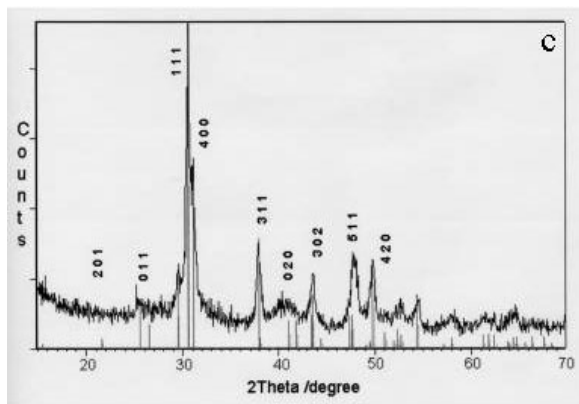
Figure 5.10: XRD pattern of SnSe nanowires in the template (reflections are calculated as a line pattern and indexed according to JCPDS No. 88-0287).

terminating caps at their ends, resulting from the bottom dimple of the template pores. This detail nicely shows that the pores were filled in their full depth and that the excellent aspect ratio of the pores can be transferred quantitatively to the one-dimensional nanostructures.
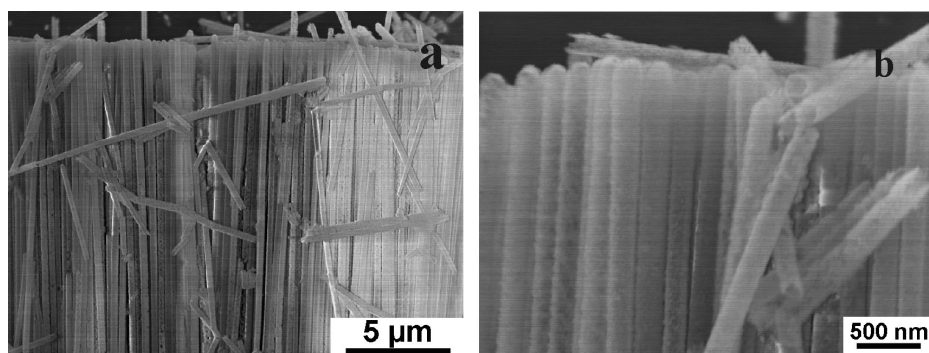

Figure 5.11: SEM images of an ordered array of SnSe nanotubes with a diameter of 180 nm: (a) Overview and (b) detail showing granular wall morphology and terminating caps.

The grain structure of the tube walls becomes obvious from Figure 5.12a, where a TEM images of an individual polycrystalline SnSe tube released from a template with a pore diameter of 400 nm is depicted. The crystallites have diameters of the order of 10 - 20 nm. The thickness of the tube walls is also in the range of 20 nm. The SAED pattern depicted in Figure 5.12b shows the characteristics of polycrystalline tubes of single-phase orthorhombic SnSe (space group Pbnm).

5.3.4 Sn microtubes

Ordered structures of tin nanotubes can be used for the preparation of nanostructures of catalytically active binary intermetallics such as Pt-Sn [132] or Au-Sn [133]. Tin
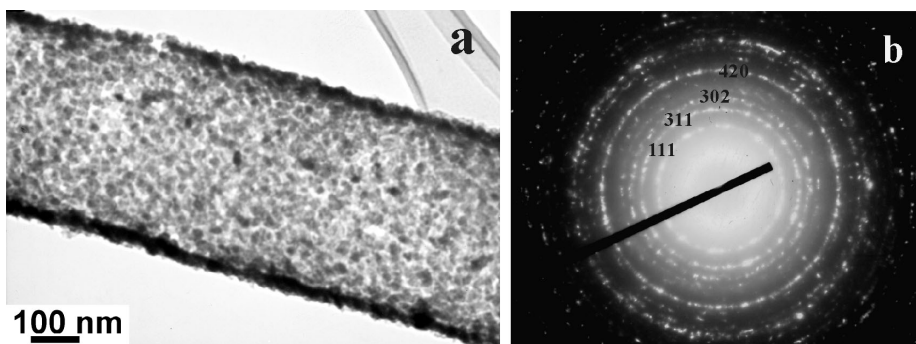
Figure 5.12: (a) TEM image of a single SnSe nanotube with a diameter of 400 nm with polycrystalline walls. (b) Electron diffraction pattern of the tube section seen in(a).

nanowires were also shown to exhibit superconducting properties [134]. Here, Sn microtubes were prepared by a redox reaction of $Sn(SePh)_4$ and SnSe with macroporous silicon (Table (3))
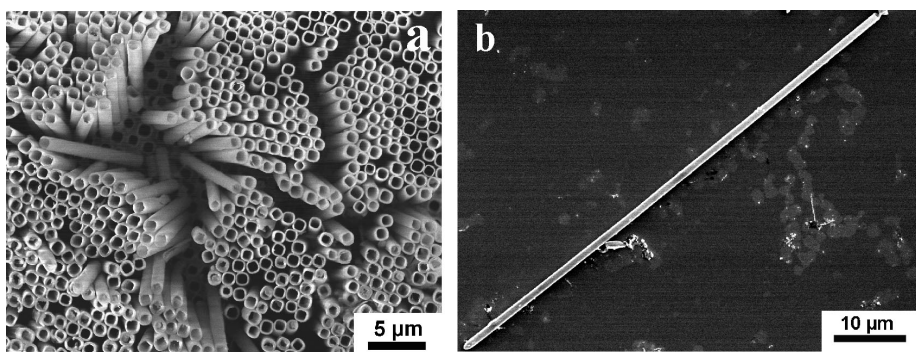

Figure 5.13: (a) SEM image of a laterally extended array of Sn microtubes with a diameter of 1 μm, protruding from the macroporous silicon matrix. (b) An completely liberated Sn tube on a silicon wafer, with an aspect ratio of 90 : 1.

The reduction can be performed as a quantitative conversion either starting directly from molecular $Sn(SePh)_4$ or from independently produced nanoparticles of SnSe with a particle size of $\sim$ 50 nm. In both reactions elemental tin was formed under the reaction conditions and crystallized from its liquid state under cooling. Owing to the large surface area of the pore walls of macroporous silicon templates and a relevant number of defects and distortions forming in the structure of the pore walls of macroporous silicon during annealing [135], the reaction of $Sn(SePh)_4$ with the template pores should be even more effective than its reaction with microcrystalline silicon powder. Accordingly, single-crystalline microtubes consisting of elemental Sn with a diameter of 1 μm were obtained by infiltrating macroporous silicon moulds

with $Sn(SePh)_4$, annealing of the wetted templates at temperatures in the range of 600°C to 650°C for 5h and subsequent cooling to room temperature at a rate of 2 K/min. Figure 5.13 shows an array of aligned Sn tubes protruding from a partially removed template. They are uniform in size and have a wall thickness of 150 nm.
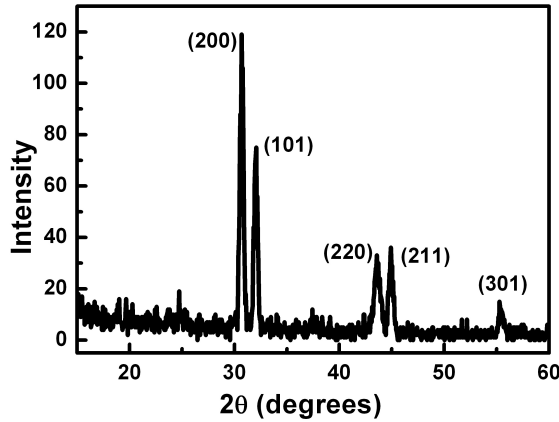

Figure 5.14: XRD pattern of aligned, partially released tin tubes. (All reflections are indexed on the basis of JCPDS No. 04-673).

All reflections in the X-ray diffraction pattern of aligned Sn tubes partially embedded in macroporous silicon (Fig. 5.14) can be indexed for tetragonal β-Sn (JCPDS entry No. 04-673) without ambiguity, indicating that the reduction of tin (II) selenide is quantitative. Figure 5.15a shows an individual tin tube (d = 1 μm) after removal of the silicon template and an indexed SAED pattern is depicted in Figure 5.15b. The long axis of the Sn microtube growth along the (30-1).
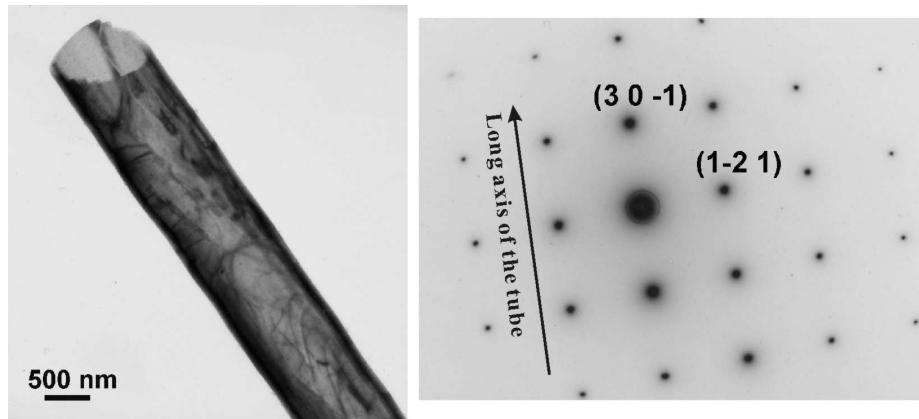

Figure 5.15: (a) Tin microtube after removal of the silicon template. (b) Indexed SAED pattern of a single tin microtube (zone axis [123]), indicating its single-crystalline character.

5.3.5 SnO$_2$ nanowires

When Sn(SePh)$_4$ was infiltrated into porous alumina and annealed at 650°C a big difference in the oxidizing power of the walls of small pores etched with sulfuric acid and the walls of larger pores etched with phosphoric acid became apparent. Whereas the thicker, less acidic walls of the larger pores did not lead to oxidation of SnSe, single-crystalline SnO$_2$ nanowires with high aspect ratio and a diameter of 25 nm were prepared employing porous alumina templates etched with sulfuric acid. This is in accordance with the higher defect concentration, the increased acidity and the presence of electrolyte anions and residual water in the pore walls of templates etched with sulfuric acid [56]. Figure 5.16a shows a TEM image of SnO$_2$ nanowires at low magnification. They typically have aspect ratios larger than 100:1. The non-uniform contrast appearance of these nanowires is due to bending contours, thickness fringes and planar defects [136]. An indexed SAED pattern of part of a section of a single crystalline SnO$_2$ nanowire is depicted in Figure 5.16 showing the single crystalline nature of the wire.
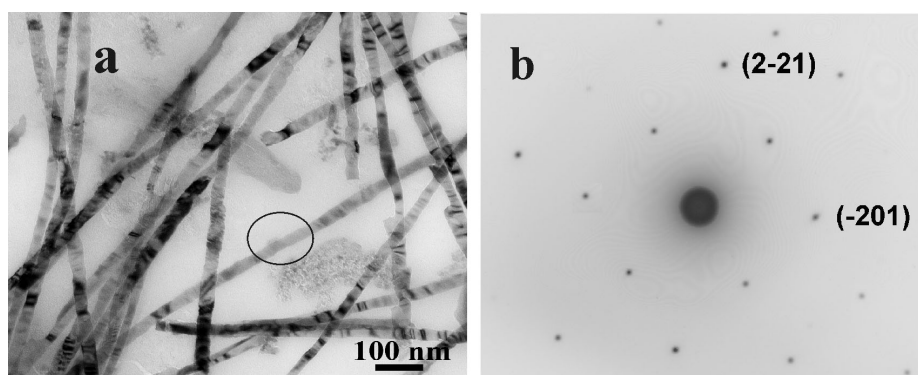

Figure 5.16: (a) TEM image of single-crystalline SnO$_2$ nanowires with a diameter of 25 nm. (b) Indexed SAED pattern (zone axis [122], growth axis (-210)) of the marked section of the SnO$_2$ nanowire seen in (a).

A high resolution TEM micrograph of a selected area of an individual nanowire of tetragonal SnO$_2$ (Fig. 5.17) again shows the single-crystalline nature of the wires. The interplanar spacing of d = 3.34 Å(Fig. 5.17c) could be assigned to 110 planes of the SnO$_2$ lattice described in space group P42/mnm (JCPDS No. 21-1250).

In this section, SnSe, SnO$_2$ and Sn were obtained from one single-source precursor Sn(SePh)$_4$. We demonstrated that the selective reactivity of the pore walls of porous alumina and macroporous silicon leads to a complete conversion of the nano-objects into different target materials.
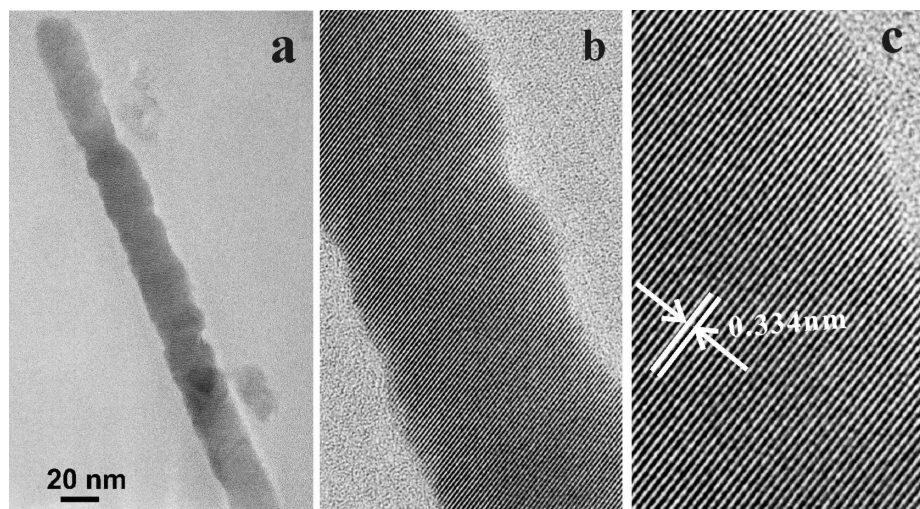
Figure 5.17: (a) Segment of an individual SnO$_2$ nanowire with a diameter of 25 nm. (b) Enlarged section of the nanowire, indicating the good homogeneity and crystallinity. (c) High resolution image of a part of (b), showing 110 lattice fringes of SnO$_2$.

5.4 Templates as reactants II: synthesis of nanostructures of ZnTe, Te, ZnAl$_2$O$_4$ and ZnAl$_2$O$_4$-Te from Zn(TePh)$_2$·TMEDA

Another case of templates serving as reactants is the templated high temperature thermolysis of the organochalcogenolate precursor of Zn(TePh)$_2$·TMEDA [100]. Dependent on the experimental conditions applied, Zn(TePh)$_2$·TMEDA in the pores of ordered porous alumina membranes yields single-crystalline nanowires of zinc telluride (ZnTe), zinc spinel/tellurium (ZnAl$_2$O$_4$-Te) and elemental tellurium or ZnAl$_2$O$_4$ nanotubes. ZnTe is one of the most important II-VI type compound semiconductors, a class of materials that is of considerable interest for potential applications in the fields of sensor technology [137] and light emitting diodes [138]. ZnTe exhibits a direct optical bandgap of 2.26-2.29 eV at room temperature and of 2.39 eV at 1.6 K [139] [140]. Te is a narrow bandgap (0.35 eV) semiconductor with a highly anisotropic crystal structure [141]. Trigonal elemental tellurium crystallizes in a non-centrosymmetric space group and shows several interesting properties, for instance, photoconductivity [142] [143], thermoelectricity [144], and piezoelectricity [145]. The zinc aluminum oxide spinel ZnAl$_2$O$_4$ is widely used as a catalyst for cracking, dehydration, hydrogenation and dehydrogenation [146] [100].
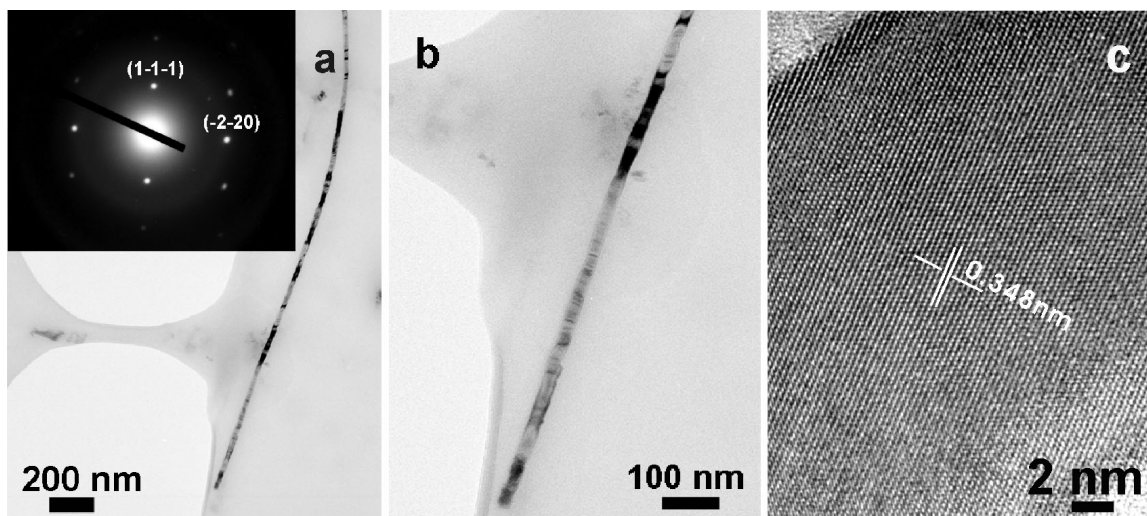
Figure 5.18: (a) TEM image and SAED pattern (inset, zone axis [1 -1 2]) of a single-crystalline ZnTe nanowire. (b) Bottom part of the wire at higher magnification. (c) HRTEM image of a ZnTe nanowire showing (111) lattice planes (d = 3.48$\mathring{A}$).

5.4.1 ZnTe nanowires

In a general synthetic procedure for the preparation of the nanostructures a solution of 5 wt-% Zn(TePh)$_2$·TMEDA [100] in chloroform (CHCl$_3$) was dropped onto ordered porous alumina with a pore diameter of 25 nm under ambient conditions. After the solvent had evaporated, the templates with the precursor inside the pores were heated to 280°C and kept at this temperature for 2h. Then, the samples were heated to 500°C, annealed at this temperature for 24h or 48h, and slowly cooled to room temperature. If as-wetted samples were annealed in vacuum for 48 h at 500°C, ZnTe nanowires were obtained, which could be released by etching the templates with aqueous KOH.

Figure 5.18a shows a representative TEM image of a ZnTe nanowire with a diameter of 25 nm corresponding to the one of the template pores and an aspect ratio of 120, and Figure 5.18b a detail at higher magnification. The SAED pattern (Fig. 5.18a, inset) of a segment of the ZnTe nanowire evidences the single-crystalline nature as it contains only indexed Bragg reflections. Growth direction of the ZnTe nanowire is (1-1-1). The HRTEM image of a ZnTe nanowire (Fig. 5.18c) shows the (111) lattice planes (d = 3.48$\mathring{A}$) of cubic ZnTe (space group F-43m) (JCPDS No. 15-147).

A overview of ZnTe nanowires at low magnification and its corresponding SAED are described in Figure 5.19. The indexed Bragg reflections of the SAED (Fig. 5.19b) further confirmed that cubic ZnTe nanowires were obtained. We assume that the formation of the ZnTe nanowires occurs according to the well-known degradation
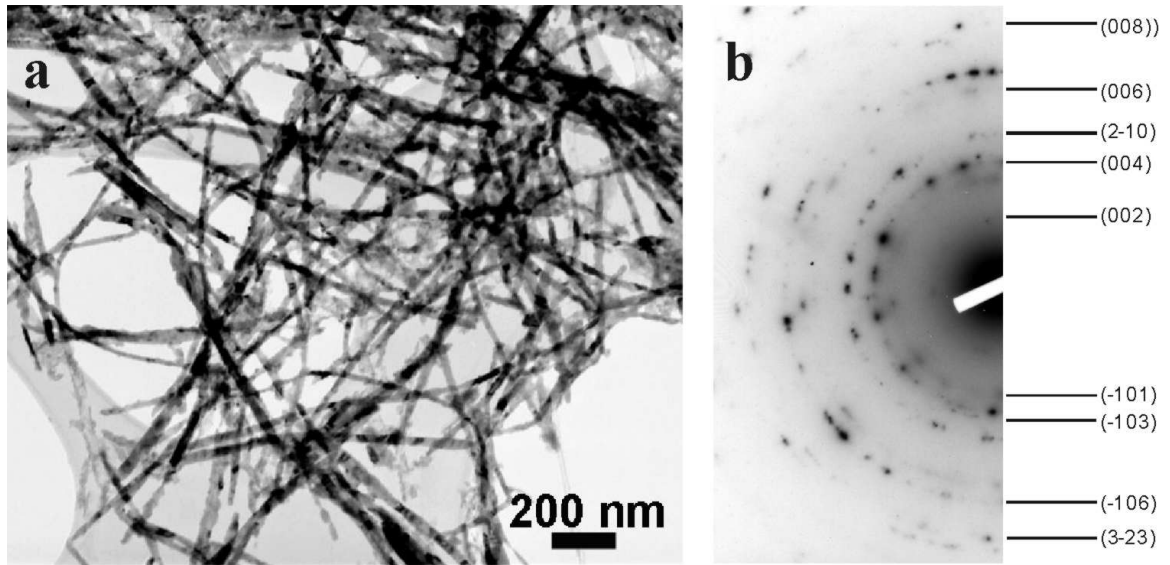
Figure 5.19: (a) TEM image of ZnTe nanowires and (b) SAED pattern (strong reflections are indexed).

mechanism of $Zn(TePh)_2 \cdot TMEDA$ [100] [101] [104] [147] [105]. A room temperature photoluminescence spectrum of released ZnTe nanowires on a silicon wafer is shown in Figure 5.20. The PL spectrum centered at 545 nm (bandgap of 2.26-2.29 eV) and had a full width at half maximum (FWHM) of about 40 nm. ZnTe nanowires with a diameter of 25 nm exhibit the characteristic photoluminescence of the corresponding bulk ZnTe [124].
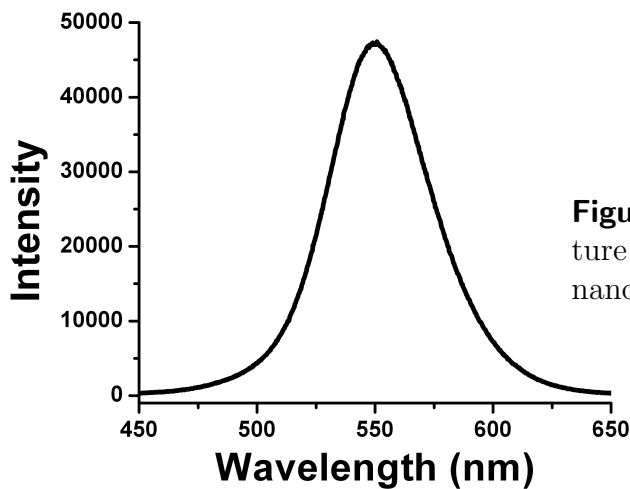
Figure 5.20: Room temperature PL of single-crystalline ZnTe nanowires (d = 25 nm).

5.4.2 ZnAl₂O₄-Te nanowires

If the wetted samples were not annealed in vacuum but in air for 24 h at 500°C, single-crystalline tellurium nanowires (D_p = 25 nm) surrounded by a polycrystalline $ZnAl_2O_4$ shell (wall thickness = 8 nm) were obtained. The core/shell structure of as-prepared $ZnAl_2O_4$-Te nanowires is obvious from Figure 5.21. The $ZnAl_2O_4$-Te nanowires have an aspect ratio of about 200. The core/shell structure has a diameter of 35 - 40 nm, which is larger than the one of the template pores. This larger diameter strongly supports the idea that the pore walls act as chemical reactants in the formation of the core/shell wires. The single-crystalline tellurium core can be seen in the high-resolution TEM image (Fig. 5.21). The distance between the lattice planes of the tellurium core was found as 3.1$\mathring{A}$, corresponding to the d-value of the (101) lattice planes. Overview TEM images of core-shell $ZnAl_2O_4$/Te nanowires at low magnification and its SAED pattern are shown in Figure 5.22. The SAED pattern (Fig. 5.22b) shows reflections of both tellurium and zinc spinel. The strong reflections are indexed.
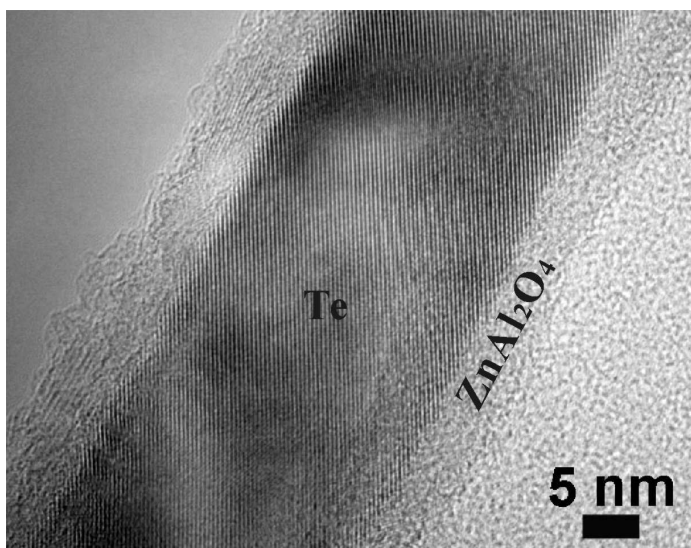
Figure 5.21: HRTEM image of a $ZnAl_2O_4$/Te core-shell structure. The lattice fringes of the tellurium core correspond to the (101) planes (d = 3.1 $\mathring{A}$).

The chemical composition of released core/shell nanowires was analyzed by energy-dispersive X-ray spectroscopy (EDX) (Fig. 5.23). Exclusively strong tellurium peaks and a weak oxygen peak are found in the spectrum measured on a wire segment where the $ZnAl_2O_4$ shell had peeled off (the copper peak originates from the TEM grid onto which the wires had been deposited) (Fig. 5.23a). This indicates that the core consists of pure tellurium, possibly covered by a thin oxide layer. A segment
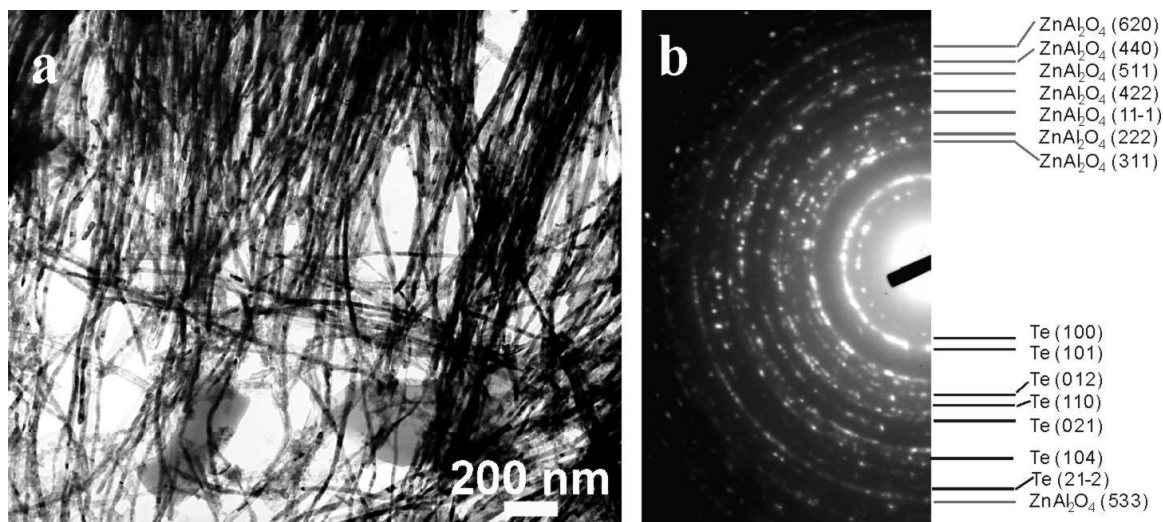
**Figure 5.22:** (a) TEM image of ZnAl$_2$O$_4$-Te nanowires and (b) its SAED pattern (strong reflections are indexed).

consisting only of the ZnAl$_2$O$_4$ shell was selected for a second EDX scan (Fig. 5.23b). The signals of aluminum, zinc and oxygen can be seen in the spectrum, whereas no tellurium could be detected. The atomic ratio of Zn: Al: O = 1 : 1.9 : 3.7 deduced from the EDX spectrum is in accordance with the stoichiometry of ZnAl$_2$O$_4$. A third EDX spectrum was measured on an intact core/shell segment (Fig. 5.23c). Here, the peaks of zinc, aluminum, oxygen and tellurium can be seen. All EDX spectra indicate that the nanowires consist of a ZnAl$_2$O$_4$ shell with a tellurium core.

We suggest the following mechanism for the formation of the ZnAl$_2$O$_4$-Te core/shell nanowires. After thermolysis of Zn(TePh)$_2$·TMEDA, the initially formed ZnTe is transformed by ambient oxygen, resulting in the formation of ZnO and elemental tellurium within the pores.

$$2Zn^{2+} + 2Te^{2-} + O_2 \longrightarrow 2ZnO + 2Te \tag{5}$$
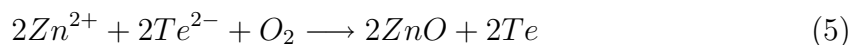
Freshly formed active ZnO reacts with the alumina template, as previously reported by Wang and Wu [148], to form the polycrystalline ZnAl$_2$O$_4$ shell. The formation of the compact and single-crystalline tellurium core is greatly facilitated by the fact that elemental tellurium with a melting point of 452°C [149] is formed in its liquid state at the annealing temperature of 500°C. A slow cooling process following the annealing step leads to the formation of single-crystalline tellurium structures inside the spinel shell.
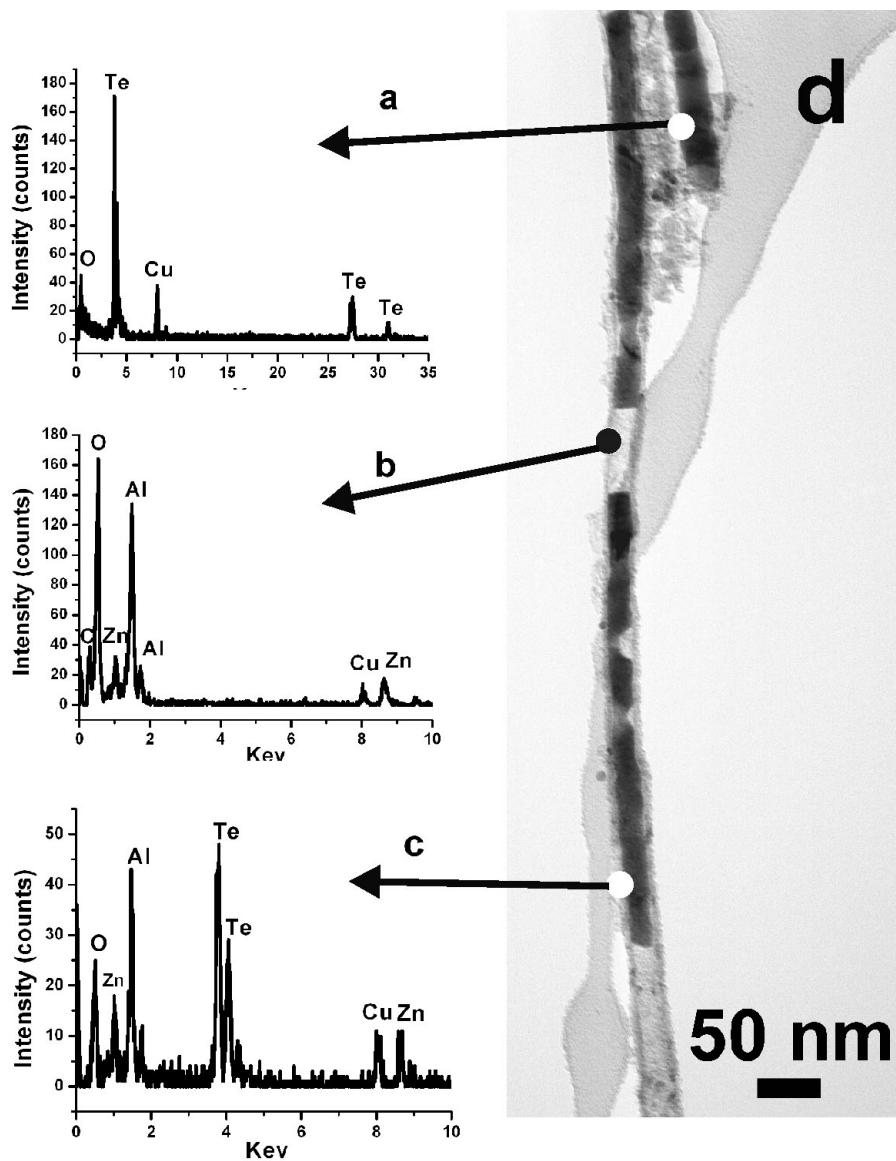
Figure 5.23: Chemical composition analysis of $ZnAl_2O_4$-Te nanowires by EDX spectroscopy: (a) EDX point spectrum of a pure tellurium nanowire measured at the location indicated in (d). (b) EDX point spectrum of a pure $ZnAl_2O_4$ shell measured at the location indicated in (d). (c) EDX point spectrum of a $ZnAl_2O_4$-Te core/shell structure measured at the location indicated in (d). (d) TEM image of the investigated nanowire segments.
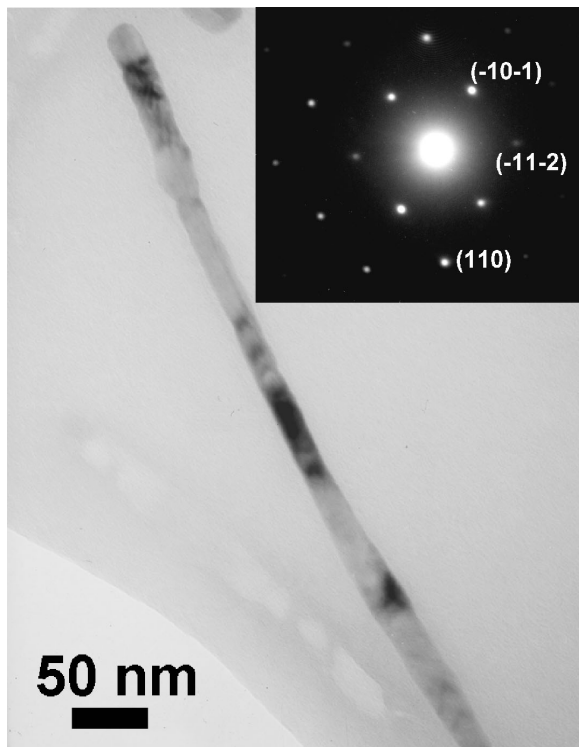
Figure 5.24: Released single-crystalline tellurium nanowire (d = 25 nm) and its indexed SAED pattern (inset, zone axis [-1 1 3]).

5.4.3 Te nanowires

Sonification of the core/shell structures resulted in the removal of the $ZnAl_2O_4$ crystallites, and liberated single-crystalline tellurium nanowires can be obtained (Fig. 5.24). The SAED patterns of these samples (Fig. 5.24, inset) show only Bragg reflections that can be assigned to trigonal tellurium (space group $P3_12_1$) (JCPDS No. 5-669). This gives evidence of the single-crystalline nature of the tellurium wires and the lack of relevant structural disorder in these products. An overview of Te nanowires at low magnification is shown in Figure 5.25a. A careful examination of the TEM image of the Te nanowires reveals that broken $ZnAl_2O_4$ nanotubes occasionally show up together with the Te nanowires. When we liberated Te nanowires from the core-shell $ZnAl_2O_4$-Te nanowires by sonification, even though in most of the case, the nanotubes are broken into very small pieces, they still exist in the suspension, and may thus be present in the TEM images. Moreover, there are occasional cases that long segments of the $ZnAl_2O_4$ nanotubes survive from being broken after the Te core get out of them. In this case, we may see the Te nanowires (majority) and $ZnAl_2O_4$ nanotubes (minority) show up in the same image. Figure 5.25 is such a kind of image. As expected, in the corresponding SAED pattern (Fig. 5.25b), not only the Bragg reflections of Te are indexed, a $ZnAl_2O_4$ reflection also can be assigned.
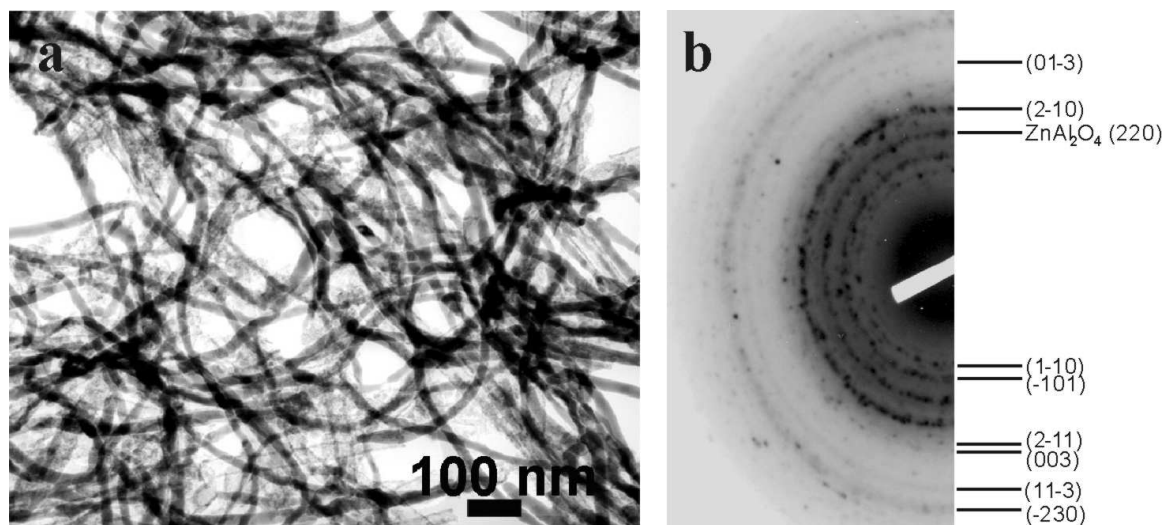
Figure 5.25: (a) TEM image of Te nanowires and (b) its SAED pattern (strong reflections are indexed).

5.4.4 ZnAl$_2$O$_4$ nanotubes

Not only the core without the shell, but also the shell without the core could be isolated by etching of the tellurium core with aqueous KOH at 90°C for 4 hours. A TEM image of as-obtained isolated nanoshells is seen in Figure 5.26a. The corresponding SAED pattern is shown in Figure 5.26b, the d-spacings of containing ring patterns are 2.8 Å), 2.44 Å), 2.02 Å), 1.56 Å), and 1.43 Å) corresponding to the (220), (311), (400), (511), and (440) reflections of ZnAl$_2$O$_4$ (spinel, space group Fd3m) indicating that the nanoshell consists of polycrystalline ZnAl$_2$O$_4$.
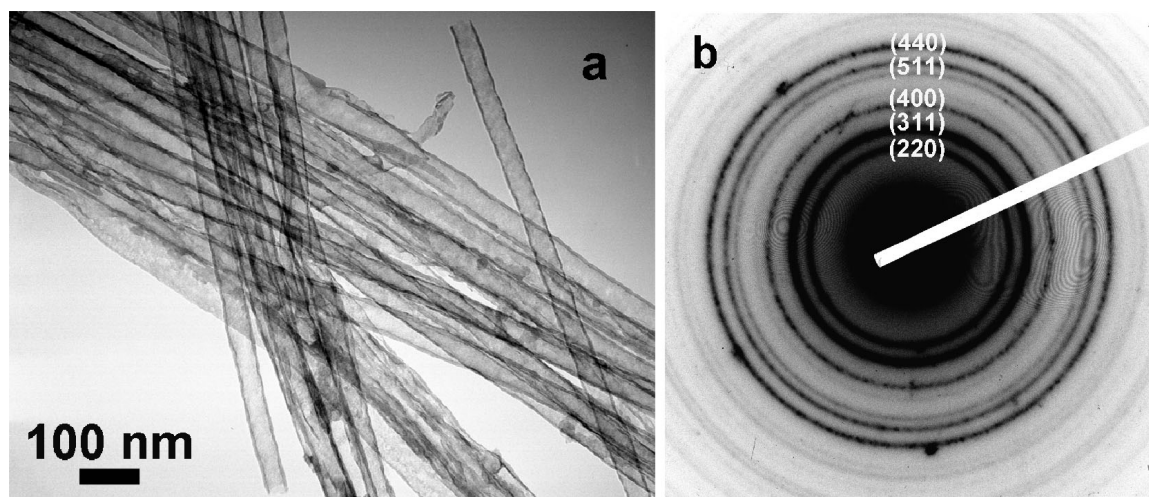
Figure 5.26: (a) TEM image of ZnAl$_2$O$_4$ shells and (b) its SAED pattern showing their polycrystallinity.

Typical HRTEM images of the highly crystalline wall of $ZnAl_2O_4$ nanotubes are displayed in Figure 5.27. A wall segment with d-spacings of 2.8 Å) and 2.3 Å), indicating (220) and (222) lattice planes, is seen in Figure 5.27a, and a detail at higher magnification in Figure 5.27b. Crystallites with different orientations are tightly fused together to form a tube wall without amorphous regions (Fig. 5.27c). The tubular nature of the nanostructures can be seen from the cross section of an individual tube (Fig. 5.27d). In order to investigate whether or not $ZnAl_2O_4$ nanotubes also form in the absence of tellurium, we infiltrated alumina templates with a dilute solution of 5wt-% $ZnCl_2$ in THF and applied the same protocol as in case of the thermolysis of $Zn(TePh)_2$·TMEDA. However, no $ZnAl_2O_4$ nanotubes were obtained, indicating that the slower formation of ZnO from the tellurolate precursor is crucial.
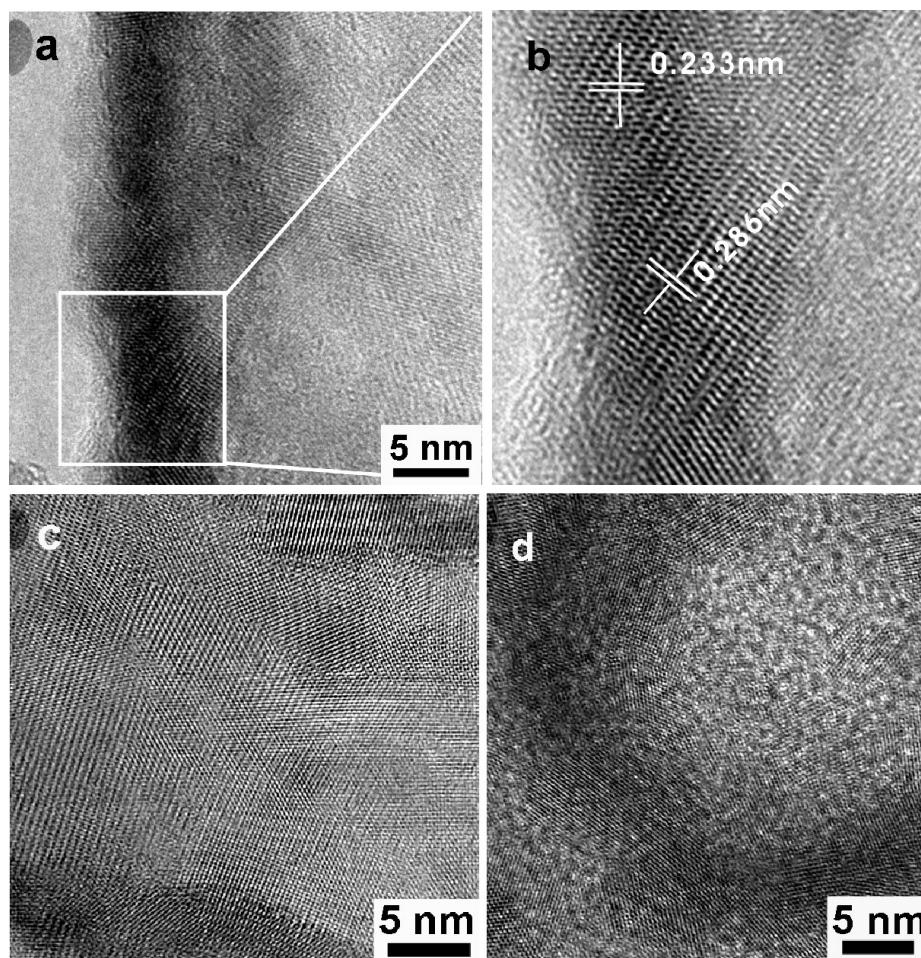
Figure 5.27: HRTEM images of $ZnAl_2O_4$ nanotubes. (a) Wall segment and (b) detail at higher magnification. (c) Typical polycrystalline morphology of the tube walls. (d) Cross section of a tube (the dark regions with higher mass thickness contrast represent the tube wall).

We have shown in this section another example of templates serving as reactants. By proper variation of the conditions under which the thermolysis of $Zn(TePh)_2 \cdot$ TMEDA takes place single-crystalline nanowires of ZnTe or Te in a $ZnAl_2O_4$ nanoshell can be produced. Alternatively, pure nanotubes of $ZnAl_2O_4$ can also been prepared after removal of the tellurium core.

5.5   *Summary of the chapter*

In this chapter, we have shown that templated high-temperature thermolysis of single-source precursors of the arylchalcogenolate type is a versatile method to prepare nanowires, nanotubes and microtubes of a range from target materials, which is not limited to compound semiconductors. In the process of synthesis of CdSe nanowires and microtubes by templated high-temperature thermolysis of $Cd(SePh)_2 \cdot$TMEDA, porous membranes serve as inert mold to modify the morphology of the target materials. In contrast, taking the templated high-temperature conversion precursors of $Sn(sePh)_4$ and $Zn(TePh)_2 \cdot$TMEDA as examples, we proved that the selective reactivity of the pore walls of porous alumina and macroporous silicon leads not only just to a surface modification but to a complete conversion of the one-dimensional nano-objects. This allows the preparation of monodisperse tubes and wires of different target materials.

CHAPTER VI

Modification of Macroporous Silicon by Templated Thermal Conversions

As we introduced in chapter 3, the pores of macroporous silicon are arranged in either a hexagonal or quadratic lattice characterised by a sharp pore diameter distribution, forming a monodomain that may extend several cm^2. Specific defect structures such as linear and bent waveguides, Y-branches and microresonators can be implemented into this two-dimensional (2D) photonic bandgap material [150]. Macroporous silicon has been employed as a template for the fabrication of tubular structures [13] [23] [25]. Modification of macroporous silicon by functional oxide microtubes will result in hybrid systems consisting of billions of aligned functionalized channels, which have a great potential for the design of micrometer-scale, functional optical components in micro-devices. Conventional approaches to move functional materials into the pores are mainly based on the conversion of precursors [76] [78] [126], and the tubes thus obtained are grainy and of poor mechanical stability. Moreover, the controlled incorporation of dopants, and the control over the stoichiometry of the wall material is difficult to achieve. To overcome these drawbacks, we introduced a so called high temperature melt wetting approach. This is a modified templated high-temperature conversion approach that involves infiltration of the porous template directly with the melt of the target material. As an example, we infiltrated macroporous silicon with a congruent $LiNbO_3$ melt containing 0.3 mol% Er, as discussed in section 6.1. An interesting phenomena appeared in the fabrication of $LiNbO_3$ and $Er:LiNbO_3$ microtubes. There are crystalline reflections of SiO_2 in the XRD patterns besides those of $LiNbO_3$. We assume the crystallization of amorphous SiO_2 covering the pore walls is induced by trace amount of lithium, which volatilized from the $LiNbO_3$ melt at elevated temperature during the annealing process. Thus, another way to modify macroporous silicon by microtubes is proposed: preparation of crystalline SiO_2 microtubes in the macroprous silicon by offering lithium to induce crystallization of amorphous SiO_2.

6.1 LiNbO$_3$ and Er:LiNbO$_3$ microtubes by high temperature melt wetting

Doping host systems with rare earth elements yields functional materials with superior optical properties. Trivalent erbium, Er^{3+}, is of particular interest, because the sharp optical intra-4f transitions from the first excited state ^{4}I$_{13/2}$ to the ground state ^{4}I$_{15/2}$ at 1.53 μm coincide with the transmittance maximum of silica-based fibers [151] [152]. However, the integration of such dopant/host systems into device architectures has remained an problem. Only few examples for Er^{3+}-doped 1D nanostructures and microstructures have been reported to date: for example, as-grown silicon [153] and germanium [154] nanowires were exposed to a volatile erbium compound. The challenge remains to control the doping level, and to integrate Er^{3+}-doped 1D building blocks into functional device architectures based on Si microstructures, such as macroporous Si. In our experiments, Er^{3+}-doped LiNbO$_3$ microtubes were fabricated by infiltrating of macroporous silicon with a congruent LiNbO$_3$ melt containing 0.3 mol% Er.

6.1.1 Fabrication of LiNbO$_3$ and Er:LiNbO$_3$ microtubes

To obtain the Er:LiNbO$_3$ microtubes, we infiltrated macroporous silicon with a congruent LiNbO$_3$ melt containing 0.3 mol% Er. At first, Er-doped LiNbO$_3$ single crystals were grown along the c-axis in air from the congruent melt by the conventional Czochralski method [155] and manually milled using an agate mortar. Subsequently, we covered macroporous Si (pore diameter 1 μm, pore depth 100 μm) with a thin layer of the powder thus obtained. The samples were annealed at 1260°C just above the melting point of single-crystalline LiNbO$_3$ for 2 hours, and cooled to 1050°C at a rate of 0.1°C/min. To eliminate residual internal stress and defects, this temperature was kept for 3 hours, before the samples were cooled to room temperature at a rate of 5°C/min. All steps were performed in air. No external driving force was applied to pull the melt into the pores. The residual material on the template surface was carefully removed by mechanical polishing. Optionally, the macroporous Si can be selectively etched with aqueous 30 wt-% KOH at elevated temperatures to release the Er:LiNbO$_3$ microtubes.

6.1.2 Morphology and structural characterization of LiNbO$_3$ and Er:LiNbO$_3$ microtubes

Figure 6.1a shows a SEM picture of the polished surface of macroporous Si containing Er:LiNbO$_3$ microtubes. Their walls appear in a brighter contrast than the surrounding Si matrix. An array of partially released, aligned Er:LiNbO$_3$ microtubes connected with macroporous Si acting as a support is seen in Figure 6.1b, and completely liberated Er:LiNbO$_3$ microtubes deposited on a Si wafer are shown in Figures 6.1c and 6.1d. Their walls are smooth and virtually free of defects. Their aspect ratio amounts to 100 corresponding to that of the template pores. Therefore, the Er:LiNbO$_3$ melt must form a uniform wetting layer completely covering the pore walls of the macroporous silicon template. Powders of released Er:LiNbO$_3$ microtubes contain no short tube fragments (Fig. 6.1c, 6.1d). This indicates that their considerable mechanical stability prevents the Er:LiNbO$_3$ microtubes from breaking in the course of the preparation procedure.
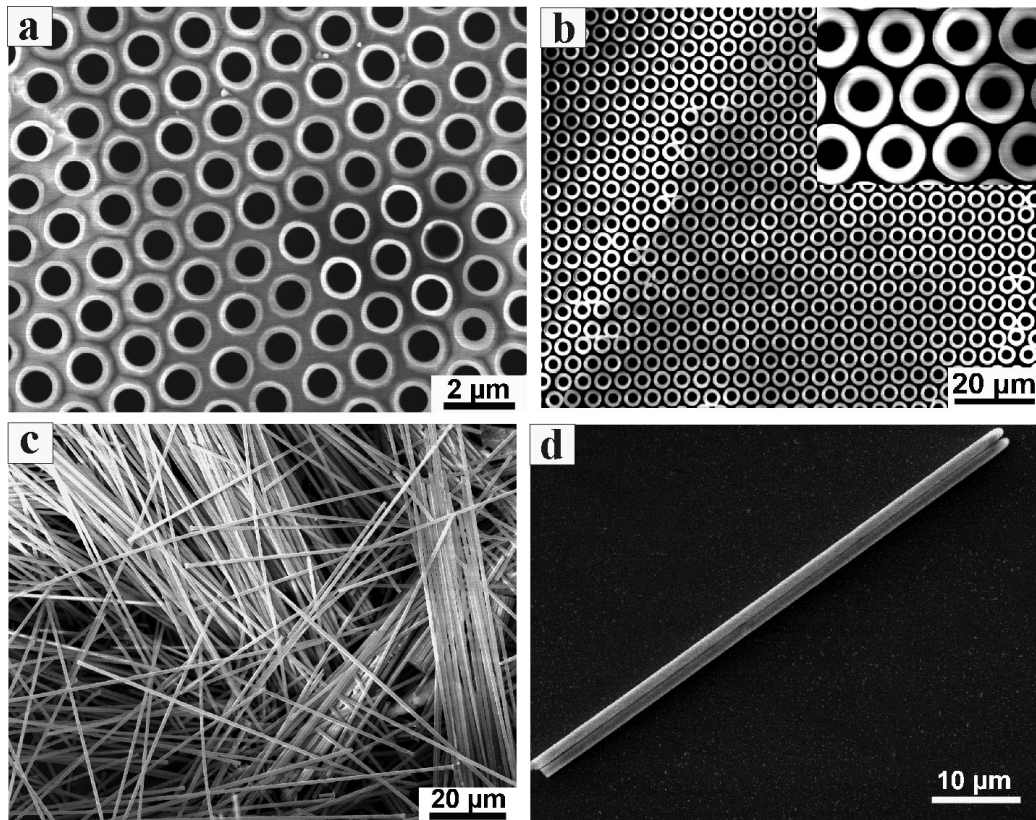

Figure 6.1: SEM images Er:LiNbO$_3$ microtubes. (a) Er:LiNbO$_3$ microtubes within macroporous Si after polishing the template surface. (b) Array of aligned Er:LiNbO$_3$ microtubes partially embedded in macroporous Si after partially etching the template. (c),(d) Completely liberated Er:LiNbO$_3$ microtubes deposited on a Si wafer.

A representative bright-field TEM image of an Er:LiNbO$_3$ microtube segment is shown in Figure 6.2a, and the corresponding selected area electron diffraction (SAED) pattern in Figure 6.2b. Only one set of spots is seen, evidencing the single-crystalline nature of the tube wall. At slow cooling rates as applied here, a small number of nuclei, formed at high nucleation temperatures, will initiate crystallization. Under these conditions, the growth of extended single-crystalline entities can be expected. However, twinned structures [156] may form, when the centrosymmetric high-temperature phase of LiNbO$_3$ is converted into the non-centrosymmetric low-temperature phase at the Curie point of 1160°C. Therefore, we assume that the Er:LiNbO$_3$ microtubes consist rather of single-crystalline segments than of one single crystalline entity. Figure 6.2c shows an ultra-thin slice with a thickness of a few tens of nm, as determined from its interference colour, containing a cross-section across a Er:LiNbO$_3$ microtube embedded in epoxy resin along its long axis. Figure 6.2d shows correspondingly a cross-section along a tube. The tube walls, which were partially damaged because of the mechanical stress imposed during the sample preparation, have a uniform thickness of about 100 nm. If the mechanical failure predominantly occurs at grain boundaries, the intact wall segments should correspond to single crystalline domains. We estimate their extension in the direction of the tubular long axis to be of the order of several hundreds of nm.

6.1.3   X-ray diffraction of LiNbO$_3$ and Er:LiNbO$_3$ microtubes

XRD scans of macroscopically aligned Er:LiNbO$_3$ microtubes located within the pores of polished macroporous Si were measured in the reflection mode (Fig. 6.3a). The sample surface was inclined by 5° with respect to the plane defined by the incident beam and the detector. The kinematically forbidden (200) reflection of the (100) oriented Si template at 32.8°, which occurs when macroporous Si is annealed in air, would otherwise coincide with the (104) peak of LiNbO$_3$ [126]. It is well known that thermal oxidation of macroporous Si imposes considerable mechanical stress on Si forming the pore walls [157]. Solely annealing macroporous silicon in argon/air environment does not result in the occurrence of lattice distortions abrogating the extinction of the (200) (Fig. 6.4a), whereas, a sharp Si (200) peak appears in the XRD pattern when the macroporous silicon is annealed in the presence of lithium (Fig. 6.4b). Hence, the Si lattice must have been distorted upon the formation of the crystalline LiNbO$_3$ tubular structures on the pore surface of macroporous silicon (Fig. 6.3). In Figure 6.3, the XRD pattern contains the characteristic reflections of LiNbO$_3$ (space group R3c, JCPDS entry 78-0250). The (210)/(011) double peak at
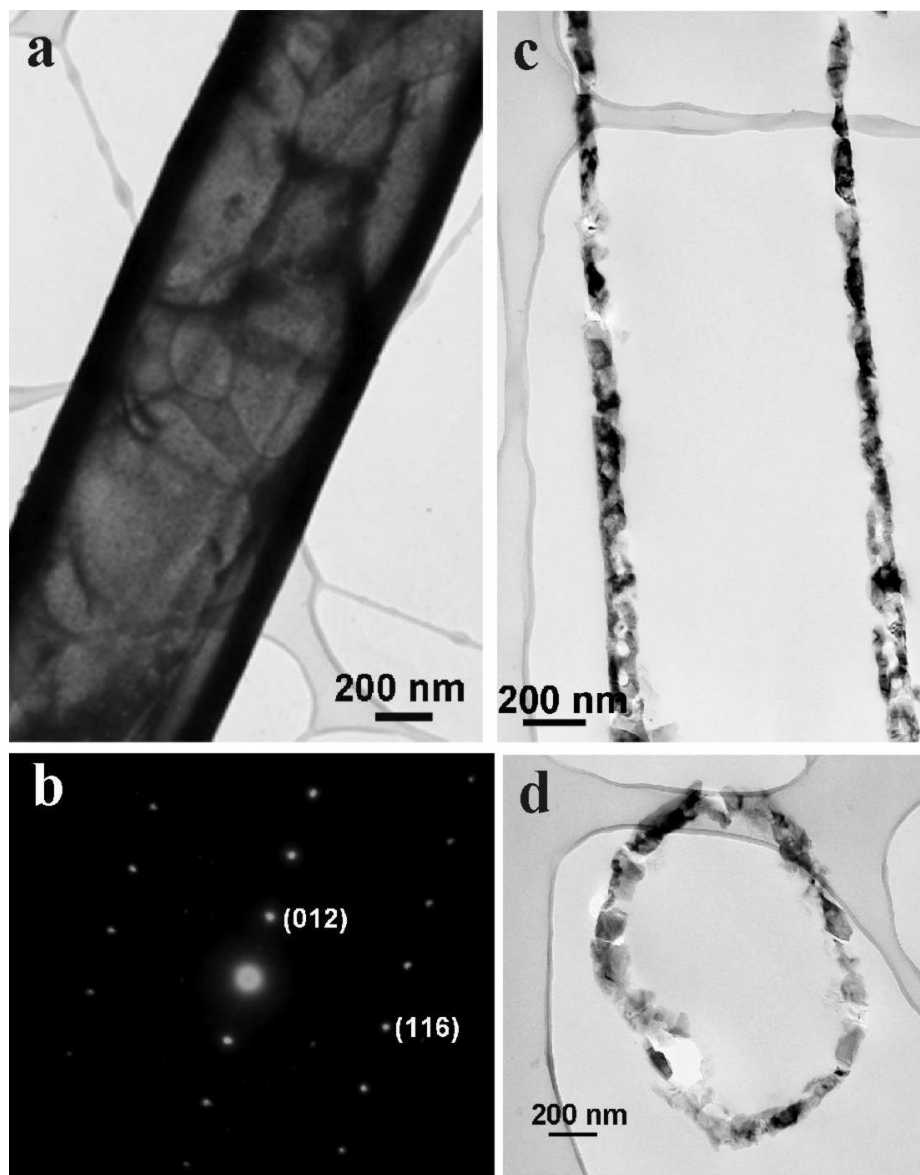
72

Figure 6.2: TEM images of Er:LiNbO$_3$ microtubes.(a) Single Er:LiNbO$_3$ microtube. (b) Corresponding SAED pattern. The (012) and (116) diffraction spots of rhombo-hedral LiNbO$_3$ are denoted, the growth direction of the tube is (012). (c) and (d) Ultra-thin section of a Er:LiNbO$_3$ microtube embedded in epoxy resin along its long axis.

21.4° - 21.6° (JCPDS entry 26-1176) of the lithium-deficient phase $LiNb_3O_8$, possibly formed as the product of an interfacial reaction [158] [159] between the $LiNbO_3$ and the silicon oxide covering the pore walls, also shows up.
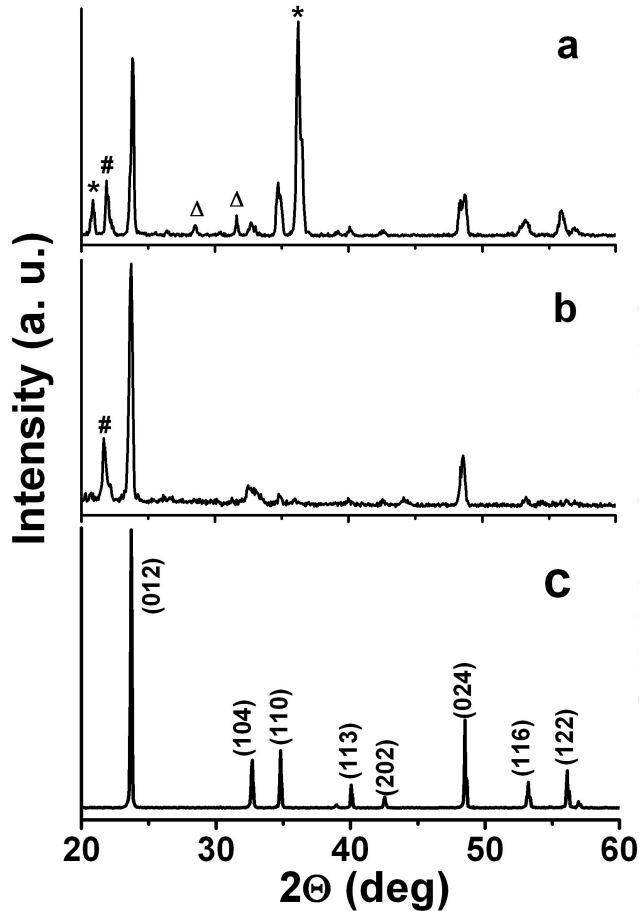
Figure 6.3: XRD pattern on Er:$LiNbO_3$ and $LiNbO_3$ microtubes. (a) Aligned Er:$LiNbO_3$ microtubes embedded in macroporous Si. (b) Completely liberated $LiNbO_3$ microtubes deposited on a Si wafer. (c) Powder pattern measured on a finely milled $LiNbO_3$ single crystal. Reflections originating from $LiNb_3O_8$ are denoted with $\sharp$, those originating form quartz with $*$, and those originating from Si with Δ.

A third set of reflections is found too and can be ascribed to trigonal quartz (space group $P3_221$, JCPDS entry 85-0794), which forms as the silica layer on the pore walls crystallises during annealing in air [126]: the (100) reflection at 20.6°, and the (110) peak at 36.5°. The occurrence of weak (200) and (111) peaks of cubic Si (JCPDS entry 27-1402) at 28.5° and 31.6° indicates that crystallites with a deviating orientation have formed within the (100) oriented Si matrix. Otherwise, the peaks would not appear in the geometry up used for the measurements (Fig. 6.4a). We assume the crystallization of amorphous SiO_2 is induced by Li traces evaporated form the $LiNbO_3$ melt at elevated temperatures [160] [161]. The details are discussed in section of lithium-induced crystallization of amorphous SiO_2 microtubes (section 6.2). XRD investigations on released $LiNbO_3$ microtubes deposited a (100)-oriented Si wafer, however, revealed the absence of quartz and Si after the selective etching of the template by KOH 30 wt-% 90°C 2h. Only $LiNbO_3$ and weak $LiNb_3O_8$ peaks show

74

up (Fig. 6.3b). The relative peak intensities of both patterns are similar to those of the $LiNbO_3$ powder pattern of a milled single crystal fabricated by the Czochralski method (Fig. 6.3c). Macroscopic ensembles of aligned $Er:LiNbO_3$ and $LiNbO_3$ tubes show therefore no apparent texture.
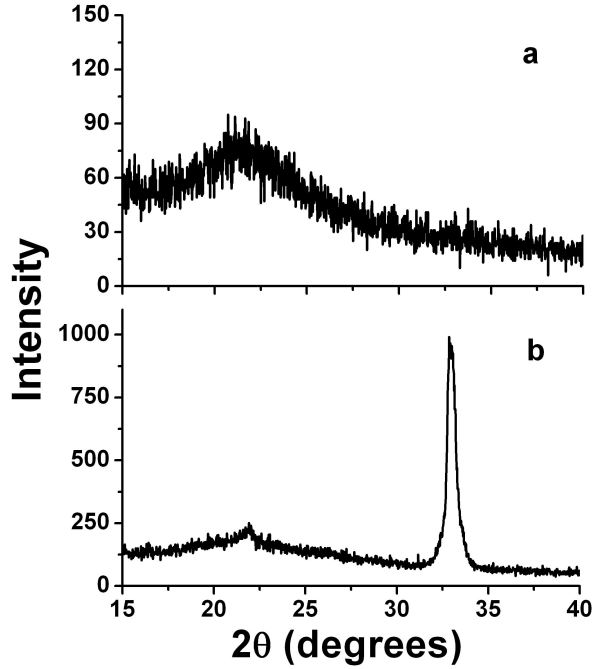
Figure 6.4: XRD patterns of macroporous silicon ($Dp = 1\ \mu m$; $Lp = 100\ \mu m$), alkali annealed (a) in air and (b) in the presence of lithium at 950°C for 2h. in the latter case, a starting (200) reflection of Si appears.

6.1.4 Optical properties of Er:LiNbO$_3$ microtubes

The room temperature PL spectra of $Er:LiNbO_3$ microtubes and bulk $Er:LiNbO_3$ show essentially the same features. The spectra of $Er:LiNbO_3$ microtubes embedded within the pores of the macroporous Si (Fig. 6.1a), released $Er:LiNbO_3$ microtubes deposited on an Si wafer (Fig. 6.1c), and bulk $Er:LiNbO_3$ in the range from 1450 and 1600 nm are presented in Figures 6.5a, b, c, respectively. In all cases a pronounced $^4I_{13/2} \rightarrow\ ^4I_{15/2}$ transition at 1.53 μm appears. The satellite peaks at 1490, 1513, 1547, 1562, 1575, and 1606 nm, respectively, represent the transitions among the multiplet manifolds. This energy-level splitting caused by the crystal field of the matrix indicates that the active Er^{3+} centers are located within a well-defined crystalline environment. The PL of the visible range of $Er:LiNbO_3$ microtubes embedded in the template (Fig. 6.5d), of released $Er:LiNbO_3$ microtubes deposited on a Si wafer (Fig. 6.5e), and of bulk $Er:LiNbO_3$ (Fig. 6.5f) indicates that a rapid non-radiative de-excitation from the excited state $^2K_{15/2}$ to the $^4S_{3/2}$ state takes place. Among the different emissions that can be observed, the $^4S_{3/2} \rightarrow\ ^4I_{15/2}$ (550 nm) and the $^4S_{3/2}$

$\rightarrow {}^4I_{13/2}$ (860 nm) transitions are the most intense ones. The ${}^4I_{11/2}$ state is populated too, predominantly via non-radiative channels, so that the ${}^4I_{11/2} \rightarrow {}^4I_{15/2}$ (980 nm) transition can be detected.
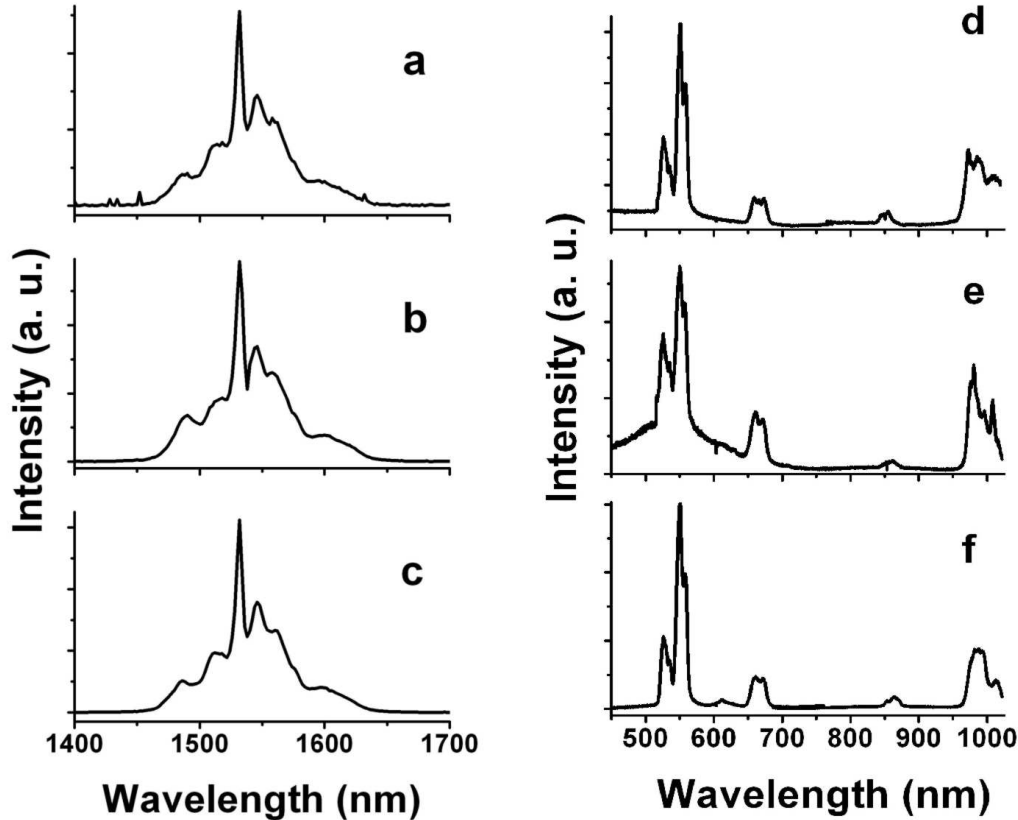
Figure 6.5: Room temperature photoluminescence emission spectra. (a) IR range from Er:LiNbO$_3$ microtubes embedded in macroporous Si. (b) IR range from released Er:LiNbO$_3$ microtubes deposited on a Si wafer. (c) IR range from bulk Er:LiNbO$_3$. (d) Visible range from Er:LiNbO$_3$ microtubes embedded in macroporous Si. (e) Visible range from released Er:LiNbO$_3$ microtubes deposited on a Si wafer. (f) Visible range from bulk Er:LiNbO$_3$.

6.1.5 High-temperature melt wetting

The question arises as to how the Er^{3+}-doped LiNbO$_3$ move into the template pores? Vacuum melting combined with high-pressure injection of melts of various inorganic materials into the nanopores of anodic alumina [162] was employed to obtain solid nanowires. However, no external driving force is required to infiltrate liquid Er:LiNbO$_3$ into macroporous Si. The pore walls of macroprous silicon are covered with a native silica layer which has a quiet high surface energy of the order of 520

mN/m [163]. The surface energy of molten LiNbO$_3$, which lies in the range from 310 to 320 mN/m [164], may be sufficiently low for a complete wetting of the solid pore walls. Moreover, the interfacial reaction leading to the formation of LiNb$_3$O$_8$ [158] [159], the presence of which has been evidenced by XRD (Fig. 6.3a,b), possibly triggers chemical spreading. The second interesting phenomenon is the stability of the liquid cylindrical Er:LiNbO$_3$ layer covering the pore walls. A general mechanism for the infiltration of pores and capillaries with liquids involves the initial formation of such a wetting film [165] [166]. However, cylindrical liquid films are susceptible to hydrodynamic instabilities [167], leading to the formation of menisci (snap-off). Their interfaces move in opposite direction as more liquid moves into the pore. Eventually, this results in the complete filling of the pore volume with the liquid [165]. In case of disordered polymer melts the infiltration stops after the formation of the wetting layer [25] [168]. This has been attributed to the bulkiness of the macromolecules: The wetting layer comprises only a monolayer of molecules, each of which is in contact with the pore walls. The reason for the stability of the liquid cylindrical Er:LiNbO$_3$ films may be the well-known presence of mesoscopic cluster structures within LiNbO$_3$ melts [169] [170]. The intrinsic short-range order imposed by these clusters would be disturbed by the occurrence of instabilities so that their growth might be suppressed.

In this section, the preparation of Er^{3+}-doped lithium niobate (LiNbO$_3$) microtubes consisting of single-crystalline segments within the pores of macroporous silicon [57] [65] by infiltration of Er:LiNbO$_3$ melts was discussed. Both embedded and released Er:LiNbO$_3$ microtubes show the characteristic photoluminescence of Er^{3+}:LiNbO$_3$ which exhibits rapid non-linear optical response behaviour, low switching power and broad conversion bandwidth and is therefore an attractive host system [171] [172]. Si-based microstructures combined with the functionality of Er:LiNbO$_3$ are potential components for complex device architectures. Moreover, the so called high temperature melt wetting approach presented here may be applicable to other nano- and microstructures than macroporous Si, such as mesoporous Si, artificial opals and their inverse counterparts. Even though the underlying physico-chemical phenomena are not fully understood, the wetting of silica-based micro- and nanostructures with Er:LiNbO$_3$ should have a great potential for the design of micro-scaled, functional optical components.

6.2 Lithium-induced crystallization in amorphous SiO_2 microtubes

Many minerals are known to have the chemical composition SiO_2. The silica (SiO_2) minerals include quartz, tridymite, cristobalite, coesite, stishovite and several others. The polymorphs have different structures, with different symmetries and different physical properties. Each of the polymorphs has both an α- and a β-form. The α-form distorted versions of the β-forms and occurs at lower temperatures and have lower symmetry. Quartz is the most important and best known of silica. It goes through a structural transitions from α-phase (or low-quartz) to the β-phase (or high-quartz) at 573°C. Phase transition of β-form quartz to β-from tridymite occurs at 870°C. Silica (SiO_2) is a biocompatible and bioresorbable material. Especially quartz exhibits pronounced piezoelectric behaviour [173] and is therefore a promising raw material for miniaturized components for sensors, actuators and micro-electromechanical systems (MEMS).

Although amorphous SiO_2 nanostructures and microstructures with various morphologies have been fabricated in a well-controlled manner [174], the access to crystalline SiO_2 nano- and microstructures is still a challenge. This is particularly the case for complex structures such as tubes, which are of considerable interest because of their intrinsic anisotropy. Tubular structures consisting of amorphous SiO_2 are easily accessible by thermal oxidation of the pore walls of macroporous Si. However, to exploit the properties of crystalline SiO_2 in low-dimensional systems, a simple and reliable process for the controlled crystallization of glassy silica is required. We solved this problem by a simple and easy process. Crystalline SiO_2 microtubes were accomplished in macroporous silicon using a so-called lithium-induced crystallization approach, in which trace of lithium serve as catalyst in the crystallization process.

6.2.1 Lithium-induced crystallization in SiO_2

Commonly, only amorphous silica forms by thermal oxidation of crystalline silicon is either in unpatterned or in lithographically patterned form, or can be grown on patterned substrates. Cristobalite nanowires were grown in the presence of carbon [175]. Mesopores in mesoporous silica vanish upon crystallization [176]. Other catalysts that facilitate crystallization in silica class are water [177], noble metals [178], and alkali ions [160]. The silica polymorph that forms depends on the crystallization temperature [179]. Among the alkali metals, Li has been reported to be the most efficient catalyst for the conversion of amorphous silica glass into a crystalline

phase, since incorporation of Li into the amorphous silica results in the highest perturbation of the silica framework [160] [161]. Procedures reported in the literature commonly start from glassy silica containing the metal atoms acting as a catalyst, or they require the presence of water or amorphous carbon. It is obvious that the approaches to catalyze the crystallization of silica are not compatible with state of the art silicon technology and clean room standards. We have overcome this problem by a procedure that combines thermal oxidation of silicon with the crystallization of the silica then formed by traces of Li. Here, we take advantage of the volatility of Li at high temperatures. As it is obvious from our results, it is sufficient to locate a Li source inside the furnace used for the oxidation, which is not in direct contact with the sample being oxidized. Evaporated Li is sufficient to promote crystallization in thermal oxide layers grown on a silicon substrate.

6.2.2 Fabrication of crystalline SiO_2 microtubes

In this section, we show that traces of evaporated lithium trigger crystallization in silica integrated into common silicon microstructures. The selected crystallization temperature determines which polymorph forms. As described in chapter 3, a large ranges of pore diameters and pore lengths in macroporous silicon are accessible by photolithographically pre-patterned, (100)-oriented n-type silicon wafers. As example in case, we have investigated quartz and christobalite microtubes obtained from macroporous silicon (Si) ([57], [65]) with a pore diameter of 1 μm and pore depths ranging from 100 μm to 150 μm. We placed macroporous Si and a crucible containing some lithium niobium isprooxide (LiNb(OC$_3$H$_7$) 5 wt-% solution Alfar Aesar) in a furnace and heated the samples at a rate of 10°C/min to 1050°C, 1100°C and 1200°C, respectively. Then, the samples kept at these temperatures for 2 hours, and subsequently cooled to room temperature at a rate of 1°C/min. The entire procedure was carried out under ambient conditions.

6.2.3 Morphology of SiO_2 microtubes

Figure 6.6a shows a SEM image of the surface of a macroporous Si membrane annealed at 1050°C. The pore walls are SiO_2 microtubes that appear as bright annuli surrounding the pore openings. Apparently, the silica layer has a uniform thickness. We selectively released the SiO_2 tubes either partially or completely by etching the residual Si with 30 wt-% aqueous KOH at 80°C. After an etching time of 15 minutes approximately 30 μm of the tubes were released, whereas the lower tube segments were still embedded into the Si matrix (Fig. 6.6b). After an etching for 90 minutes

the silica tubes are completely liberated. Their high mechanical stability prevents the microtubes from breaking. Fig.1c is a representative SEM image of a single silica microtube with an aspect ratio of 140, corresponding to that of the pores in the macroporous Si that had been oxidized. We note that also in SEM images containing a large number of silica microtubes no short segments of broken tubes are seen (Fig. 6.6c). The walls of the microtubes are smooth and free of defects (Fig. 6.6d). A TEM image of an ultra-thin slice containing a section across a silica microtube is seen in Figure 6.6e (the preparation of ultra-thin slice for TEM investigation were described in section 4.3.4). Its wall broke during the cutting into segments with lengths of 200-500 nm. The wall thickness of around 80-90 nm is in line with the values obtained from the SEM.

6.2.4 X-ray diffraction of SiO$_2$ microtubes

XRD on ensembles single silica microtubes revealed that all three low-pressure SiO$_2$ polymorphs, quartz, tridymite and crystobalite, were obtained depending on the crystallization temperature applied. Figure 6.7 shows XRD patterns of the released SiO$_2$ microtubes, which were deposited on silicon wafers. The samples were crystallized at 1050°C (Fig. 6.7a), 1100°C (Fig. 6.7b) and 1200°C (Fig. 6.7c). A peak centered at $2\theta = 21.9°$, which can be indexed as the (101) reflection of cristobalite (JCPDS: 76-0937), appeared in all three diffraction patterns. In case of the sample crystallized at 1050°C (Fig. 6.7a) strong (100) and (011) peaks of quartz were occur at $2\theta = 20.8°$ and $2\theta = 26.6°$ (JCPDS: 88-2487). Tridymite (JCPDS: 89-3141) traces were also appeared indicated by the appearance of small peaks at 23.2° (101), 30° (102) and 35.8° (110) in figure 6.7b. The reflection signals of cristobalite increase with increasing of the annealing temperature, for the sample annealed at 1200°C, a pure cristobalite phase was achieved (Fig. 6.7c).

6.2.5 Electron diffraction pattern of SiO$_2$ microtubes

Different SiO$_2$ polymorphs were observed by TEM. For the sample with thermal oxidation at 1050°C, quartz (hexagonal; P3$_2$21; zone axis $\langle 001 \rangle$) was the dominate phase. Figure 6.8b shows a representative SAED pattern with the Bragg spots corresponding to the (110) and (-210) reflections of hexagonal quartz, indicating the single crystalline nature of the microtubes. Tridymite (hexagonal; P63/mmc; zone axis $\langle 001 \rangle$) appeared when increasing the temperature to 1100°C (Fig. 6.8c, d). The Bragg spots, shown in Figure 6.8e, is arise due to (-100) and (2-10) reflections of the hexagonal tridymite. Cristobalite (tetragonal; P4$_1$2$_1$2; zone axis $\langle 001 \rangle$) was finally
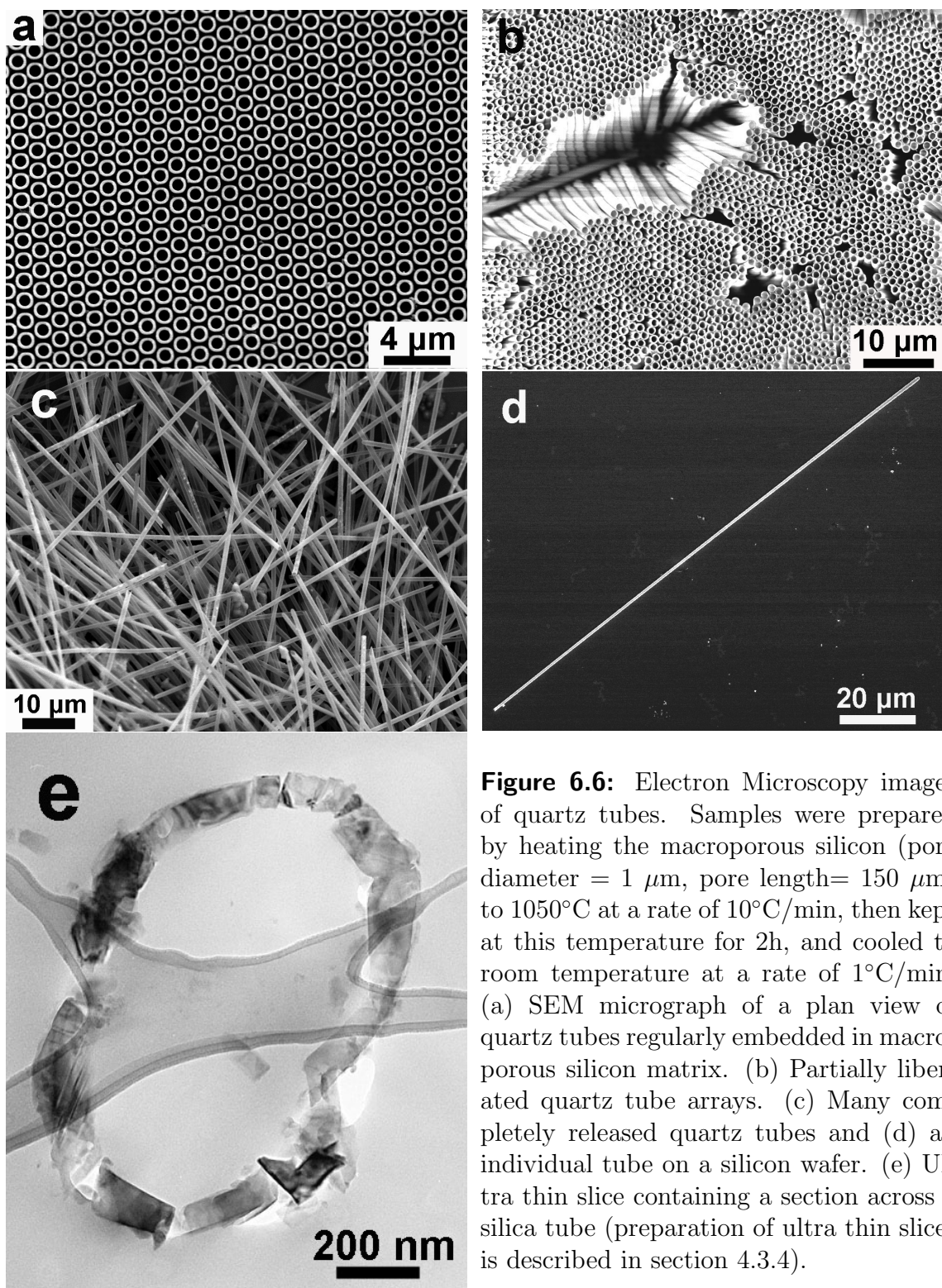
Figure 6.6: Electron Microscopy images of quartz tubes. Samples were prepared by heating the macroporous silicon (pore diameter = 1 μm, pore length= 150 μm) to 1050°C at a rate of 10°C/min, then kept at this temperature for 2h, and cooled to room temperature at a rate of 1°C/min. (a) SEM micrograph of a plan view of quartz tubes regularly embedded in macroporous silicon matrix. (b) Partially liberated quartz tube arrays. (c) Many completely released quartz tubes and (d) an individual tube on a silicon wafer. (e) Ultra thin slice containing a section across a silica tube (preparation of ultra thin slices is described in section 4.3.4).
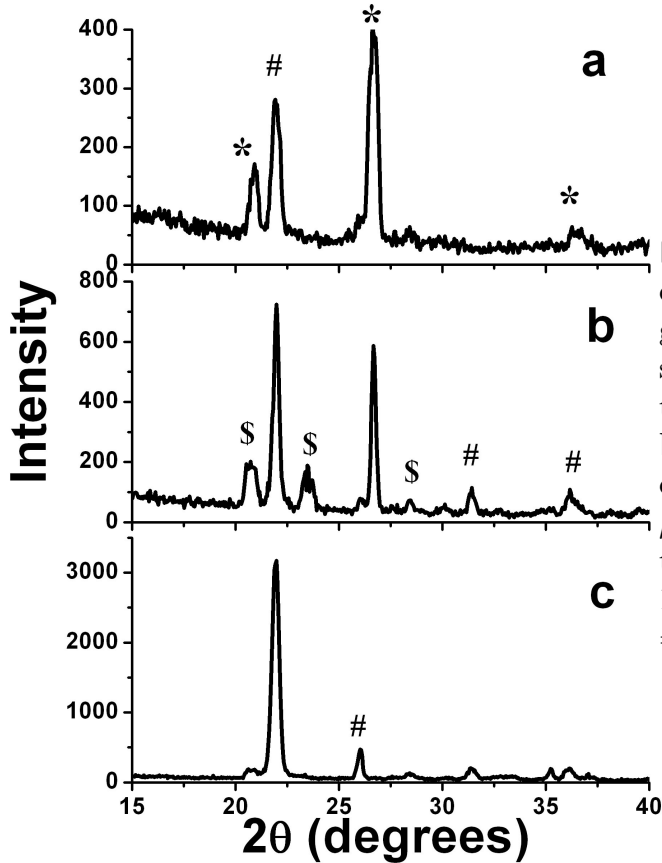
Figure 6.7: Crystal modification of SiO_2 microtubes was investigated by $\theta/2\theta$ scans. XRD results of complete released microtubes on silicon wafer, obtained by thermal oxidation of macroporous Si (Dp =1 μm; Lp = 100 μm) in lithium for 2h at temperature of (a) 1050°C, (b) 1100°C, (c) 1200°C. (*: quartz, \$: tridymite, #: cristobalite).

achieved at 1200°C (Fig. 6.8e, f). The Bragg spots in the SAED pattern shown in Figure 6.8f can be assigned to (-110) and (200) reflections of the tetragonal cristobalite structure. No amorphous silica is present in the tubes subjected to thermal oxidation in the presence of lithium. Under our preparation conditions, we believe the microtubes are first formed in the α-form, and are then converted to the β-form on further heating and cooling to room temperature. The SAED-pattern of SiO_2 microtubes at different temperatures reveal that TEM investigations are in good agreement with that of XRD.

6.2.6 SiO$_2$ thin films

In order to demonstrate that lithium actually acted as a catalyst and induced the SiO_2 amorphous/crystalline phase transitions, we explored the thermal oxidation of a flat Si wafer. As expected, the thermal oxidation of Si conducted under the same oxidation conditions but in a furnace without Li contaminations exclusively yielded amorphous SiO_2. In contrast, a cristobalite thin film was obtained by thermal oxidation of a silicon wafer at 1250°C in the presence of lithium for 2h. Figure 6.9 is the XRD
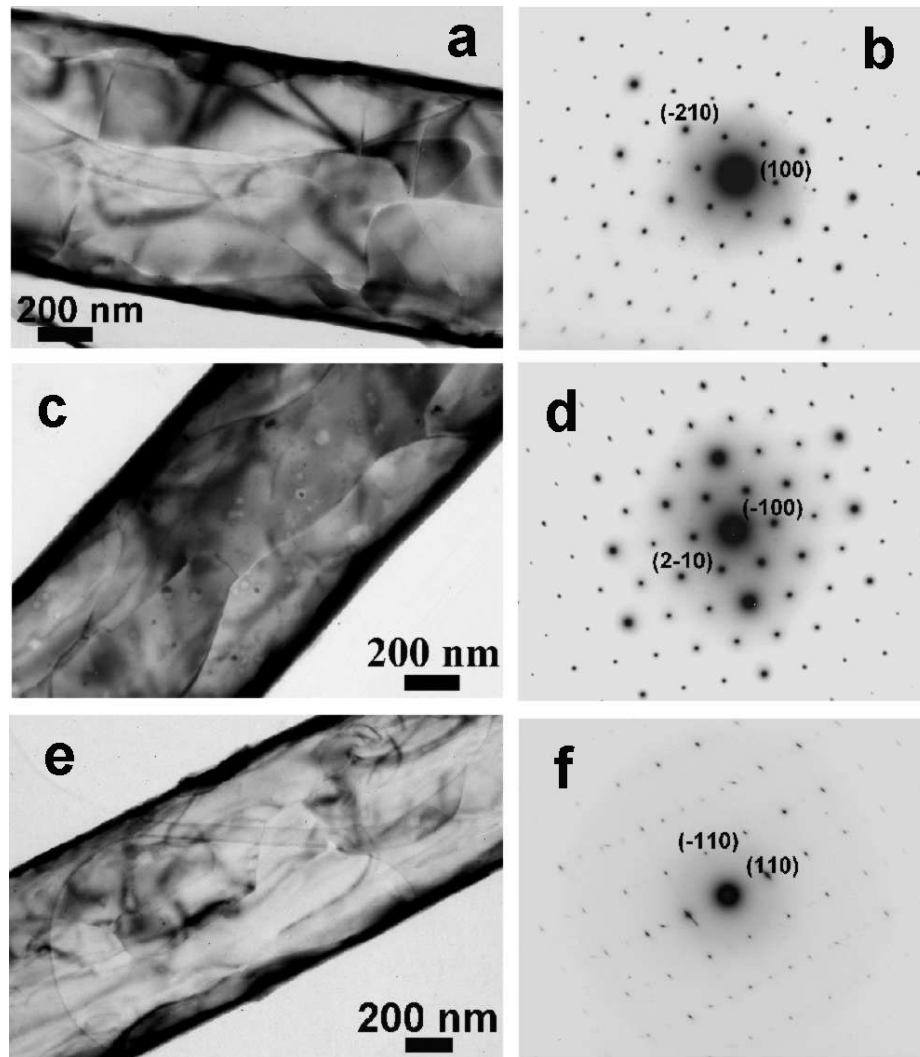
Figure 6.8: TEM investigation on SiO_2 microtubes. The samples were prepared by thermal oxidation of macroporous Si (Dp= 1 μm, Lp= 100 μm) at temperatures of 1050°C, 1100°C, 1200°C in the presence of lithium, respectively. (a) Quartz (hexagonal) microtubes obtained at 1050°C. (b) Its selected area electron diffraction pattern (SAED). (c) Tridymite tubes obtained at 1100°C. (d) Its selected area electron diffraction pattern (SAED). (e) Cristobalite (tetragonal) microtubes obtained at 1200°C. (f) Its selected area electron diffraction pattern (SAED) (lattice reflections are indexed).

pattern of a SiO$_2$ thin film fabricated by annealing the silicon wafer in the presence of lithium at 1250°C. As expected, the pure cristobalite phase was obtained. The peak at $2\theta = 32.8°$ is the (200) reflection of Si forbidden peak which only occurs when the Si lattice is distorted. XRD results reveal that the effect of the temperature on the phase transition does not follow exactly the thermodynamic stability order of the pure silica phases.
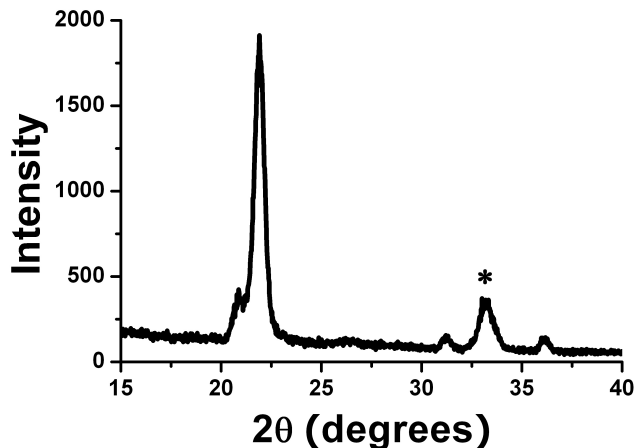
Figure 6.9: XRD pattern of SiO$_2$ thin film obtained by annealing Si wafer in present of lithium at 1250°C for 2h (*: Si(200)).

TEM images of SiO$_2$ thin film cross sections are shown in Figure 6.10 (the cross section X-TEM specimen preparation procedure is discussed in section 4.3.4). The thin film has a thickness of around 800 nm. The bright field image (Fig. 6.10a) together with the corresponding dark field (Fig. 6.10b) image indicates that the thin film has single-crystalline segments extending several square micrometers. The occurrence of spots in a typical SAED in Figure 6.10c can be assigned to the (111), (0-11) of cristobalite (tetragonal, P4$_1$2$_1$2). Energy dispersive X-ray analysis (EDX) proves stoichiometric SiO$_2$ tubes were obtained. The features of the electron energy loss spectroscopy (EELS) spectrum coincides with that of a standard SiO$_2$ (Fig. 6.10d).

In summary, SiO$_2$ crystalline microtubes with a pore diameter of 1 μm, and pore lengths from 100 to 150 μm were fabricated by thermal oxidation of macroporous silicon in the presence of lithium. All the three SiO$_2$ low pressure phases, quartz, tridymite, and crystobalite, were obtained by varying the annealing temperature from 1050°C to 1200°C. In addition, a highly crystalline SiO$_2$ thin films were obtained by annealing the Si wafer in lithium at 1250°C for 2h. We believe that the study of lithium-induced crystallization in amorphous SiO$_2$ microtubes is of high significance because it demonstrates a novel and simple approach to fabricate crystalline SiO$_2$ nano- and microstructures.
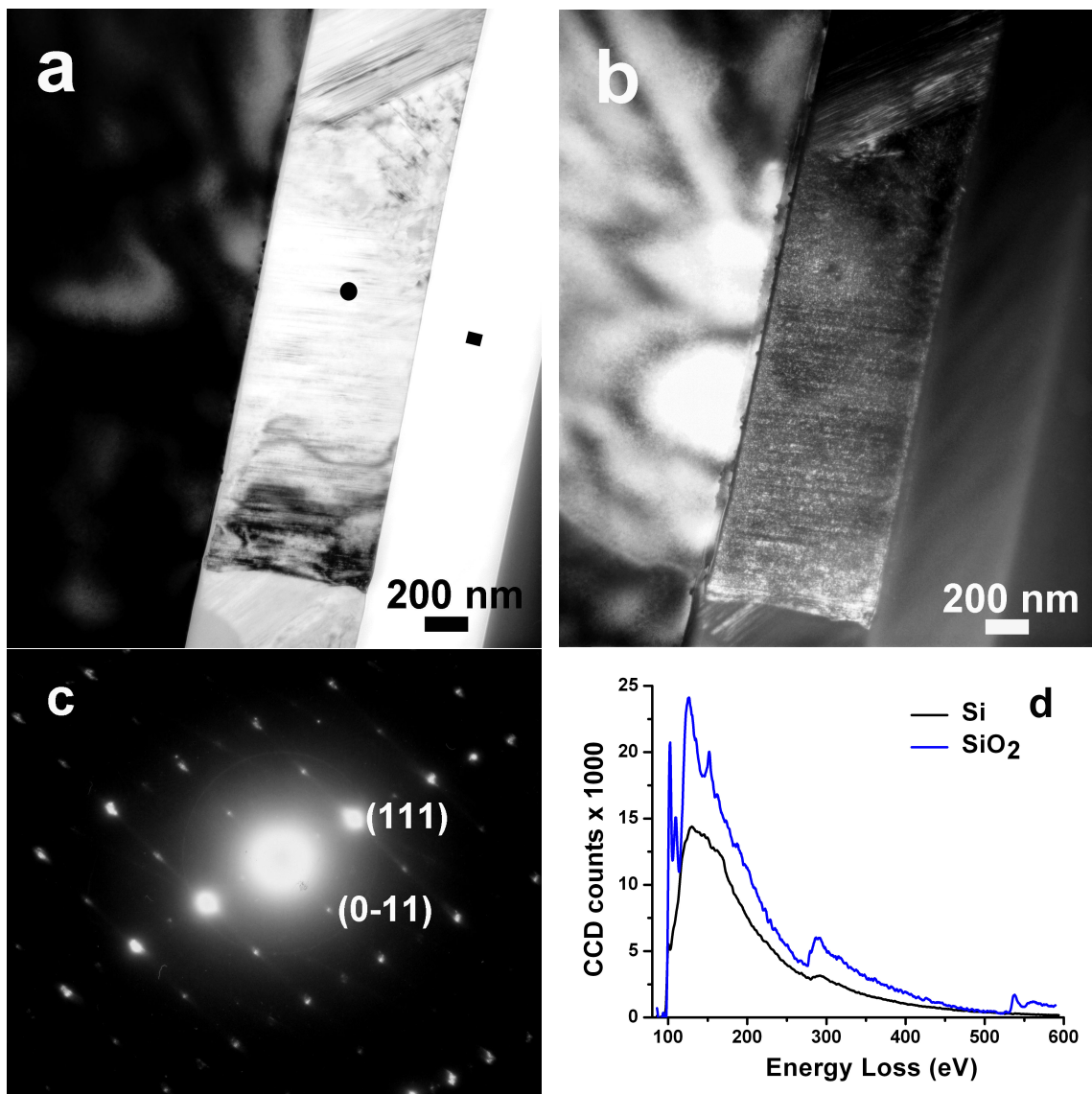
Figure 6.10: TEM cross section investigations on SiO_2 (cristobalite) thin film. Sample are prepared by heating Si wafer in lithium to 1250°C at a rate of 10°C/min, kept at this temperature for 2 hours, and cooled to room temperature at a rate of 1°C/min. (a) Bright field. (b) Dark field image. (c) A typical selected area electron diffraction pattern (SAED image). (d) EELS of the thin film, measured at the location indicated in (a).

6.3 Summary of the chapter

Modification of macroporous silicon by microtubes, either $LiNbO_3$ and $Er:LiNbO_3$ or crystalline SiO_2 microtubes was discussed in the chapter. $LiNbO_3$ and $Er:LiNbO_3$ microtubes were prepared by a modified templated high-temperature conversion approach, so-called high temperature melt wetting. Crystalline SiO_2 microtubes were fabricated by crystallization of thermally grown amorphous SiO_2 tubes in macroporous silicon templates in the presence of trace amount of lithium.

CHAPTER VII

Conclusions and outlook

The aim of the thesis is to develop a generic procedure for the production of 1D nanostructures and microstructures by templated high-temperature conversion using ordered porous materials as templates and reactants as well as characterization in terms of structure and other relevant properties. It was demonstrated in this thesis that templated high-temperature conversion is a versatile synthetic protocol for a uniform fabrication procedure. It did not only allow to fabricate high-quality 1D nanostructures and microstructures of metals, II/VI- or IV/VI-semiconductors and their derivatives but also made modified the macroporous Si using functional inorganic oxide microtube hybrid systems accessible.

The formation of tubes and rods consisting of II/VI semiconductors, IV/VI semi-conductors and metals from a set of specifically designed single source precursors of the organochalcogenolate type were investigated. The precursors are very similar in their molecular architecture, and they have similar thermal and wetting properties. Therefore, it was possible to fabricate 1D nanostructures and microstructures from a broad range of target materials by the same preparative procedure. CdSe nanowires and microtubes were prepared by thermolysis of Cd(SePh)$_2$·TMEDA wetted templates, under conditions where the templates are inert. This is an example where the porous materials served only as a "mold" to direct the dimension of the nano-objects and micro-objects. Single-crystalline CdSe nanowires with a diameter of 25 nm exhibiting the characteristic photoluminescence of bulk CdSe were obtained. A preliminary investigation of the growth mechanism of single-crystalline CdSe nanowires was performed (chapter 5).

Porous templates (ordered porous alumina and macroporous silicon) can not only serve as "mold" to define the morphology but also may react with the nano- and micromaterials in the pores. High temperature chemical transformations exploiting the oxidizing and reducing properties of the templates further extend the range of accessible target materials the 1D nanostructures and microstructures may consist of. Templated conversion of SnSe into elemental Sn and SnO$_2$ was shown as an example demonstrating that the selective reactivity of the pore walls of porous alumina and macroporous silicon may not just cause a surface modification but may lead to a

complete conversion of the 1D nano-objects and micro-objects. This procedure allows the preparation of monodisperse tubes and nanowires of three different target materials SnSe, SnO_2 and Sn from one single-source precursor $Sn(SePh)_4$. Besides the redox reaction, the template pore walls may directly react with the nano- and micromaterials in the pores. As example of a porous template serveing as a reactant high temperature thermolysis of the single source precursor $Zn(TePh)_2 \cdot TMEDA$ was investigated. Dependent on the experimental conditions applied, single-crystalline nanowires of zinc telluride (ZnTe), zinc spinel/tellurium and tellurium ($ZnAl_2O_4$-Te) or $ZnAl_2O_4$ nanotubes were obtained.

In order to exploit the versatility of the templated high-temperature conversions approach, the modification of macroporous silicon with functional inorganic oxide microtubes was investigated. Macroporous silicon is a 2D photonic band gap materials. Modification of macroporous silicon by functional oxide microtubes yields hybrid systems consisting of billions of aligned functionalized channels, which have a great potential for micrometer-scale, functional optical components in micro-devices. As selected example $LiNbO_3$ and $Er:LiNbO_3$ microtubes were prepared by directly infiltration $LiNbO_3$ and $Er:LiNbO_3$ melts into the template pores. This is the so called high-temperature melt wetting (chapter 6). Optical spectroscopy on the obtained $LiNbO_3$ and $Er:LiNbO_3$ microtubes reveals that both embedded and released $Er:LiNbO_3$ microtubes show the characteristic photoluminescence of $Er:LiNbO_3$. Si-based microstructures combined with the functionality of $Er:LiNbO_3$ are potential components for complex device architectures. Finally, crystalline SiO_2 mirotubes were fabricated by thermal oxidization of macroporous silicon in the presence of lithium. All the three SiO_2 low pressure phases, including quartz, tridymite, crystobalite, were obtained by varying the annealing temperature from 1050°C to 1200°C.

This study of the templated high-temperature conversions proved that it is a simple and generic procedure to fabricate high quality functional 1D nanostructures and microstructures, either as arrays or powders. It should easily be possible to adapt the proposed templated high-temperature conversion method to other types of precursors. Moreover, the approach presented here may be applicable to nano- and microporous materials other than ordered porous alumina and macroporous Si, such as mesoporous Si, artificial opals, and their inverse counterparts.

Bibliography

[1] Y. Cui, X. Duan, J. Hu, and C. M. Lieber. *J. Phys. Chem. B*, 104:5213, 2001.

[2] X. Duan, Y. Huang, Y. Cui, J. Wang, and C. M. Lieber. *Nature*, 409:66, 2001.

[3] Y. Cui and C. M. Lieber. *Science*, 291:851, 2001.

[4] Y. Huang, X. Duan, Y. Cui, L. J. Lauhon, K. Kim, and C. M. Lieber. *Science*, 294:1313, 2001.

[5] V. Golod, D. Grützmacher, C. David, E. Deckhardt, O. Kirfel, S. Mentese, and B. Ketterer. *Microelectron. Eng.*, 67-68:595, 2003.

[6] Y. Luo, I. Szafraniak, N. D. Zakharov, V. Nagarajan, M. Steinhart, R. B. Wehrspohn, J. H. Wendorffand, R. Ramesh, and M. Alexe. *Appl. Phys. Lett.*, 83:440, 2003.

[7] A. M. Morales and C. M. Lieber. *Science*, 279:208, 1998.

[8] X. F. Duan and C. M. Lieber. *Adv. Mater.*, 12:298, 2000.

[9] T. M. Whitney, J. S. Jinag, P. C. Searson, and C. L. Chien. *Science*, 261:1316, 1993.

[10] T. J. Trentler, K. M. Hickman, S. C. Geol, A. M. Viano, P. C. Gibbons, and W. E. Buhro. *Science*, 270:1791, 1995.

[11] R. Tenne, L. Marglis, M. Genut, and G. Hodes. *Nature*, 360:444, 1992.

[12] M. Nath and C. N. R. Rao. *J. Am. Chem. Soc.*, 123:4841, 2001.

[13] C. R. Martin. *Adv. Mater.*, 3:457, 1991.

[14] V. Ya. Prinz, V. A. Seleznev, A. K. Gutakovsky, A. V. Chehovskiy, V. V. Preobrazhenskii, M. A. Putyato, and T. A. Gavrilova. *Physicca E*, 6:828, 2000.

[15] M. Remskar, Z. Skraba, C. Ballif, R. Sanjines, and F. Levy. *Adv. Mater.*, 10:246, 1998.

[16] Z. Y. Pan, X. J. Liu, S. Y. Zhang, G. J. Shen, L. G. Zhang, Z. H. Lu, and J.Z. Liu. *J. Phys. Chem. B*, 101:9703, 1997.

[17] I. Willner, F. Patolsky, and J. Wasserman. *Angew. Chem. Int. Ed.*, 40:1861, 2001.

[18] M. H. Huang, S. Mao, H. Feick, H. Q. Yan, Y. Y. Wu, H. Kind, E. Weber, R. Russo, and P. D. Yang. *Science*, 292:1897, 2001.

[19] N. A. Melosh, A. Boukai, F. Diana, B. Gerardot, A. Badolato, P. M. Petroff, and J. R. Heath. *Science*, 300:112, 2003.

[20] A. M. Morales and C. M. Lieber. *Science*, 279:208, 1998.

[21] D. P. Yu, C. S. Lee, I. Bello, X. S. Sun, Y. H. Tang, G. W. Zhou, Z. G. Bai, Z. Zhang, and S. Q. Feng. *Solid State Commun.*, 105:403, 1998.

[22] Z. G. Bai, D. P. Yu, H. Z. Zhang, Y. Ding, Y. P. Wang, X. Z. Gai, Q. L. Hang, G. C. Xiong, and S. Q. Feng. *Chem. Phys. Lett.*, 303:311, 1999.

[23] C. R. Martin. *Science*, 266:1961, 1994.

[24] D. Routkevitch, T. Bigioni, M. Moskovits, and J. M. Xu. *J. Phys. Chem.*, 100:14037, 1996.

[25] M. Steinhart, J. H. Wendorff, A. Greiner, R. B. Wehrspohn, K. Nielsch, J. Schilling, J. Choi, and U. Gösele. *Science*, 296.

[26] J. Choi, G. Sauer, P. Göring, K. Nielsch, R. B. Wehrspohn, and U. Gösele. *J. Mater. Chem.*, 13:1100, 2003.

[27] B. B. Lakshmi, P. K. Dorhout, and C. R. Martin. *Chem. Mater.*, 9:857, 1997.

[28] J. C. Johnson, H. J. Choi, K. P. Knutsen, R. D. Schaller, P. D. Yang, , and R. J. Saykally. *Nature Materials*, 1:106, 2002.

[29] Y. Y. Wu, H. Q. Yan, and P. D. Yang. *Top. Catal.*, 19:197, 2002.

[30] X. F. Duan, Y. Huang, R. Agarwal, and C. M. Lieber. *Nature*, 421:241, 2003.

[31] V. C. Sundar, J. Lee, J. R. Heine, M. G. Bawendi, and K. F. Jensen. *Adv. Mater.*, 12:1102, 2000.

[32] W. U. Huynh, J. J. Dittmer, and A. P. Alivisatos. *Science*, 295:2425, 2002.

[33] J. C. Hulteen and C. R. Martin. *J. Mater. Chem.*, 7:1075, 1997.

[34] B. Cheng and E. T. Samulski. *J. Mater. Chem.*, 11:2901, 2001.

[35] B. A. Hernandez, K. S. Chang, E. R. Fisher, and P. K. Dorhout. *Chem. Mater.*, 14:480, 2002.

[36] Y. Luo. Functional nanostructures by ordered porous tempates. *Thesis*, 2005.

[37] Z. J. Karpinski and R. A. Osteryoung. *J. Electroanal. Chem.*, 349:285, 1993.

[38] C. R. Martin. *Chem. Mater.*, 8:1739, 1996.

[39] S. M. Drew and R. M. Wrightman. *J. Electroanal. Chem.*, 317:117, 1991.

[40] H. Daimon and O. Kitakami. *J. Appl. Phys.*, 73:5391, 1993.

[41] E. Matijevic. *Langmuir*, 10:8, 1994.

[42] G. C. Krueger and C. W. Miller. *J. Chem. Phys.*, 21:2018, 1953.

[43] Y. J. Xiong, B. T. Mayers, and Y. N. Xia. *Chem.Comm.*, 40:5013, 2005.

[44] S. D. Dingman, N. P. Rath, P. D. Markowitz, P. C. Gibbons, and W. E. Buhro. *Angew. Chem. Ent. Ed.*, 39:1470, 2000.

[45] Z. Y.Tang, N. A. Kotov, and M. Giersig. *Science*, 297:237, 2002.

[46] X. Jiang, Y. Xie, J. Liu, L. Y. Zhu, W. He, and Y. T. Qian. *Chem. Mater.*, 13:1213, 2001.

[47] Y. F. Liu, J. H. Zeng, W. X. Zhang, W. C. Yu, Y. T. Qian, J. B. Cao, and W. Q. Zhang. *J.Mater.Res.*, 16:3361, 2001.

[48] X. Peng. *Nature*, 404:59, 2000.

[49] B. Nikoobakht, Z. L. Wang, and M. A. El-Sayed. *J. Phys. Chem. B*, 104:8635, 2000.

[50] P. C. Ohara, J. R. Heath, and W. M. Gelbart. *Angew. Chem. Ent. Ed.*, 36:1078, 1997.

[51] W. Z. Li, S. S. Xie, L. X. Qian, B. H. Chang, B. S. Zou, W. Y. Zhou, R. A. Zhao, and G. Wang. *Science*, 274:1701, 1996.

[52] C. G. Wu and T. Bein. *Science*, 264:1757, 1994.

[53] C. Guerret-Piecourt, Y. L. Bouar, A. Loiseau, and H. Pascard. *Nature*, 372:761, 1994.

[54] C. G. Wu and T. Bein. *Science*, 266:1013, 1994.

[55] H. Masuda and K. Fukuda. *Science*, 268:1466, 1995.

[56] H. Masuda, F. Hasegawa, and S. Ono. *J. Electrochem. Soc.*, 144:L127, 1997.

[57] V. Lehmann. *J. Electrochem. Soc*, 140:2836, 1993.

[58] G. Che, B. B. Lakshmi, C. R. Martin, and E. R. Fisher. *Chem. Mater.*, 10:260, 1998.

[59] C. A. Foss, J. Hornyak, G. L. Stockert, and J. A. Martin. *J. Phys. Chem.*, 98:2963, 1994.

[60] V. P. Menon and C. R. Martin. *Anal. Chem.*, 67:192, 1995.

[61] V. M. Copak and C. R. Martin. *Chem. Mater.*, 11:1363, 1999.

[62] M. L. Hitchman and K. F. Jensen. Chemical vapor deposition. *Academic Press: San Diego*, CA, 1993.

[63] M. Terrones, N. Grobert, J. Olivares, J. P. Zhang, H. Terrones, K. Kordatos, W. K. Hsu, J. P. Hare, P. D. Townsend, K. Prassides, A. K. Cheetham, H. W. Kroto, and D. R. M. Walton. *Nature*, 388:52, 1997.

[64] G. Che, B. B. Lakshmi, E. R. Fisher, and C. R. Martin. *Nature*, 393:346, 1998.

[65] A. Birner, U. Göring, S. Ottow, A. Schneider, F. Müller, V. Lehmann, H. Föll, and U. Gösele U. *Phys. Stat. Sol. A*, 165:111, 1998.

[66] B. J. Holliday and C. A. Mirkin. *Angew. Chem. Int. Ed.*, 40:2022, 2001.

[67] R. M. Penner and C. R. Martini. *Anal. Chem.*, 59:2625, 1987.

[68] C. R. Martin. *Chem. Mater.*, 8:1739, 1996.

[69] C. J. Brumlik and C. R. Martin. *J. Am. Chem. Soc*, 113:3174, 1991.

[70] C. J. Brumlik, V. P. Menon, and C. R. Martin. *J. Mater. Res.*, 9:1174, 1994.

[71] R. M. Penner and C. R. Martin. *J. Electrochem. Soc.*, 133:2206, 1986.

[72] L. S. Van Dyke and C. R. Martin. *Langmuir*, 6:1123, 1990.

[73] S. R. Nicewarmer-Pena, R. G. Freeman, B. R., Reiss, L. He, I. D. Walton, R. Cromer, C. D. Keating, and M. J. Natan. *Science*, 294:137, 2001.

[74] M. Chen, P. C. Searson, and C. L. Chien. *J. Appl. Phys.*, 93:8253, 2003.

[75] E. W. Wong, B. W. Maynor, L. D. Burns, and C. M. Lieber. *Chem. Mater.*, 8:2041, 1996.

[76] M. Steinhart, Z. H. Jia, A. K. Schaper, R. B. Wehrspohn, U. Gösele, and J. H. Wendorff. *Adv. Mater.*, 15:706, 2003.

[77] Y. Luo, S. K. Lee, H. Hofmeister, M. Steinhart, and U. Gösele. *Nano Lett.*, 4:143, 2004.

[78] L. L. Zhao, M. Steinhart, M. Yosef, S. K. Lee, U. Gösele, and S. Schlecht. *Sensors and Actuators B*, 109:86, 2005.

[79] H. W. Fox, E. F. Hare, and W. A Zisman. *J. Phys. Chem.*, 59:1097, 1955.

[80] J. W. Diggle, T. C. Downie, and C. W. Goulding. *Chem. Rev.*, 69:365, 1969.

[81] J. P. O'Sullivan and G. C. Wood. *Proc. R. Soc. London Ser. A*, 317:511, 1970.

[82] C. Pollak. Anodised electrical condensers und current directing devices. *British Patent No. 933*, 1898.

[83] O. Jessensky, F. Müller, and U. Gösele. *Appl. Phys. Lett.*, 72:1173, 1998.

[84] A. P. Li, F. Müller, A. Birner, K. Nielsch, and U. Gösele. *J. Appl. Phys.*, 84:6023, 1998.

[85] K. Nielsch, J. Choi, K. Schwirn, R. B. Wehrspohn, and U. Gösele. *Nano Lett.*, 2:677, 2002.

[86] J. Choi, K. Nielsch, M. Reiche, R. B. Wehrspohn, and U. Gösele. *J. Vac. Sci. Techn. B*, 21:763, 2003.

[87] H. Masuda, H. Yamada, M. Satoh, M. Nakao H. Asoh, and T. Tamamura. *Appl. Phys. Lett.*, 71:2770, 1997.

[88] J. Choi. Thesis. *Martin-Luther-Universit at Halle-Wittenberg*, Germany, 2004.

[89] H. Masuda, M. Ohya, K. Nishio, H. Asoh, M. Nakao, M. Nohtomi, A. Yokoo, and T. Tamamura. *Jpn. J. Appl. Phys. 2*, 39:L1039, 2000.

[90] B. Vanderlinden, H. Terryn, and J. Vereecken. *J. Appl. Electrochem.*, 20:798, 1990.

[91] V. Lehmann and H. J. Föll. *J. Electrochem. Soc.*, 137:653, 1990.

[92] J. N. Chazalviel, F. Ozanam, and R. B. Wehrspohn. *J. Electrochem. Soc.*, 149:C511, 2002.

[93] R. B. Wehrspohn and J. Schilling. *Mater. Res. Bull.*, 8:62, 2001.

[94] J. Brulev, V. J. Keast, and D. B. Williams. *J. Phys. D*, 29:1730, 1996.

[95] R. F. Egerton and J. C. Bennett. *J. Microscopy-Oxford*, 183:116, 1996.

[96] K. Lie, R. Hoier, and R. Brydson. *Phy. Rev. B*, 61:1786, 2000.

[97] Y. Xia, P. D. Yang, Y. Sun, Y. Wu, B. Mayers, B. Gates, Y. Yin, F. Kim, and H. Yan. *Adv. Mater.*, 15:353, 2003.

[98] R. Tenne, M. Homyonfer, and Y. Feldman. *Chem. Mater.*, 10:3225, 1998.

[99] H. Masuda, T. Mizuno, N. Baba, and T. Ohmori. *J. Electroanal. Chem.*, 368:333, 1994.

[100] Y. Jun, C. S. Choi, and J. Cheon. *Chem. Commun*, 1:101, 2001.

[101] Y. Jun, J. E. Koo, and J. Cheon. *Chem. Commun.*, 14:1243, 2000.

[102] M. Yosef, A. K. Schaper, M. Froeba, and S. Schlecht. *Inorg. Chem*, 44:5890, 2005.

[103] F. Shieh, A. E. Saunders, and B. A. Korgel. *J. Phys. Chem. B*, 109:8538, 2005.

[104] H. Pfistner and D. Z. Fenske. *Anorg. Allg. Chem.*, 627:575, 2001.

[105] S. Schlecht, M. Budde, and L. Kienle. *Inorg. Chem.*, 41:6001, 2002.

[106] Y. Cui, Q. Wei, H. K. Park, and C. M. Lieber. *Science*, 293:1289, 2001.

[107] D. Xu, X. Shi, G. Guo, L. Gui, and Y. Tabg. *J. Phys. Chem. B*, 104:5061, 2000.

[108] A. P. Alivisatos. *Science*, 289:736, 2000.

[109] X. C. Jiang, B. Mayers, T. Herricks, and N. Y. Xia. *Adv. Mater*, 15:1740, 2003.

[110] M. Artemyev, B. Moeller, and U. Woggon. *Nano Lett.*, 3:509, 2003.

[111] J. T. Hu, L. S. Li, W. D. Yang, J. Wickham, E. Scher, A. Kadavanich, and A. P. Alivisatos. *Science*, 292:2060, 2001.

[112] D. Xu, X. Shi, G. Guo, L. Gui, and Y.Tabg. *J. Phys Chem B*, 104:5061, 2000.

[113] W. U. Huynh, J. J. Dittmer, and A. P. Alivisatos. *Science*, 295:2425, 2002.

[114] X. C. Jiang, B. Mayers, HT. erricks, and T. Nxia. *Adv. Mater.*, 15:1740, 2003.

[115] A. P. Alivisatos. *Science*, 271:933, 1996.

[116] P. Göring, E. Pippel, H. Hofmeister, R. B. Wehrspohn, M. Steinhart, and U. Gösele. *Nano Lett.*, 4:1121, 2004.

[117] P. Pelce. *Dynamics of Curved Fronts, Academic Press, San Diego*, 1988.

[118] J. G. McLean, B. Krishnamachari, D. R. Peale, E. Chason, J. P. Sethna, and B. H. Cooper. *Phys. Rev. B*, 55:1811, 1997.

[119] W. Z. Ostwald. *Phys. Chem*, 34:495, 1900.

[120] R. L. Penn and J. F. Banfield. *Science*, 281:969, 1998.

[121] N. Pradhan, H. F. Xu, and X. G. Peng. *Nano Lett*, 6:720, 2006.

[122] Y. Jun, J. S. Choi, and J. Cheon. *Angew. Chem. Int. Ed.*, 45:3414, 2006.

[123] L. Manna, L. W. Wang, R. Cingolani, and A. P. Alivisatos. *J Phys. Chem B*, 109:6183, 2005.

[124] Landolt-Boernstein. Numerical data and functional relatonships in science and technology. *group III*, 22.

[125] J. Choi, Y. Luo, R. B. Wehrspohn, R. Hillebrand, J. Schilling, and U. Gösele. *J. Appl. Phys.*, 94:8, 2003.

[126] L. L. Zhao, M. Steinhart, M. Yosef, S. K. Lee, T. Geppert, E. Pippel, R. Scholz, U. Gösele, and S. Schlecht. *Chem. Mater*, 17:3, 2005.

[127] R. Kniep, P. Lamparter, and S. Steeb. *Angew. Chem.*, 101:975, 1989.

[128] M. T. S. Nairand P. K. Nair. *Semicond. Sci. Technol.*, 6:132, 1991.

[129] K. Bindu and P. K. Nair. *Semicond. Sci. Technol.*, 19:1348, 2004.

[130] A. Bennouna, P. Y. Tessier, M. Priol, Q. Dang Tran, and S. Robin. *Phys. Status Solidi B*, 51:117, 1983.

[131] T. Subba Rao, B. K. Samanata Ray, and A. K. Chaudhuri. *Thin Solid Films*, 165:257, 1988.

[132] Y. G. Gao, J. S. Hu, H. M. Zhang, H. P. Liang, L. J. Wan, and C. L. Bai. *Adv. Mater.*, 17:746, 2005.

[133] J. G. Wang, M. L. Tian, T. E. Mallouk, and M. H. W. Chan. *Nano. Lett.*, 4:1313, 2004.

[134] M. L. Tian, J. Wang, J. Snyder, J. Kurtz, Y. Liu, P. Schiffer, T. E. Mallouk, and M. H.W. Chan. *Appl. Phys. Lett.*, 83:1620, 2003.

[135] L. L. Zhao, M. Steinhart, M. Yosef, S. K. Lee, T. Geppert, E. Pippel, R. Scholz, U. Gösele, and S. Schlecht. *Chem. Mater.*, 17:3, 2005.

[136] Y. Ding and Z. L. Wang. *J. Phys. Chem. B*, 108:12280, 2004.

[137] P. Fengand, Q. Wan, and T. H. Wang. *Appl. Phys. Lett.*, 87:213111, 2005.

[138] A. V. Nurmikko and R. L. Gunshor. *Solid State Physics*, 49:205, 1995.

[139] N. Mingo. *Appl. Phys. Lett.*, 85:5986, 2004.

[140] H. Venghaus and P. Dean. *J. Phys. Rev. B*, 21:1596, 1980.

[141] V. B. Anzin, M. I. Eremets, Y. V. Kosichkin, A. I. Nadezhdinskii, and A. M. Shirokov. *Phys. Status Solidi A*, 42:385, 1977.

[142] V. A. Vis. *J. Appl. Phys.*, 35:360, 1964.

[143] Z. P. Liu, Z. K. Hu, Q. Xie, B. J. Yang, J. Wu, and Y. T. Qian. *J. Mater. Chem.*, 13:159, 2003.

[144] T. Ikari, H. Berger, and F. Levy. *Mater. Res. Bull.*, 21:99, 1986.

[145] K. Araki and T. Tanaka. *Jpn. J. Appl. Phys.*, 11:472, 1972.

[146] T. El-Nabarawy, A. A. Attia, and M. N. Alaya. *Mater. Lett.*, 24:319, 1995.

[147] M. Yosef, A. K. Schaper, M. Fro1ba, and S. Schlecht. *Inorg. Chem.*, 44:5890, 2005.

[148] Y. Wang and K. Wu. *J. Am. Chem. Soc.*, 127:9687, 2005.

[149] Crc handbook of chemistry and physics, 48th edition. pages B–230, 1967.

[150] A. Birner, R. B.Wehrspohn, U. Gösele, and K. Busch. *Adv. Mater.*, 13:377, 2001.

[151] H. Ennen, J. Schneider, G. Pomrenke, and A. Axmann. *Appl. Phys. Lett.*, 43:943, 1983.

[152] A. Polman. *J Appl.Phys.*, 82:1, 1997.

[153] Z. Wang and J. L. Coffer. *Nano Lett.*, 2:1303, 2002.

[154] J. Wu, P. Punchaipetch, R. M. Wallace, and J. L. Coffer. *Adv. Mater.*, 16:1444, 2004.

[155] P. Lerner, C. Legras, and J. P. Dumas. *J. Cryst. Growth*, 3/4:231, 1968.

[156] G. Arlt. *J. Mater. Sci.*, 25:2655, 1990.

[157] S. Ottow, V. Lehmann, and H. Föll. *J. Electrochem. Soc.*, 143:385, 1996.

[158] V. Bouquet, E. Longo, E. R., Leite, and J. A.Varela. *J. Mater. Res.*, 14:3115, 1999.

[159] M. A. McCoy, S. A. Dregia, and W. E. Lee. *J. Mater. Res.*, 9:2029, 1994.

[160] J. H. Jean and T. K. Gupta. *J. Mater. Res.*, 7:3103, 1992.

[161] A. Navrotsky, K. L. Gelsinger, P. Mcmillan, and G. V. Gibbs. *Phys. Chem. Miner*, 11:284, 1985.

[162] Z. Zhang, J. Y. Ying, and M. S. Dresselhaus. *J. Mater. Res.*, 13:1745, 1998.

[163] R. H. Doremus. *J. Phys. Chem.*, 80:1773, 1976.

[164] X. M. Chen, Q. Wang, X. Wu, and K. Q. Lu. *J. Cryst. Growth*, 204:163, 1999.

[165] R. Lenormand. *J. Phys. Condensed Mater.*, 2:SA79, 1990.

[166] M. G. Bernadiner. *Transport in Porous Media*, 30:251, 1998.

[167] L. Rayleigh. Scientific papers. *Cambridge University Press*, 3, 1902.

[168] M. Steinhart, R. B. Wehrspohn, U. Gösele, and J. H. Wendorff. *Angew. Chem. Int. Ed.*, 43:1334, 2004.

[169] P. Andonov, P. Chieux, and S. Kimura. *Physica Scripta*, T57:36, 1995.

[170] P. Andonov, S. Kimura, T. Sawada, and A. Z. Kobayashi. *Z. Naturforsch.*, 51a:133, 1996.

[171] M. Fleuster, C. Buchal, E. Snoeks, and A. Polman. *Appl. Phys. Lett.*, 65:225, 1994.

[172] R. Brinkmann, W. Sohler, and H. Suche. *Electronic Lett.*, 27:415, 1991.

[173] R. Bechmann. *Phys. Rev.*, 110:1060, 1958.

[174] R. Fan, Y. Y. Wu, D. Y. Li, M. Yue, A. Majumdar, and P. D. Yang. *J. Am. Chem. Soc.*, 125:5254, 2003.

[175] F. L. Deepak, G. Gundiah, M. Motin Seikh, A. Govindaraj, and C. N. R. Rao. *J. Mater. Res.*, 19:2216, 2004.

[176] A. Okabe, M. Niki, T. Fukushima, and T. Aida. *Chem. Lett.*, 35:228, 2006.

[177] F. E. Wagstaff and K. J. Richards. *J. Am. Ceram. Soc.*, 49:118, 1966.

[178] V. G. Pol, A. Gedanken, and J. Calderon-Moreno. *Chem. Mater.*, 15:1111, 2003.

[179] A. M. Venezia, V. La Parola, A. Longo, and A. Martorana. *J. Solid. State. Chem.*, 161:373, 2001.

APPENDIX A

Curriculum vitae

First Name	Lili
Family Name	Zhao
Date of Birth	June 14, 1977 (Harbin, P. R. China)
Nationality	Chinese
E-mail	*lzhao@mpi-halle.de*

EDUCATION

Oct. 2003 - present	Max Planck Institute of Microstructure Physics and Martin-Luther-University Halle-Wittenberg (Halle, Germany) Ph.D. candidate (Supervisors: Prof. Ulrich Gösele and Dr. Martin Steinhart)
Sep. 2001 - Jun. 2003	Harbin Institute of Technology (Harbin, P. R. China) Master Degree in Mechanical Engineering
Mar. 2002 - Feb. 2003	Hongkong University of Science and Technology (Hongkong, P.R. China), experimental work for master thesis Department of Mechanical Engineering
Sep. 1996 - Jul. 2000	Harbin Institute of Technology (Harbin, P. R. China) Bachelor Degree in Applied Chemistry

---

HONORS AND AWARDS

Apr. 2005	Chinese Government Award for Outstanding Self-Financed Students Abroad
2003 - 2006	Research Scholarship of the Max Planck Institute
Jul. 2003	Excellent Alumnus of Harbin Institute of Technology

A.1 List of Publications

- **L. L. Zhao**, X. Wang, B. Wang, W. Wen, T. Y. Zhang "ZnO-doped LiNbO$_3$ single crystals studied by X-ray and density measurements ", *Appl. Phys. B* 78, 769-774 (2004).

- **L. L. Zhao**, M. Steinhart, M. Yosef, E. Pippel, R. Scholz, U. Gösele, and S. Schlecht "Lithium Niobate Microtubes within Ordered Macroporous Silicon by Templated Thermolysis of a Single Source Precursor", *Chem. Mater.* 17, 3-5 (2005).

- **L. L. Zhao**, M. Steinhart, M. Yosef, S. K. Lee and S. Schlecht "Large-scale template-assisted growth of LiNbO$_3$ one-dimensional nanostructures for nano-sensors", *Sensors and Actuators B* 109, 86-90 (2005).

- **L. L. Zhao**, M. Steinhart, M. Yosef, S. K. Lee and S. Schlecht "Lead Titanate Nano- and Microtubes", *J. Mater. Res.* 21, 685-690 (2006).

- **L. L. Zhao**, M. Yosef, M. Steinhart, P. Goering, H.Hofmeister, U. Gösele and S. Schlecht "Porous silicon and alumina as chemically reactive templates for the synthesis of tubes and wires of SnSe, Sn and SnO$_2$", *Angew. Chem. Int. Ed.* 45, 311-315 (2006).

- **L. L. Zhao**, T. Z. Lu, M. Zacharias, J. Yu, J. Shen, H. Hofmeister, M. Steinhart and U. Gösele "Integration of Erbium-Doped Lithium Niobate Microtubes into Ordered Macroporous Silicon", *Adv. Mater.* 18, 363-366 (2006).

- **L. L. Zhao**, M. Yosef, E. Pippel, H. Hofmeister, M. Steinhart, U. Gösele and S. Schlecht "Killing four birds with one stone: Synthesis of nanostructures of ZnTe, Te, ZnAl$_2$O$_4$ and ZnAl$_2$O$_4$-Te from one single source precursor", *Angew. Chem. Int. Ed.* in press.

- O. Kriha, **L. L. Zhao**, L. L. Zhao, M. Steinhart, E. Pippel, U. Gösele, R. B. Wehrspohn, J. Wendorff, A. Greiner "Organic tube/rod hybrid nanofibers with adjustable segment length by bidirectional template wetting", *submitted.*

- **L. L. Zhao**, T. Z. Lu, M. Yosef, M. Steinhart, M. Zacharias, U. Gösele, S. Schlecht "Single-crystalline CdSe nanostructures: from primary grains to oriented nanowires", *submitted.*

A.2 List of Presentations

- **L. L. Zhao**, M. Steinhart, M. Yosef, S. K. Lee, S. Schlecht "Large-scale template-assisted growth of LiNbO$_3$ one-dimensional nanostructures for nanosensors", *E-MRS Fall Meeting* September 6-10, Poland, Warsaw (2004) talk.

- **L. L. Zhao**, M. Steinhart, M. Yosef, P. Göring, E. Pippel, U. Gösele, S. Schlecht "Template-assisted synthesis of one dimensional nanostructures by single source

precursor", *Science and Technology of Inorganic Nanowires* February 13-16, Bad Honnef, Germany (2005) poster.

- **L. L. Zhao**, M. Steinhart, J. Shen, J. Yu, P. Göring, H. Hofmeister, M. Alexe, U. Gösele "Lithium Niobate and doped Lithium Niobate nanoshell tubes by high-temperature melts wetting", *17th International Symposium on Integrated Ferroelectrics(ISIF)* April 17-20, Shanghai, China (2005) talk.

- **L. L. Zhao**, M. Steinhart, J. Yu, J. Shen, E. Pippel, P. Göring, M. Alexe, U. Gösele "Controlled One-Dimensional Nanostructures of $PbTiO_3$: From anoparticles to Nanotubes", *17th International Symposium on Integrated Ferroelectrics(ISIF)* April 17-20, Shanghai, China (2005) poster.

- **L. L. Zhao**, M. Steinhart, T. Z. Lu, M. Zacharias, M. Yosef, P. Goering, E. Pippel, S. K. Lee, S. Schlecht "CdSe: from nanoparticles to nanowires" nanotube and nanowire", *SPP1165* May 2-4, Fulda, Germany (2005) poster.

- **L. L. Zhao**, M. Steinhart, M. Yosef, U. Gösele and S. Schlecht "Synthesis of single-crystalline ZnTe, Te and ZnA_2O_4-Te nanowires and ZnA_2O_4 nanotubes by templated thermolysis of a single source precursor ", *E-MRS Spring Meeting* May 29-Jun 2, Nice, France (2006) talk.

- **L. L. Zhao**, M. Steinhart, M. Yosef, S. K. Lee, U. Gösele and S. Schlecht "Lithium induced crystallization in amorphous SiO_2 microtubes", *E-MRS Spring Meeting* May 29- Jun 2, Nice, France (2006) poster.

- **L. L. Zhao**, M. Yosef, E. Pippel, H. Hofmeister, M. Steinhart, U. Gösele and S. Schlecht "Synthesis of single-crystalline ZnTe, Te and ZnA_2O_4-Te nanowires and ZnA_2O_4 nanotubes by templated thermolysis of a single source precursor ", *Nanowires and Nanotubes, Synthesis and Characterization* September 11-15, Kleinwalsertal, Austria (2006) talk.

APPENDIX B

Acknowledgements

I would like to take this opportunity to express my gratitude to all of people who accompanied and supported me in the last three years at Max Planck Institute of Microstructure Physics in Halle.

I would like to show my sincere appreciation and respects to my supervisors. First and foremost, Prof. Gösele, for his consistent support, insightful advices and kind guidance for the past three years. His supervision improved my research ability and broadened my view on materials science. Special thanks go to Dr. Steinhart, who introduced me to the research areas of template-wetting method and porous materials. He also supervised me and gave lots of worthy advises and encouragement during my Ph.D period. He took great effort in reading and providing me with valuable comments on earlier versions of this thesis. I wish to express my gratitude to Prof. Schlecht (Free University, Berlin, Germany) who was not only a good collaborator but also a nice supervisor to me. Thank her for her doing the control experiments of redox properties of porous membranes described in the chapter 5. Her indoctrination in the rigor performing research be a valuable lesson for my future career.

I feel a deep sense of gratitude for Dr. Hofmeister, Dr. Pippel, and Dr. Erfurth for their introduction of electron microscopy measurements and their support on the analysis of the nano- and microstructures described in this thesis. I would like to express my great gratitude to Ms. Möhner and Ms. Hopfe who supported my work with their skilled techniques in preparation TEM samples. Thanks also go to Ms. Sklarek for her kind support in the chemical lab and helping me ordering all kinds of experimental stuff. I thank Mr. Silko and Ms. Schwirn, Mr. Langner for always providing me porous templates on time. I thank Dr. Göring for taking time to preform XRD on my samples. I thank Dr. Yoself (Free University, Berlin, Germany) for the synthesis and characterization of the precursors.

I own thanks to Dr. Rehn, Mr. Zschech, Mr. Hohlbein and Mr. Bauer who share office with me as well as their friendship for the past three years, especially thank Dr. Rehn, for introducing the German culture to me and for translating various German letters for me. I wish to acknowledge the group of "Ordered Porous Materials" at MPI-Halle. During the last three years, I was continuously encouraged and supported by them. I would like to thank all the group members who helped me in all the directions either in my life or research. Many thanks for accepting me as your colleague. I wish to express my gratitude to Dr. Alexe, Dr. Hesse, Dr. W. Lee, and Dr. S.K. Lee for valuable discussions and support.

I deeply thank all Chinese friends in Halle for their support and friendship. Without their support, my last three years would not have been such rich and colorful. This thesis is dedicated to my husband and my parents. Without their endless love and sacrifice, nothing could have been accomplished.

APPENDIX C

Eidesstattliche Erklärung

Ich erkläre hiermit, dass ich keine anderen als die von mir angegebenen Quellen und Hilfsmittel zur Erstellung meiner Dissertation verwendet habe. Den benutzten Werken wörtlich oder inhaltlich entnommene Stellen sind als solche gekennzeichnet.

Lili Zhao

Halle (Saale), den 9 October 2006